The Dissertation Committee for Talal Eid Alotaibi

Certifies that this is the approved version of the following dissertation:

Applications of Phase-Field Modeling in Hydraulic Fracture

APPROVED BY

SUPERVISING COMMITTEE:

Chad M. Landis, Supervisor

Mukul M. Sharma

Mark E. Mear

Krishnaswa Ravi-Chandar

John T. Foster

Applications of Phase-Field Modeling in Hydraulic Fracture

by

Talal Eid Alotaibi

DISSERTATION

Presented to the Faculty of the Graduate School of

The University of Texas at Austin

in Partial Fulfillment

of the Requirements

for the Degree of

DOCTOR OF PHILOSOPHY

The University of Texas at Austin

December 2019

Dedicated to my sister Nawal

Acknowledgments

I would like to express my sincerest of gratitude to my supervisor, Professor Chad Landis, for his guidance and support; it has been a privilege to work with him. Since the time I start my research with him, he has been a very helpful mentor that guided me throughout my Ph.D. study. My sincere gratitude also goes to my Ph.D. committee members; Professor Mukul Sharma, Professor Mark Mear, Professor Krishnaswa Ravi-Chandar, and Dr. John Foster, for their valuable time and giving me insightful reviews that enhanced this document. I am also very thankful to Dr. Murtadha Altammar for his collaboration in one of the problems I have worked on in this dissertation.

I would like to acknowledge the financial support from both the Public Authority for Applied Education and Training (PAAET) and Kuwait Embassy for their generous scholarship that gave me the opportunity to pursue my graduate study at the University of Texas at Austin.

I have been lucky to have my mother, brothers, and sisters, with their unconditional love, support, and encouragement. They are always beside me whenever I need help. Lastly, I would like to express my ultimate gratitude to my lovely wife Maha, for her love, support, and patience during my Ph.D. process. She is the key to every success in my life.

Abstract

Applications of Phase-Field Modeling in Hydraulic Fracture

Publication No. _____

Talal Eid Alotaibi, PhD

The University of Texas at Austin, 2019

Supervisor: Chad M. Landis

Understanding the mechanisms behind the nucleation and propagation of cracks is of considerable interest in engineering application and design decisions. In many applications in the oil industry, complicated fracture geometries and propagation behaviors are encountered. As a result, the development of modeling approaches that can capture the physics of non-planar crack evolution while being computationally tractable is a critical challenge. The phase-field approach to fracture has been shown to be a powerful tool for simulating very complex fracture topologies, including the turning, splitting, and merging of cracks. In contrast to fracture models that explicitly track the crack surfaces, crack propagation and the evolution thereof arise out of the solution to a partial differential equation governing the evolution of a phase-field damage parameter. As such, the crack

growth emerges naturally from solving the set of coupled differential equations linking the phase-field to other field quantities that can drive the fracture process. In the present model, the physics of flow through porous media and cracks is coupled with the mechanics of fracture. Darcy-type flow is modeled in the intact porous medium, which transitions to a Stokes-type flow regime within open cracks. This phase-field model is implemented to gain insights into the propagation behavior of fluid-injected cracks.

One outstanding issue with phase-field fracture models is the decomposition of the strain energy required to ensure that compressive stress states do not cause crack propagation and damage evolution. In the present study, the proper representation of the strain energy function to reflect this fracture phenomenon is examined. The strain energy is constructed in terms of principle strains in such a way that it has two parts; the tensile and the compressive. A degradation function only applies to the tensile part enforcing that the crack is driven only by that part of the strain energy. We investigated the split operator proposed by Miehe et al. [1], and then proposed a split approach based on masonry-like material behavior [2, 3]. We have found that when using Miehe's form for the strain energy function, cracks can propagate under compressive stresses. In contrast, the approach based on a masonry-like materials constitutive model we proposed ensures that cracks do not grow under compressive stresses.

To demonstrate the capabilities of phase-field modeling for fluid-driven fractures, four general types of problems are simulated: 1) interactions of fluid-driven, natural, and proppant-filled cracks, 2) crack growth through different material layers, 3) fluid-driven

crack growth under the influence of in-situ far-field stresses, and 4) crack interactions with inclusions. The simulations illustrate the capabilities of the phase-field model for capturing interesting and complex crack growth phenomena.

To understand how fluid-driven cracks interact with inclusions, AlTammar et al. [4] performed experiments. Three tests with tough inclusions were performed to understand the effects of orientation angle, thickness, and material properties. Additionally, one test with a weak inclusion was performed to compare the results with those of the tough inclusion cases. The experiments show a clear tendency for the fluid-driven hydraulic fracture to cross thick natural fractures filled with materials weaker and softer than the matrix and to be diverted by thick natural fractures with tougher and stiffer filling materials. To replicate these experiments numerically and to gain a mechanistic understanding, in the present study, we ran simulations using phase-field modeling. Results from both the experiments and the simulations provide clear evidence that inclusion width, angle, material properties, and distance from the injection point affect the outcome of the crack evolution. Phase-field modeling was able to capture the trends of crack deflection/crossing in all the test cases.

Finally, we extended the phase-field model has been extended to three dimensions and tested it on bench-mark problems. The first bench-mark problem is a compact test for a CT specimen. In this problem, the mechanical equations are only considered. The simulation shows that the CT specimen is split into two symmetric parts. The second

bench-mark problem is a fluid-driven circular crack. The simulation for this problem shows that the crack grows in a radial direction.

Table of Contents

List of Tables

List of Figures

Chapter 1. Introduction

Phase-field modeling is a powerful tool in simulating and understanding the evolution of microstructures with multi-phases, defects, and discontinuities. The approach utilizes a continuous phase-field parameter that smears discontinuities in diffuse zones. When applied to hydraulic fractures, the phase-field approach has been shown to be a powerful tool in simulating very complex fracture topologies, including the turning, splitting, and merging of cracks. In contrast to classical fracture models that explicitly track the crack surfaces, in the phase-field approach, crack evolution and propagation arise out of the solution to a partial differential equation governing the evolution of a phase-field damage parameter. As such, the crack growth emerges naturally from solving the set of coupled differential equations linking the phase-field to other field quantities that can drive the fracture process.

Fluid-driven fractures have been of great interest in many engineering applications, including injecting waste disposal into underground formations [5, 6], the simulation of groundwater wells [7, 8], and the stimulation of geothermal reservoirs [9, 10]. More importantly, applications dealing with hydraulic fractures have great impact on the oil and gas industry, making the extraction of crude oil and gas from unconventional reservoirs feasible. In 2016, according to the U.S. Energy Information Administration, 670,000 wells were hydraulically fractured, representing about 69% of the producing wells [11]. The cost

of each fracturing job is about $4.9 to $8.3 million per well [12]. Optimizing the hydraulic fracture treatment is essential to making oil and gas production more economical.

1.1 Scope of the Study

In the present model, the physics of flow through porous media and cracks is coupled with the mechanics of fracture. Darcy-type flow is modeled in the intact porous medium, which transitions to a Stokes-type flow regime within open cracks. This phase-field model is implemented to gain insights into the propagation behavior of fluid-injected cracks.

One outstanding issue with phase-field fracture models is the decomposition of the strain energy that is required to ensure that compressive stress states do not cause crack propagation and damage evolution. The present study examines the proper representation of the strain energy function to reflect this fracture phenomenon is examined. The strain energy is constructed in terms of principal strains in such a way that it has two parts: tensile and compressive. A degradation function only applies to the tensile part, ensuring that the crack is driven only by that part of the strain energy. We found that the split operator proposed by Miehe et al. [1] creates an issue regarding allowing the fracture's growth under compressive stresses. To solve this issue, we proposed a split approach based on the behavior of masonry-like material [2, 3] that ensures that the fracture cannot propagate under compressive stresses. In this regard, our approach is superior to the split operator proposed by Miehe that has been adopted in most of the literature.

To demonstrate the capabilities of phase-field modeling for fluid-driven fractures, four general types of problems are simulated: a) interactions of fluid-driven, natural, and proppant-filled cracks; b) fluid-driven crack growth under the influence of in-situ far-field stresses; c) crack interactions with inclusions; and d) crack growth through different material layers. The simulations illustrate the capabilities of the phase-field model for capturing interesting and complex crack growth phenomena.

The problem of crack interaction with other cracks is relevant to underground reservoirs containing natural cracks. We simulated a fluid-driven fracture interacting with natural fractures at different angles. Another interesting problem is the interaction of multiple parallel fluid-driven fractures, a problem that is relevant to hydraulic fracture treatments and is essential to the design of the fracturing spacings. We use the phase-field approach to give some insights into the effect of varying the number of perforations within each stage on opening and stress shadowing, associated with the cracks.

Another problem to be studied is how a crack interacts with layers made of different materials. This problem is relevant to the design of hydraulic fracturing jobs since the subsurface geologically consists of layers, raising questions as to what might cause a fracture to stay within a target layer or not. For example, this might significantly impact the environment with regard to the contamination of water reserves. Therefore, the present study investigates multiple factors that contribute to controlling a fracture's propagation and orientation.

In-situ stresses are considered to be the dominant factor in crack propagation and orientation. In the design of fracturing jobs, the orientation of perforations in each stage

depends on the direction of the in-situ stresses. If an initial fracture misses the direction of favorable in-situ stresses, this might reduce the drainage area, resulting in reduced production and failure of the fracture treatment job. The present study examines the effect of fracture orientation and its evolution under the influence of in-situ stresses. We show that fractures suffer in their growth to the degree that their initial orientations deviate from the maximum stress direction. Besides, we show the influence of the in-situ stresses on the fluid-driven fracture when it encounters a layer of a different material. The aim is to see how the in-situ stresses compete with the tough-stiff layer in controlling the fracture growth orientation.

The problem of a fracture filled with proppant is relevant to hydraulic re-fracturing treatments. Usually, the productivity of the wells decrease within months, and a successful way of increasing the productivity of the well is to re-fracture it. This can increase the well connectivity and thus its productivity. New cracks initiated by the re-fracturing treatment can interact or be influenced by the presence of old cracks filled with proppant, which can impact the drainage area. In the present study, we simulated this problem and examined the effect of the stress shadow produced by the opening of the fracture filled with proppant on the evolution of new fractures.

Concerning natural cracks, some of them are believed to be closed, but others can be open and filled/cemented with different materials [13, 14]. Experiments have been performed by AlTammar et al. [4] to investigate the effect of the cemented natural fractures on the propagation of the fluid-driven fractures. Three tests with tough-stiff inclusions were performed to understand the effects of orientation angle, thickness, and material properties.

Additionally, one test with a weak-soft inclusion was performed to compare the results with those of the tough-stiff inclusion cases. In order to gain a mechanistic understanding of this problem, we simulated the four experiments using the phase-field approach. An additional simulation was run to show how the distance between the injection point and the inclusion affects the fracture growth.

1.2 Outline of the Dissertation

The dissertation is outlined as follows:

1. Chapter reviews fracture modeling in general and phase-field modeling in greater detail. Also reviewed are relevant problems in the petroleum engineering field such as crack interactions, layer and inclusion problems, and the role of in-situ stresses, giving a clear rationale for studying such phenomena.
2. Chapter 3 focuses on the development of the theory of phase-field modeling. It begins with phase-field modeling in quasi-static brittle materials. After that, an extension to a general theory is presented that accounts for the physics of the fluid injected in a porous medium. Two decomposition forms of the strain energy are presented, one proposed by Miehe [1] and one that we proposed, based on masonry-like materials [2, 3].
3. Results and discussions are presented in Chapter 4. Two tension-compression split approaches are examined. Applications of phase-field modeling are presented

including a) interactions of fluid-driven, natural, and proppant-filled cracks; b) fluid-driven crack growth under the influence of in-situ far-field stresses; c) crack interactions with inclusions, and d) crack growth through different material layers. Additionally, the extension to three dimensions is presented through some benchmark problems, such as pressurized circular crack.

4. In Chapter 5, conclusions are presented, and future work is discussed.

Chapter 2. Background

Hydraulic fracture models have been beneficial in many applications, and primarily for issues in the petroleum field. Such models have contributed to developing hydraulic fracturing techniques that significantly impact the economics of the oil and gas industries. A brief review will be given on some of the problems relevant to the petroleum field that can be simulated with the phase-field approach, including crack interactions with natural cracks, cracks under the influence of in-situ stresses, and cracks in a heterogeneous medium. The need to understand these problems has driven the development of the numerical approach applicable to hydraulic fracture, including the phase-field approach.

2.1 Applications

Unlike conventional reservoirs, some formations that contain gas or oil are tight, meaning that they have very low permeability, making it harder to produce oil or gas. As a result, unconventional techniques have been developed to increase the connectivity of the formation and the productivity of tight oil or gas wells. One technique that has been successful worldwide is hydraulic fracturing (see Figure 2.1).

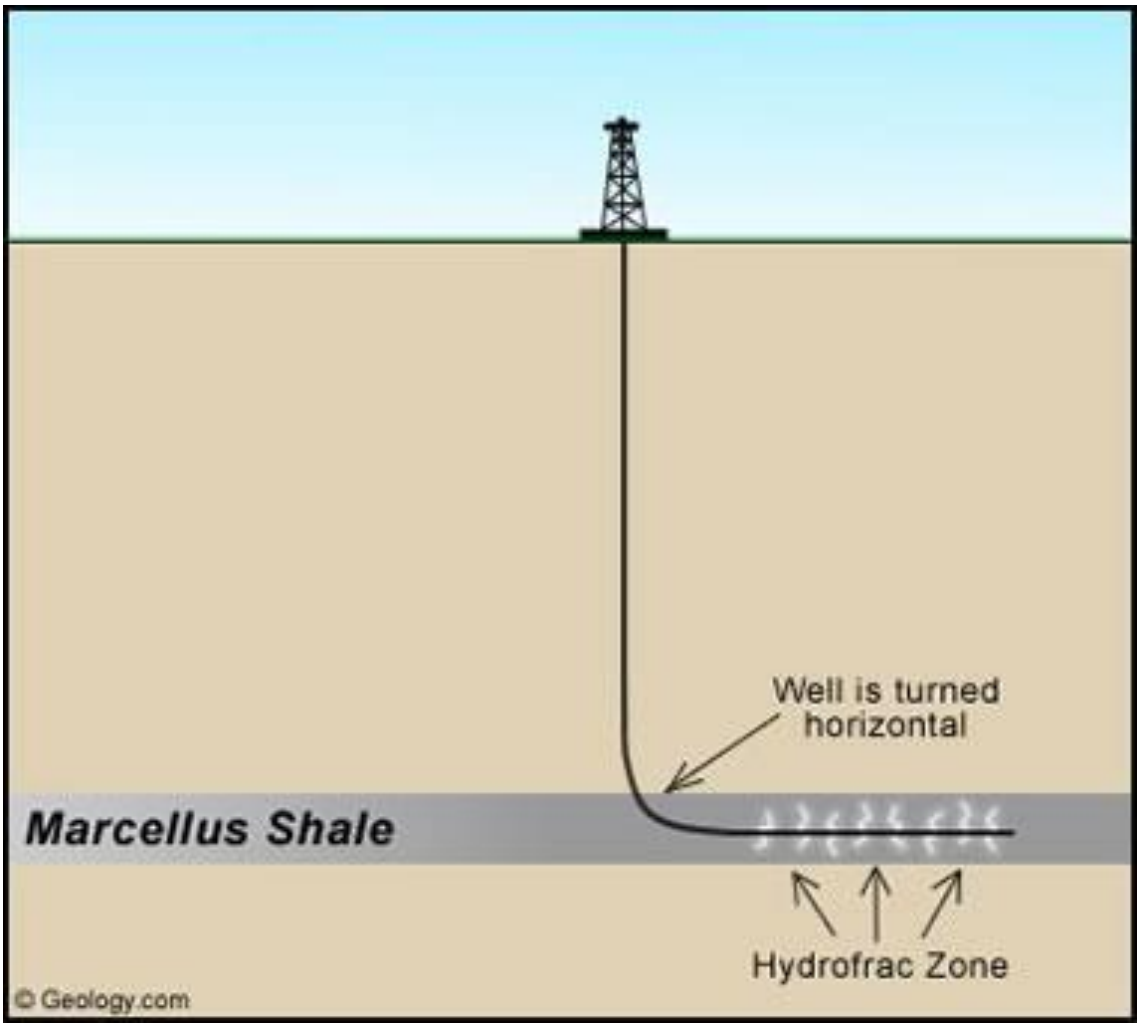

Figure 2.1: Fracturing treatment for a horizontal well in a shale formation. (source [15])

In the fracture treatment, a well is drilled, and a targeted formation containing oil or gas is perforated [16]. After that, a specific chemically formulated fluid called the “pad” is injected at high pressure in the wellbore to create and propagate fractures in the formation. Then, a viscous fluid containing proppant agents (Figure 2.2) is injected to keep the cracks open after the pumping process is completed. Next, the fluid chemically breaks

down and flows back out of the well. The main object of the hydraulic fracture process is to create fractures as long as possible to maximize the drainage area and to effectively place the proppants to keep the fractures open during the production of the gas or oil. Usually, the production of the well declines over time, typically within months [17]. Reasons for this decline have attracted the interest of researchers. One of the solutions to extending the well life is to re-fracture the well to target a new drainage area [18]. Later in this chapter, an issue will be discussed that might arise when new fractures propagate within a region containing old-fractures filled with proppant. A summary of each problem studied in this dissertation will be given.

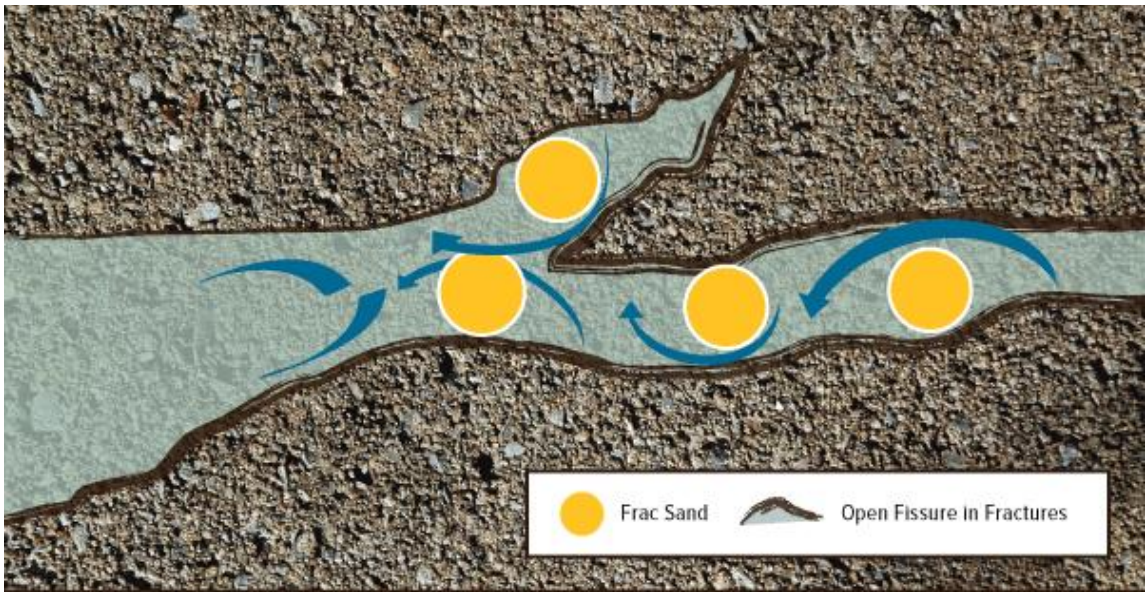

Figure 2.2: Proppant agents in cracks. Their role is to keep the cracks open, thus enhancing the formation connectivity and the well productivity (source [19]).

2.1.1 PRE-EXISTING NATURAL CRACKS

The presence of natural fractures in most shale reservoirs has been documented [20] (see Figure 2.3). Laboratory experiments and core analysis indicate a complex fracture network during hydraulic fracturing treatments [20]. Numerical models, such as the Discrete Element Method (DEM) and the Extended Finite Element Method (XFEM), have been developed to simulate the interaction between hydraulic fractures and pre-existing natural fractures [21]. Evidence suggests that the presence of natural fractures can influence the propagation of hydraulic fractures. The impact of natural fractures on fluid-driven fractures has both advantages and disadvantages [21]. Hydraulic fracture treatments activate the natural fractures and increase the connectivity of the overall fracture network, thus increasing the drainage area, and improving the productivity of the well. However, the presence of natural fractures can also alter the orientation of the hydraulic fractures towards unfavorable directions and possibly terminate their growth, thus reducing the drainage area and the productivity of the well. This problem of how induced fractures interact with natural fractures is studied and presented in Chapter 4.

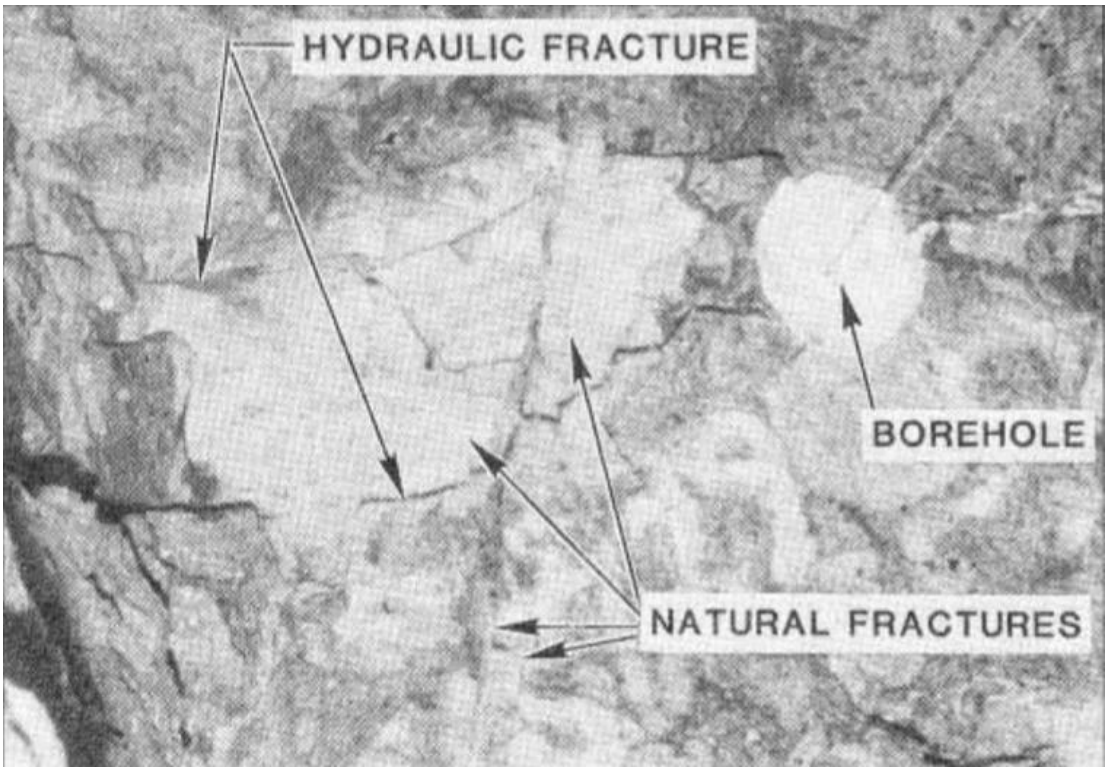

Figure 2.3: In a fractured reservoir, complex hydraulic fractures are influenced by the presence of natural fractures (source [20]).

2.1.2 PARALLEL INDUCED FRACTURES

In hydraulic fracture treatments, perforations are made in multiple stages using perforation gun tools (Figure 2.4). One of the keys to the success of the fracture treatment is the effective design of the fracture spacings throughout the multiple stages. Initiating multi-stage fractures has been found to introduce stress shadow effects and alter the local in-situ stresses [22, 23]. The stress shadow effect is associated with the stress induced in the region surrounding the fluid-driven fractures, and it depends on the net fluid pressure inside the cracks and their geometries [24]. The stress shadow increases as the spacing

between multiple fractures decreases [22, 23]. Increasing the number of fractures may increase the drainage area and thus increase the productivity of the well. However, shorter spacings between the perforations can produce a significant stress shadow that exerts resistance to the opening of the fractures, thus preventing them from propagating [25]. In addition, the stress shadow can also reduce the crack opening and consequently reduce the effectiveness of the proppant placement [25]. The challenge, therefore, is to find the optimal spacing between the perforations that gives the desired drainage area and improves proppant placement with an acceptable stress shadow.

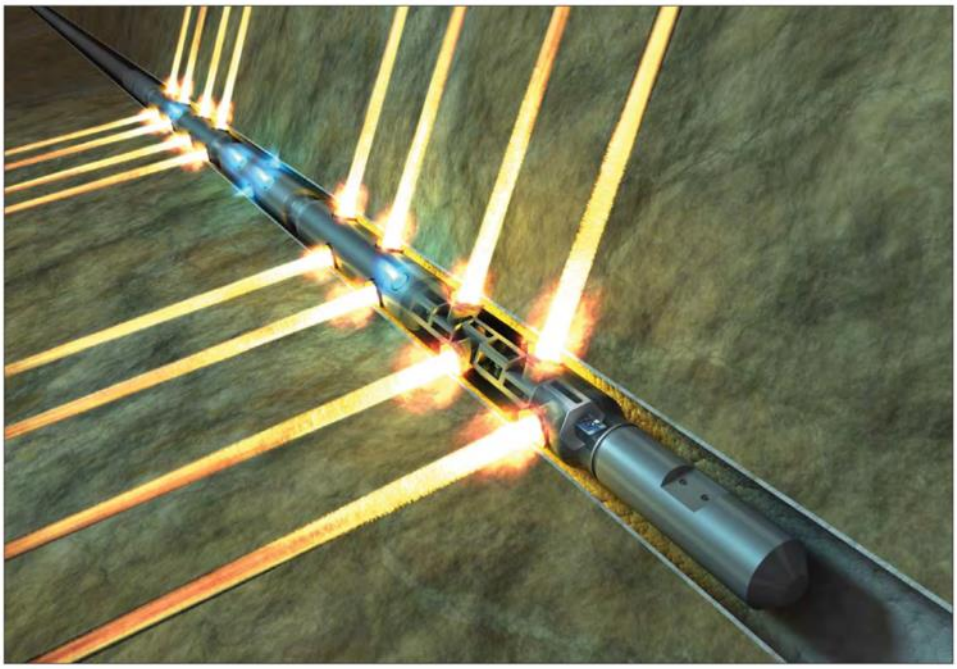

Figure 2.4: Schematic diagram of the perforation gun tool used in initializing multiple stages fractures (source [26]).

A study by Cheng et al. [27] drew the following conclusions: 1) the stress shadow created by multiple fractures significantly affects the fracture opening; 2) increasing the number of fractures within a stage does not necessarily increase the gas production, as it can inhibit the growth of the inner fractures within the stages; and 3) the productivity of the well depends on the number of effective fractures that survive the stress shadow, not on the number of initialized fractures. Hence, fracture treatment designers have to take into account the role of the stress shadow in fracture growth. In the present study, the fracture spacing effect on the behavior of the hydraulic induced fractures is investigated.

2.1.3 IN-SITU STRESSES

Geologically, the stresses that develop in underground formations are called in-situ stresses. In-situ stresses have three components: a) overburden stress caused by the weight of the overlying formation layers at a certain depth; b) the two maximum/minimum horizontal stresses developed because of the confinement and the tectonic forces [28] (see Figure 2.5). The magnitudes and orientations of these stresses are considered to be the dominant factor in fracture treatment design [20, 29]. The contrast ratio of the in-situ stresses has a significant impact on the fracture propagation orientation [30]. The fracture re-orients itself to be perpendicular to the minimum in-situ stress direction. Not only that, but the magnitude of the in-situ stresses also influence the fracture length. The greater the in-situ stresses are, the higher the injection pressure needed to extend the fractures to the

desired length [31-33]. Using the phase-field approach, the problem of induced fracture subjected to in-situ stresses is studied in this dissertation. This approach is able to show the re-orientation of the crack growth under the influence of the in-situ stresses.

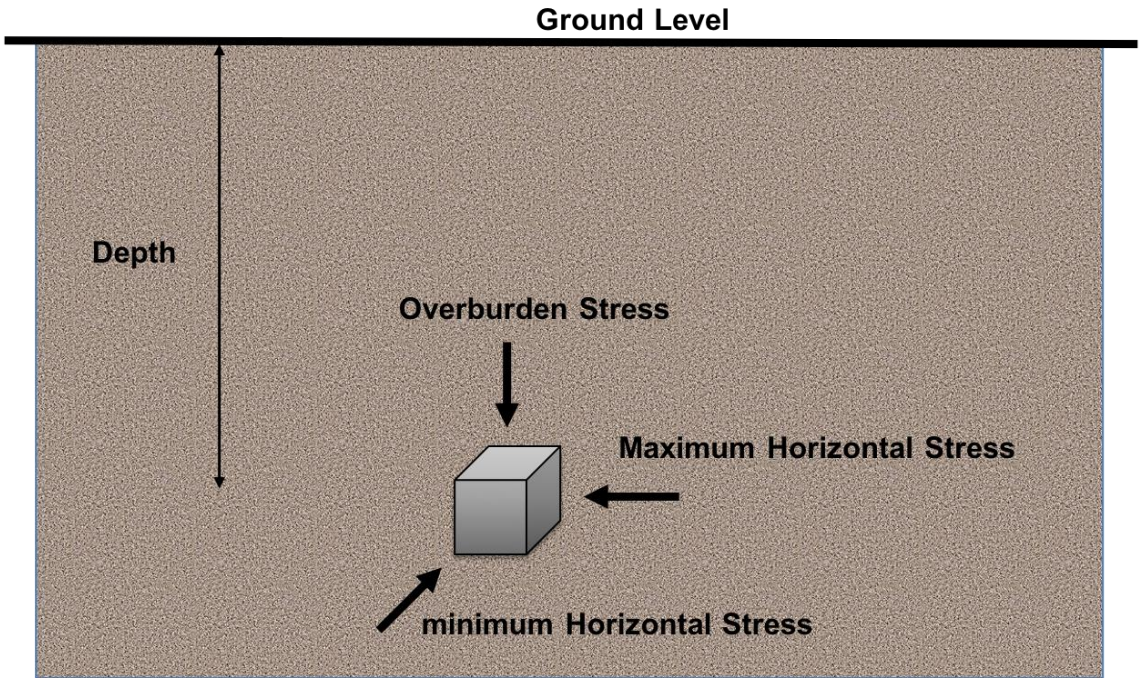

Figure 2.5: The orientation of the in-situ principal stresses: the overburden stress, the maximum principal stress in the horizontal direction, and the minimum principal stress in the horizontal direction.

2.1.4 LAYERS

The heterogeneity in underground formations has attracted considerable interest in the oil and gas industries. It has been suggested that unconventional reservoirs are stratified with multiple layers of materials whose properties, such as elastic stiffness and fracture toughness differ [34-38], and hydraulic fractures are expected to propagate through multiple layers [39, 40] (see Figure 2.6). The fracture behavior across multiple layers has been a controversial topic. Some researchers have argued that a fracture could be arrested if it propagates from a layer with a low modulus of elasticity to a layer with a higher modulus of elasticity [41]. In this situation, layers with a high modulus of elasticity, as it has been argued, act as a barrier. Later, researchers performed experiments showing that the contrast in the moduli of elasticity across layers is not sufficient to prevent a fracture from extending into the stiff layer [42]. Recently, experiments have been conducted to investigate the crack growth across multiple layers with contrasts in both the moduli of elasticity and the fracture toughness [43]. These experiments showed that cracks prefer to propagate from a tough-stiff layer to a weak-soft layer in a relatively straight direction. In contrast, fractures growing in a weak-soft layer prefer to avoid tough-stiff layers. Using the phase-field approach, various factors have been investigated that contribute to controlling the fracture growth including, the layer's thickness, the orientation of the layer, the contrast in material properties between the matrix and the layer, the injected fluid viscosity, and the distance between the injection point and the layer.

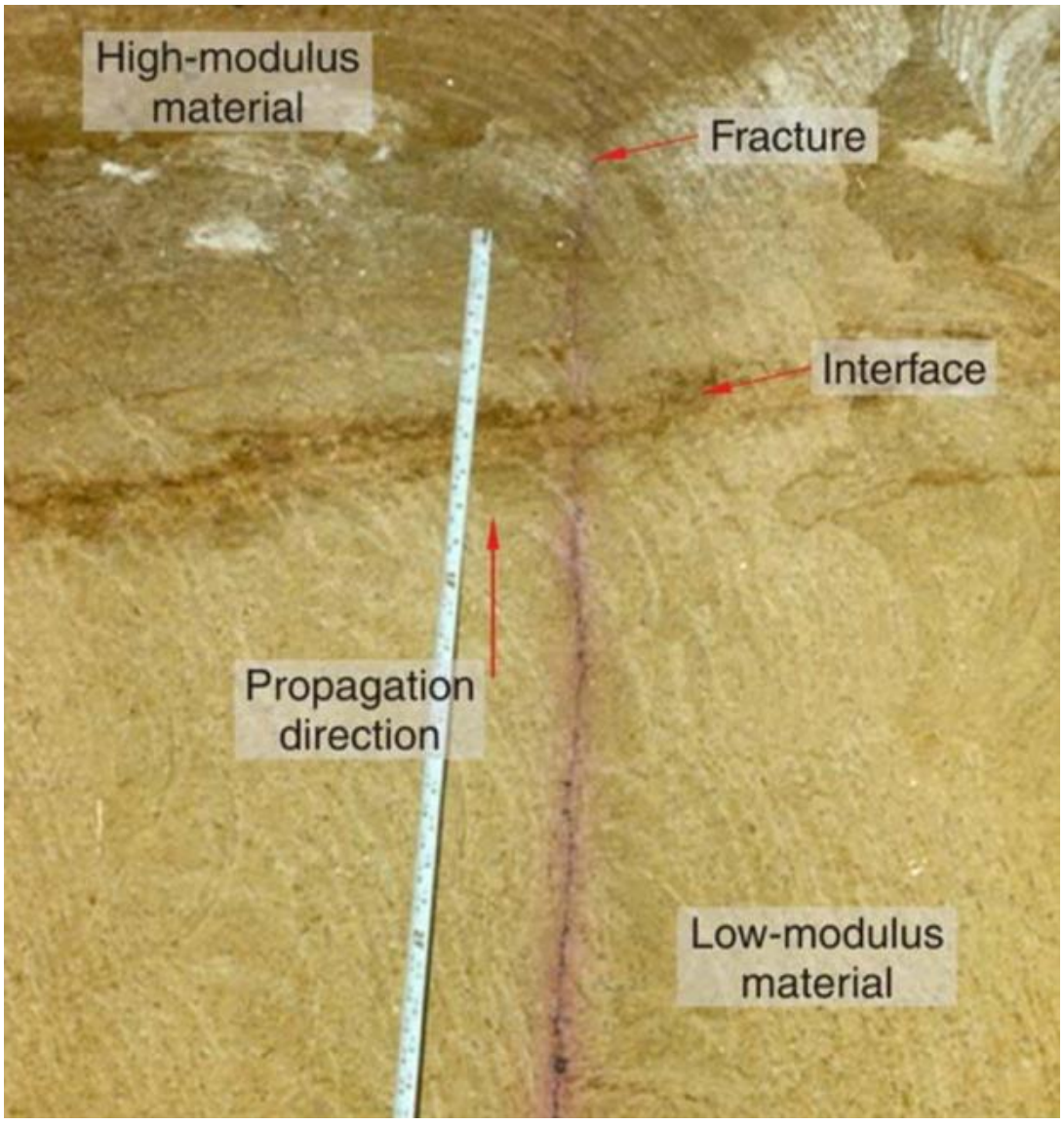

Figure 2.6: Mineback photograph of a fracture propagating from low-modulus material to high-modulus material (source [39]).

2.1.5 INCLUSIONS

Most of the previous studies on the natural fractures [20, 21] consider the crack to be closed and have frictional faces. However, natural fractures can have a finite width and be cemented/filled with different materials [13, 14]. Experiments were conducted to investigate how the hydraulic fractures interact with cemented natural fractures [44, 45]. Bahorich et al. [44] represent natural fractures with cement materials by embedding glass, sandstone, and cured plaster slides when casting their plaster blocks. Fu et al. [45] examined hydraulic fracture propagation across natural fractures with partially and fully bonded interfaces. In general, cemented natural fractures can have a higher or lower modulus of elasticity and fracture toughness than the surrounding rock. In this dissertation, the experiments conducted by Altammar et al. [4] are simulated using the phase-field approach. These experiments investigated how cemented natural fractures affect the propagation behaviors of the induced hydraulic fractures. Multiple factors were discussed: elastic and fracture properties, the orientation of the inclusions, and the distance between the injection point and the inclusion.

2.1.6 REFRACTURING TREATMENT AND PROPPANT PLACEMENT

Production decline has been reported in most unconventional wells [17] (see Figure 2.7). The reasons behind such production decline are open to debate. The decline may be caused by a poor selection of the proppant used in the fracture treatment, or it may be a result of a reorientation of the in-situ stresses that causes the cracks to close [29]. The depletion of the wells can alter the pore pressure and thus affect the magnitude and the orientation of the in-situ stresses [18]. One successful solution to enhancing production is re-fracturing treatment [46]. A well can be re-fractured in two possible ways of refracturing the well: a) re-fracturing the well to open the old fractures, or b) refracturing it with new perforations placed in different orientations [47]. The first approach generally does not last for long durations since it targets the same drainage area that has already been depleted. In contrast, the second approach targets a new drainage area, especially it the in-situ stresses have been re-orientated.

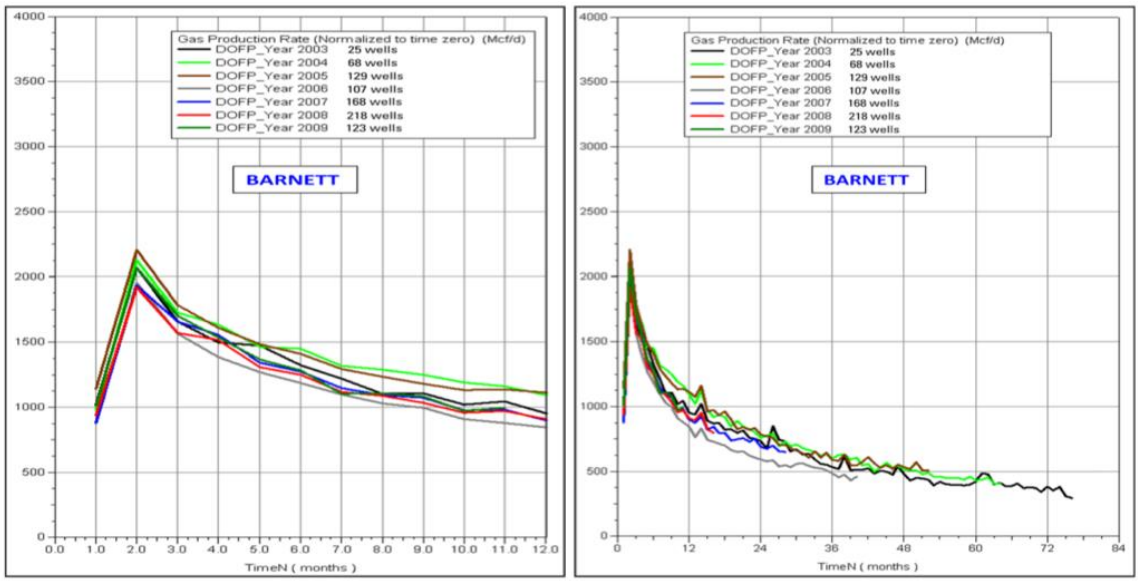

Figure 2.7: Production decline history for some Barnett Shale Wells (source [17]).

If new fractures are created during a re-fracturing treatment, they may pass by and interact with old fractures that are filled with proppants. Fractures filled with proppant can exert a stress shadow effect that interferes with the local in-situ stresses in the vicinity of the new fractures. Using the phase-field approach, we study how proppant-filled fractures influence the new hydraulic fracture. Two factors are examined: a) crack opening and b) the distance between the fluid-driven fracture and the fracture filled with proppant.

2.2 Modeling in Fracture Mechanics

Understanding the mechanisms behind the nucleation and propagation of cracks has been a significant interest in many engineering applications and design decisions, as discussed previously. Numerical approaches have been developed in the spirit of Griffith's theory [48] for brittle materials and of Irwin [49], who extended the theory to ductile materials. Based on the Griffith criteria, a crack advances in materials if the energy release rate reaches a critical value. Due to the complexity of the specimen and crack geometries in engineering applications, the existence of analytic solutions is limited; they do, however, play an essential role in the validation of numerical solutions for simple geometries. For applications where a pressurized fluid drives the crack, analytical solutions have been developed [50-53]. In the early 1940s, a 2D analytical model was developed by Sneddon [50] and extended by Sneddon and Elliot [51]. It assumed that the fracture is circular and is subject to uniform internal pressure. Additionally, the well-known 2D analytical solutions denoted as PKN and KGD were developed [52, 53]. In the PKN model, developed by Perkins, Kern, and Nordgren [52], the crack height is assumed to be smaller than the crack length. The crack cross-section is assumed to be elliptical, and the crack grows while maintaining a constant height (see Figure 2.8 (a)). In the KGD model developed by Kristonovich, Geertsma, and Daneshy [53], the crack height is assumed to be much larger than the crack length while the crack width remains constant (see Figure 2.8 (b)). All of these analytic solutions simplify the problem by assuming symmetric and planar crack geometries. Both PKN and KGD models have been modified to incorporate

the leak-off of fluid that is exuded from a pressurized crack into the surrounding porous medium [54-56]. Notable studies conducted by Detournay et al. [54-56] investigated the crack-tip behavior during growth by fluid injection. They provided insights into the fluid-driven crack behavior based on a dimensionless parameter $\mathcal{K}$ that compares the material fracture toughness K_{IC} to the fluid viscosity v^f,

$$\mathcal{K} = 4K_{IC}/\sqrt[4]{3\pi^3 E'^3 Q v^f} \qquad (2.1)$$

Where Q is the volumetric injection rate. Two regimes have been investigated; 1) a toughness-dominated regime, where the energy dissipated at the crack tip to propagate the fracture is large compared to the energy dissipated due to the flow of the viscous fluid ($\mathcal{K} \to \infty$), and 2) a viscosity-dominated regime, where the energy dissipated due to the flow of the viscous fluid is very large in comparison to the dissipation due to fracture propagation ($\mathcal{K} \to 0$).

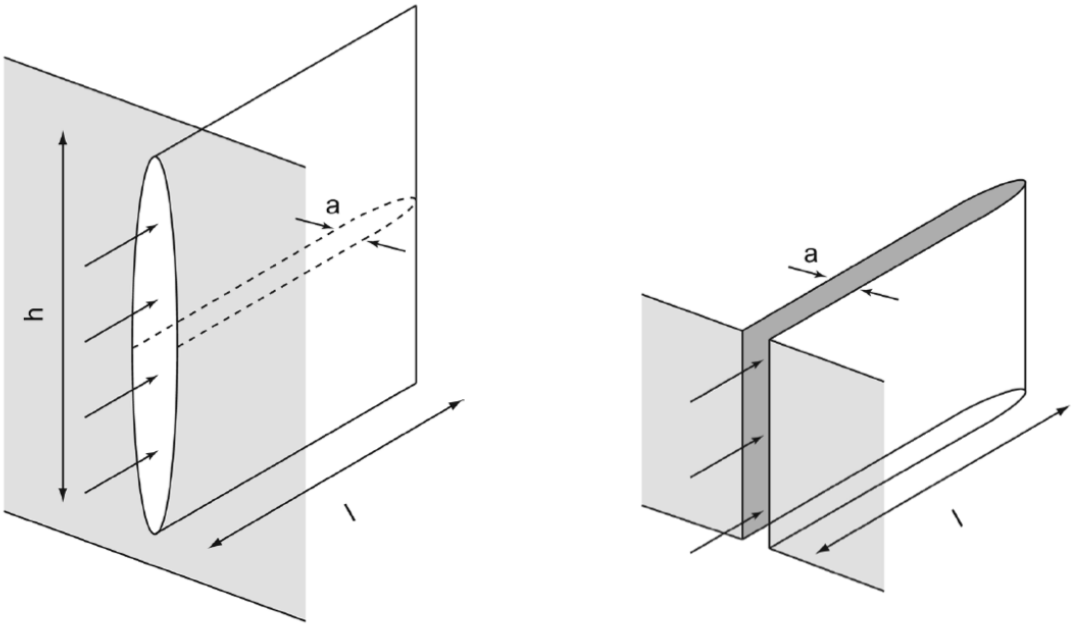

a) PKN model b) KGD model

Figure 2.8: Traditional models for pressurized crack. (a) PKN model, (b) KGD model (source [57]).

In all of the problems discussed previously, the fracture propagates through permeable rocks that are filled with oil or gas. These fractures can be affected by the heterogeneity of materials found in the reservoir formations, by variations in the magnitude and orientation of in-situ stresses, and by the presence of pre-existing natural cracks [21, 58-60]. Due to these complexities, generating analytic solutions for such cases is practically hopeless. This motivates the introduction of numerical approaches. Numerical methods for fracture problems can be divided into two main groups: a) models that treat a crack as a sharp interface and represent it explicitly with the formulation, which require

constitutive rules for how cracks propagate, turn, merge, branch, etc.; and b) diffuse crack models, which represent the crack implicitly by a variable, and the evolution of this variable is generated by partial differential equations [61].

In the first group, Rungamornrat, Wheeler, and Mear [62] developed a fully three-dimensional Galerkin boundary element method, which only requires a boundary element mesh on the surface of the crack. Taleghani and Olson [63] modified the extended finite element method (XFEM) for modeling crack propagation. Recently, a finite volume-based cohesive zone model was developed by Sharma et al. [64] to simulate fluid-driven fractures in poroelastic materials. Some of these types of models identify and track the crack faces where additional criteria are needed for the turning, branching, and merging of cracks. In some cases these models require remeshing techniques, including disconnecting or eliminating elements and moving nodes (see Figure 2.9). This can become algorithmically tedious especially when accounting for the branching and merging of multiple cracks in three-dimensions. The need to deal with the discontinuities associated with the crack growth and interactions leads to the importance and power of second group of numerical solutions to fracture problems that smear the crack over a finite volume.

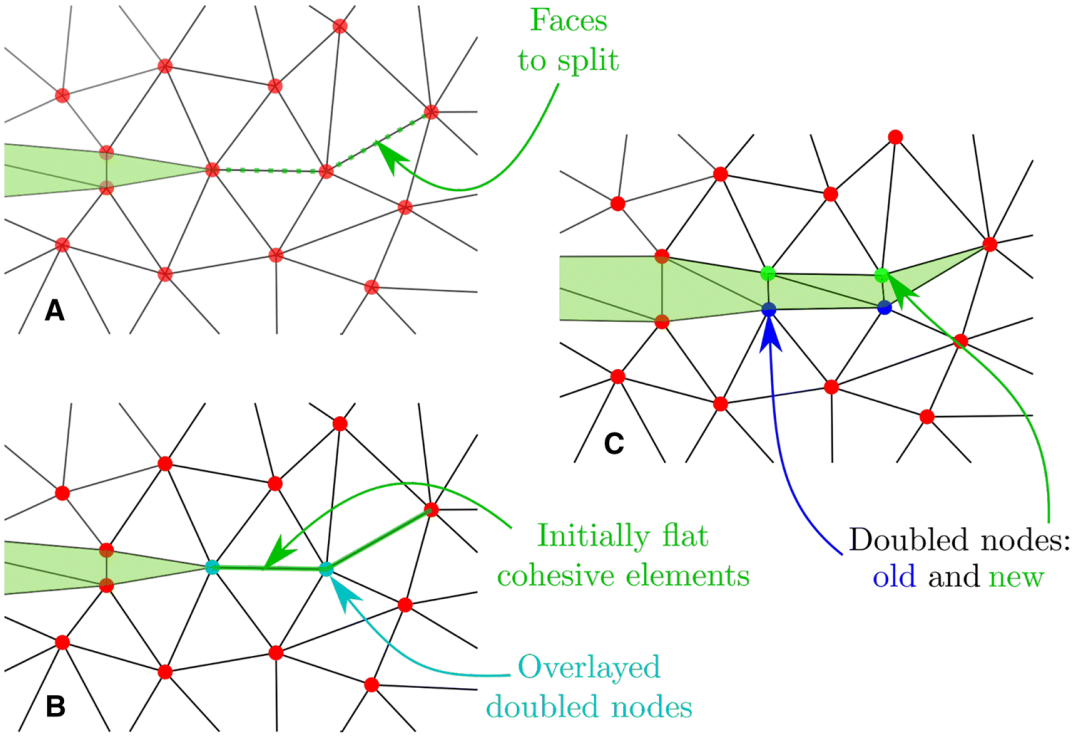

Figure 2.9: Classical FEM model tracing the faces of a crack (source [65]) and requiring remeshing techniques such as disconnecting, elements insertion, and moving nodes.

A notable example of the diffuse crack approaches is peridynamics [66, 67]. Peridynamics theory is a nonlocal theory that deals with points of discrete materials allowed to interact with other material points that reside in a nearby horizon. This becomes a powerful tool when dealing with discontinuities like cracks. Another example of the diffuse models is the phase-field approach discussed in the present study and by others [1, 61, 68-91]. In the following section, a review is given of the phase-field approach to fracture.

2.3 Phase-Field Modeling

Classic models that treat the discontinuities as sharp interfaces suffer from some numerical difficulties raised by the need for remeshing techniques and due to the requirement for constitutive rules for crack turning, branching, and intersection. Remeshing can be numerically tedious when simulating a fracture that might branch or merge with other fractures especially in three dimensions. These numerical obstacles highlight the power of the diffuse models including the phase-field approach. In general, the phase-field method is a mathematical modeling approach for physical problems involving the evolution of interfaces [92, 93]. Surfaces of discontinuity are not introduced into the body; instead, the interface is approximated by a phase-field parameter, which smears the interfacial region over a finite volume, and thus the transition in any property across the interface is continuous as opposed to a jump. This method has been used in many engineering applications [75, 94-97], including applications in fracture mechanics. In fracture mechanics, the crack is approximated by a phase-field function $\mu(\boldsymbol{x}, t) \in [0,1]$ that smears the crack in a diffuse zone, as shown in Figure 2.10.

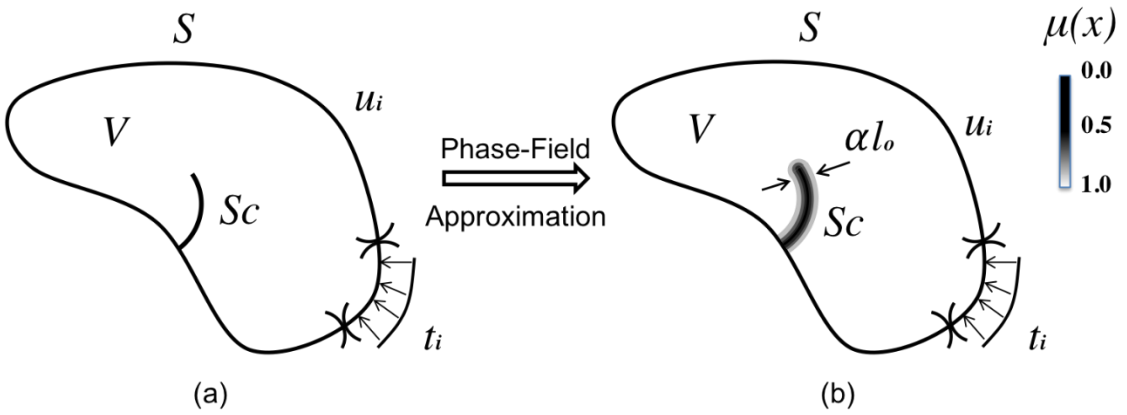

Figure 2.10: An arbitrary body *V* bounded by surface *S* with a) an internal surface of discontinuity S_c representing the crack surfaces. b) An approximation of the internal surface *Sc* by the phase-field μ. The parameter l_0 controls the width of the process zone.

In the phase-field method applied to fracture mechanics that is used in this dissertation, the value $\mu = 0$ represents the damage zone (inside the crack), and the value $\mu = 1$ represents the intact body (away from crack). The major advantage of using the phase-field is that the evolution of the fracture emerges naturally from the solution of a coupled system of partial differential equations. The numerical implementation does not require the tracking of fracture surfaces or remeshing techniques (see Figure 2.11). This approach becomes a powerful and convenient method for dealing with more complex fracture topologies including the branching and merging of cracks.

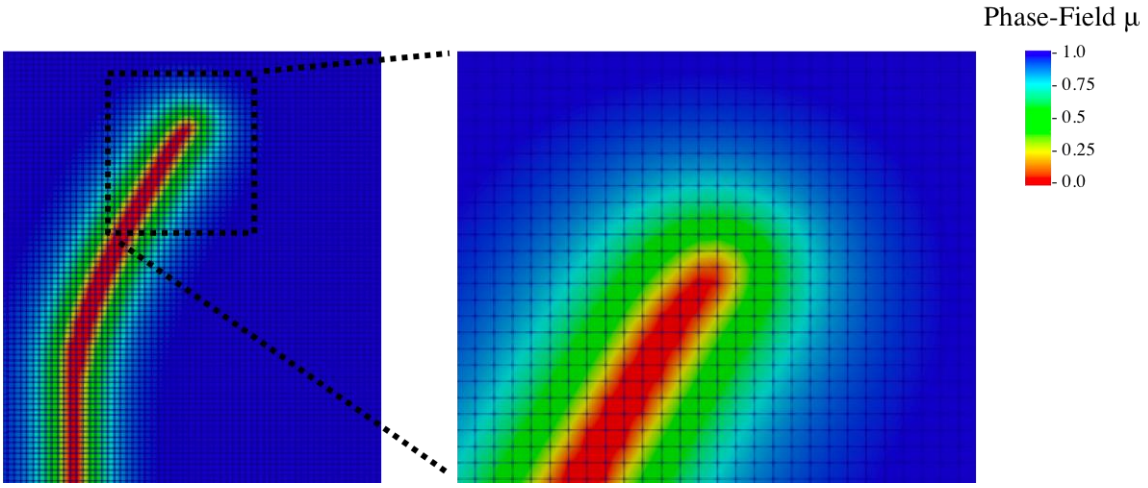

Figure 2.11: In the phase field methods, a crack propagates in a fixed mesh and does not require any remeshing techniques. The crack is represented by the μ function; the value μ=0 represents the damage zone (inside the crack), and the value μ = 1 represents the intact body (away from crack).

2.3.1 PHASE-FIELD MODELING IN FRACTURE MECHANICS

Bourdin et al. [98] were the first to implement the phase-field model to fracture mechanics. They developed a variational reformulation of Griffith's theory for quasi-static brittle fractures, transforming Griffith criterion for fracture into a differential equation by minimizing the total energy of the system with respect to the phase-field and the displacements. It has been proven that this variational formulation recovers Griffith's classical theory in the limit of $l_0 \to 0$ (l_0: phase-field process zone length) based on Γ-convergence [99]. Miehe et al. [1, 84] proposed another way of formulating this phase-field approximation based on continuum mechanics and thermodynamic considerations.

Additionally, they proposed a split operator that decomposes the strain energy function into two parts; tensile and compressive. The idea motivating this split is that damage should only evolve due to tensile stresses. Finally, Borden et al. [70] extend the phase-field model for brittle materials to dynamic cases. They provided an adaptive refinement technique that enhances the computational performance, especially when encountering problems in the three-dimensions.

2.3.2 PHASE-FIELD MODELING IN HYDRAULIC FRACTURE

Bourdin et al. [71] extended their work on the phase-field method to hydraulic fracturing. The problem of hydraulic fracture was simplified by assuming the following: 1) all thermal and chemical effects are neglected; 2) the injection rate is slow enough that all inertial effects can be neglected (quasi-static); 3) the reservoir is made of an idealized impermeable medium; 4) the injected fluid is incompressible; 5) the fluid pressure is constant throughout the fracture system; 6) a perfectly brittle linear elastic material is considered. These simplifications lead to a small number of field equations, the 3-D equilibrium equations, and one phase-field equation.

Wheeler et al. [76, 85-87, 90, 100] extended the phase-field theory accounting for poroelasticity. They adopt the quasi-static single-phase Biot theory. They provided mathematical proof for the well-posedness and uniqueness of the solution of the phase-field method in hydraulic fracture. Miehe et al. [1, 78, 82-84, 101] developed a similar variational approach to phase-field modeling. Lastly, Wilson and Landis [61] proposed a

general theory for phase-field modeling in hydraulic fracture incorporating finite deformation and non-linear material behavior. This dissertation is an extension of that work, and the theoretical formulation will be presented in Chapter 3.

Chapter 3. Methodology

The basic phase-field theory for fracture in brittle materials is presented in Section 3.1. This will serve as preliminary to the more general theory of hydraulic fracture presented in Section 3.2. In Section 3.2, the governing balance law equations, kinematics, and constitutive equations for both the fluid and solid materials will be presented (for more details see [61]). The tension-compression split schemes, the degradation functions used to degrade the load-carrying capacity of the material, and the functions to transition from Darcy to Stokes flow will be described. The numerical methods used to solve the model will be then outlined. For the purpose of comparing simulations with experiments conducted by other researchers, the experimental setups and procedures are also briefly presented.

3.1 Phase-Field Theory of Fracture in Brittle Materials

Consider an arbitrary body V with boundary surface S containing the discrete, discontinuous surfaces S_C due to the presence of cracks. We assume those surfaces S_C are traction free. For elastic materials, Griffith's theory is adopted. Griffith's theory states that the total energy of the body is the sum of the strain energy stored in V and the fracture surface energy of S_C minus the work done by the applied traction (t_i) on the part of the boundary S and body forces (b_i) on V:

$$\Phi = \int_V \psi(\varepsilon_{ij})dV + \int_{Sc} G_c dS_c - \int_V b_i u_i dV - \int_S t_i u_i dS \quad (3.1)$$

where ψ is the elastic strain energy density and ε_{ij} is the strain tensor under the assumption of small deformation:

$$\varepsilon_{ij} = \frac{1}{2}(u_{i,j} + u_{j,i}) \quad (3.2)$$

$u_{i,j}$ are the components of the deformation gradient. G_C is the fracture surface energy. Due to the numerical difficulties associated with tracking the evolution of cracks represented by S_C, a phase-field approximation of the surface fracture energy [102] is implemented:

$$\int_{Sc} G_c dS_c \approx \int_V G_c \left[\frac{(1-\mu)^2}{4l_0} + l_0\, \mu_{,i}\, \mu_{,i}\right] dV \equiv \int_V \psi^{\mu} dV \quad (3.3)$$

where l_0 is a process zone length-scale that represents the size of the region where the phase-field parameter transitions from 0 in a fully damaged region to 1 in an intact region. Since the discrete traction-free surfaces S_C have been removed, the strain energy is modified in such a way that at the damaged region where $\mu \sim 0$ cannot carry strain energy:

$$\int_V \psi(\varepsilon_{ij})dV \rightarrow \int_V g_d(\mu)\psi(\varepsilon_{ij})dV \quad (3.4)$$

The modified strain energy is then defined as follows:

$$\psi^d(\varepsilon_{ij}, \mu) = g_d(\mu)\psi(\varepsilon_{ij}) \quad (3.5)$$

Where $g_d(\mu)$ is a degradation function that is equal to 0 when μ =0 and 1 when μ =1. It must also have its first derivative with respect to μ equal to zero when μ =0. A discussion

on the forms of this degradation function will be given later in this chapter.

Then, (3.1) becomes:

$$\Phi = \int_V \psi^d(\varepsilon_{ij}, \mu)dV + \int_V \psi^\mu dV - \int_V b_i u_i dV - \int_S t_i u_i dS \qquad (3.6)$$

The first variation of (3.6) is:

$$\delta\Phi = \int_V \left[\left(\frac{\partial\psi^d}{\eth\varepsilon_{ij}}\right)_{,j} + b_i\right]\delta u_i \, dV$$

$$+\int_V \left[\frac{\partial\psi^d}{\eth\mu} + \frac{\partial\psi^\mu}{\eth\mu} - \left(\frac{\partial\psi^\mu}{\eth\mu_{,i}}\right)_{,i}\right]\delta\mu \, dV \qquad (3.7)$$

$$+\int_S \left[\left(\frac{\partial\psi^d}{\eth\varepsilon_{ij}}n_j - t_i\right)\delta u_i + \left(\frac{\partial\psi^\mu}{\eth\mu_{,i}}\, n_i\right)\delta\mu\right] dS = 0$$

where n_i is the unit vector normal to the surface *S*. Noting that (3.7) holds for arbitrary variations of u_i and μ, we conclude that:

$$\left.\begin{array}{lll} \left(\frac{\partial\psi^d}{\eth\varepsilon_{ij}}\right)_{,j} + b_i = 0 & \text{in} & V \\ \frac{\partial\psi^d}{\eth\mu} + \frac{\partial\psi^\mu}{\eth\mu} - \left(\frac{\partial\psi^\mu}{\eth\mu_{,i}}\right)_{,i} = 0 & \text{in} & V \\ \frac{\partial\psi^d}{\eth\varepsilon_{ij}}n_j = t_i & \text{on} & S \\ \frac{\partial\psi^\mu}{\eth\mu_{,i}}\, n_i = 0 & \text{on} & S \end{array}\right\} \qquad (3.8)$$

A decomposition of the strain energy ψ^d is usually implemented to make sure that the degradation of the load-carrying capacity only results from tensile stress. The total elastic strain energy ψ^d is further modified as follows:

$$\psi^d(\varepsilon_{ij}, \mu) = g_d(\mu)\, \psi^+(\varepsilon_{ij}) + \psi^-(\varepsilon_{ij}) \tag{3.9}$$

where ψ^+ and ψ^- are the parts of the strain energy due to tensile and compressive strains, respectively. Later in this dissertation, different tension-compression split approaches will be presented.

3.2 General Phase-Field Theory of Hydraulic Fracture

The coupling nature of the continuum mechanics, different fluid regimes through intact porous solid and cracks, the evolution of the phase-field parameter identifying the cracks, will be presented. The crack is identified by a phase-field function $\mu(x_i)$; inside the crack $\mu = 0$ and in the intact medium far from the crack $\mu = 1$. The fluid flow inside the crack is assumed to be Stokes flow, while the fluid in the intact material obeys Darcy flow. To account for the transition between these two regimes the theory requires the use of finite deformations to account for the opening of the crack into a finite volume where the stokes flow occurs. The general theory is presented in the reference configuration where the spatial domain V_0 is surrounded by surface S_0. It contains material points identified by the Cartesian coordinates X_I. However, in the current configuration, the spatial domain V surrounded by surface S contains material points that are identified by Cartesian coordinates x_i. The deformation gradient F_{iJ} relates the current and reference configurations as follows:

$$F_{iJ} = \frac{\partial x_i}{\partial X_J} \tag{3.10}$$

Throughout the theory, the uppercase indices refer to the reference configuration, the lowercase indices refer to the current configuration, and repeated indices indicate summation. Moreover, the subscript *s* refers to the solid, and *f* refers to the fluid.

The relations between the surface elements in the reference and current configurations are as follows:

$$n_i dS = JF_{Ji}^{-1} N_J dS_0 \tag{3.11}$$

and the relationship between the volume elements in the reference and current configurations are:

$$dV = JdV_0 \tag{3.12}$$

where n_i and N_I are unit normals to the surface in the current and the reference configurations, respectively and J is the determinant of the deformation gradient F_{iJ}.

3.2.1 MASS BALANCES:

Mass balances are developed individually for both solid and fluid materials. For the solid material; the conservation of the mass is as follows:

$$\frac{D}{Dt}[(1-\phi)\rho^s J] = 0 \tag{3.13}$$

Where ϕ is the fraction of porosity in the aggregate in the reference configuration. The matrix is assumed to be filled with fluid at all times, ρ^s is the mass density of the solid. For the fluid, the conservation of mass is as follows:

$$\frac{D}{Dt}[\phi\rho^f J] + [\rho^f \widetilde{w}_I]_{,I} = \rho^f \widetilde{m} \tag{3.14}$$

where ρ^f is the mass density of the fluid, $\widetilde{w}_I$ is the nominal fluid flux that is related to the true flux, as $w_i = \widetilde{w}_K F_{iK}/J$, and $\widetilde{m}$ is the external source of fluid volume injected per unit of the reference volume.

3.2.2 MOMENTUM BALANCES

The momentum balances equations are also developed individually for solid and fluid. The linear momentum balance equation for the solid is:

$$\left(P_{Ji} - \phi T_{Ji}\right)_{,J} + \check{b}_i^s = (1-\phi) J \rho^s \dot{v}_i \tag{3.15}$$

where P_{Ji} are the first Piola–Kirchhoff stress components in the aggregate, T_{Ji} are the first Piola–Kirchhoff stress components in the fluid, $\check{b}_i^s$ is the external body force acting on the solid per unit aggregate reference volume and $\left[\ \dot{}\ \right]$ is the time derivative. The relation between the first Piola–Kirchhoff stress P_{Ji} and the nominal surface traction is $\tilde{t}_i = P_{Ji} N_J$ on the surface S_0. The first Piola–Kirchhoff stress P_{Ji} and Cauchy stress σ_{ji} are related as $\sigma_{ji} = \frac{F_{jK} P_{Ki}}{J}$.

The linear momentum balance equation for the fluid is:

$$\left(\phi T_{Ji}\right)_{,J} + \check{b}_i^f + \check{f}_i^{sf} = \phi \rho^f J \left(\mathring{v}_i + v_i^{f/s}\right) \tag{3.16}$$

where $\check{b}_i^f$ is the external body force acting on the fluid per unit of an aggregate reference volume, and $\check{f}_i^{sf}$ is the body-force per unit of aggregate reference volume that the solid places on the fluid. The following relation between the first Piola–Kirchhoff stress T_{Ji} and the fluid traction is adopted:

$$\tilde{t}_i^f = \phi T_{Ji} N_J = \phi\left(\tau_{ji} - p\delta_{ij}\right) J F_{Jj}^{-1} N_J \text{ on } \quad S_0 \tag{3.17}$$

where τ_{ji} is the deviatoric part of the Cauchy fluid stress, δ_{ij} is the Kronecker delta, and p is the pressure. The fluid time derivative ($\overset{\circ}{(\ )}$) is for an observer that moves with the fluid. For any field variable a, the fluid time derivative is,

$$\overset{\circ}{(a)} = \dot{a} + a_{,i} v_i^{f/s} = \dot{a} + a_{,K} F_{Ki}^{-1} v_i^{f/s} \tag{3.18}$$

Applying the angular momentum balance to the aggregate and the fluid separately implies that the Cauchy stresses are symmetric:

$$\left.\begin{aligned} P_{Ki} F_{jK} &= P_{Kj} F_{iK} \\ T_{Ki} F_{jK} &= T_{Kj} F_{iK} \end{aligned}\right\} \tag{3.19}$$

3.2.3 BALANCES OF MICRO-FORCES

Following the work of Fried, Gurtin, and others [103], changes in the phase-field variable are associated with conjugate forces driving these changes. We introduce $\tilde{\imath}$ as an external surface micro-force per-unit area of athe ggregate reference surface , $\tilde{\gamma}$ as an external body micro-force per-unit aggregate reference volume, and $\tilde{\pi}$ as an internal micro-force per-unit aggregate reference volume. Analogous to the surface traction–stress relation, we postulate that the surface micro-force $\tilde{\imath}$ is related to the material micro-force vector $\tilde{\tilde{\xi}}_I$ as follows:

$$\tilde{\imath} = \tilde{\tilde{\xi}}_I N_I \quad \text{on} \quad S_0 \tag{3.20}$$

The net balance of these micro-forces is,

$$\int_{S_0} \tilde{\imath}\, dS_0 + \int_{S_0} \tilde{\tilde{\gamma}}\, dV_0 + \int_{S_0} \tilde{\pi}\, dV_0 = 0 \tag{3.21}$$

Applying the divergence theorem to (3.21) leads to the point-wise micro-force balance equation as:

$$\tilde{\tilde{\xi}}_{I,I} + \tilde{\gamma} + \tilde{\pi} = 0 \tag{3.22}$$

3.2.4 ENERGY BALANCES

Next, the energy balance of the solid/fluid aggregate is considered. The first law of thermodynamics for aggregate is:

$$\frac{D}{Dt}\int_{V_0}\left[\tfrac{1}{2}(1-\phi)\rho^s v_i v_i + (1-\phi)\rho^s e^s\right]JdV_0$$

$$+\frac{D}{Dt}\int_{V_0}\left[\tfrac{1}{2}\phi\rho^f(v_i+v_i^{f/s})(v_i+v_i^{f/s})+\tfrac{1}{2}\phi\rho^f A v_i^{f/s}v_i^{f/s}+\phi\rho^f e^f\right]JdV_0$$

$$=\int_{S_0}\tilde{t}_i\,v_i\,dS_0+\int_{V_0}\left[\tilde{b}_i v_i+\tilde{b}_i^f v_i^{f/s}\right]dV_0+\int_{S_0}\tilde{t}_i^f v_i^{f/s}\;dS_0$$

$$+\int_{V_0}\tilde{m}\,p\;dV_0+\int_{S_0}\tilde{\imath}\,\dot{\mu}\,dS_0+\int_{V_0}\tilde{\gamma}\,\dot{\mu}\,dV_0-\int_{S_0}\tilde{q}_J N_J\,dS_0+\int_{V_0}\tilde{r}\;dV_0$$

$$-\int_{S_0}\rho^f\widetilde{w}_K N_K\left[\tfrac{1}{2}(v_i+v_i^{f/s})(v_i+v_i^{f/s})+\tfrac{1}{2}Av_i^{f/s}v_i^{f/s}+e^f\right]dS_0$$

$$+\int_{V_0}\rho^f\widetilde{m}\left[\tfrac{1}{2}(v_i+v_i^{f/s})(v_i+v_i^{f/s})+\tfrac{1}{2}Av_i^{f/s}v_i^{f/s}+e^f\right]dV_0$$

(3.23)

where $\tilde{q}_J$ are components of the net heat flux ($\tilde{q}_I=\tilde{q}_I^s+\tilde{q}_I^f$) traversing a unit reference area of the aggregate per time, $\tilde{r}$ is the total heat supply to the aggregate where $\tilde{r}=\tilde{r}^s+\tilde{r}^f$, A is the tortuosity, and e^f , e^s are the internal energy per unit mass of fluid and solid respectively.

Using the mass balances (3.13), (3.14), momentum balances (3.15), (3.16) and micro-force balance (3.22) and then applying the divergence theorem, the pointwise form for the energy balance of the aggregate is as follows:

$$(1-\phi)\rho^s \dot{e}^s + \phi J \rho^f \overset{\circ}{e}^f + \phi J \rho^f \left(\tfrac{1}{2} A \overset{\underline{f}}{v}{}_i^s \overset{\underline{f}}{v}{}_i^s \right) = \left(P_{Ji} - \phi \tilde{\tau}_{Ji}\right) v_{i,J} +$$

$$\phi \tilde{\tau}_{Ji} (v_i + \overset{\underline{f}}{v}{}_i^s)_{,J} + \phi p J \frac{\overset{\circ}{\rho}{}^f}{\rho^f} + p(\dot{\phi} J) + \left[p\left(\phi J F_{Ji}^{-1}\right)_{,J} - \tilde{f}_i^{sf} \right] \overset{\underline{f}}{v}{}_i^s +$$

$$\tilde{\xi}_I \dot{\mu}_{,I} - \tilde{\pi} \dot{\mu} - \tilde{q}_{I,I} + \tilde{r} \qquad (3.24)$$

where $\tilde{\tau}_{Ji}$ is the first Piola–Kirchhoff deviatoric stress in the fluid, and is related to its Cauchy counterpart as follows: $\tilde{\tau}_{Ji} = J F_{Jk}^{-1} \tau_{ki}$. For the solid, the energy balance is:

$$\frac{D}{Dt} \int_{V_0} \left[\tfrac{1}{2} (1-\phi) \rho^s v_i v_i + (1-\phi) \rho^s e^s \right] J dV_0 = \int_{S_0} (\tilde{t}_i - \tilde{t}_i^f) v_i \, dS_0 +$$

$$\int_{V_0} \left[\tilde{b}_i^s v_i \right] dV_0 + \int_{S_0} \tilde{\imath} \, \dot{\mu} \, dS_0 + \int_{V_0} \tilde{\gamma} \, \dot{\mu} \, dV_0 - \int_{S_0} \dot{q}_J^s N_J \, dS_0 +$$

$$\int_{V_0} (\tilde{r}^s + \tilde{r}^{fs}) \, dV_0 + \int_{V_0} \dot{\varpi}^{fs} \, dV_0 \qquad (3.25)$$

where $\tilde{r}^{fs}$ is the heat transferred to the solid by the fluid, and $\dot{\varpi}^{fs}$ is the mechanical power the fluid transfers to the solid. The relation between mechanical power and the forces the solid places upon the fluid and the pressure in the fluid is as follows:

$$\dot{\varpi}^{fs} = \tilde{f}_i^{fs} v_i + p J \dot{\phi} \qquad (3.26)$$

using equations (3.13), (3.15), (3.22) and (3.26) in (3.25), and applying the divergence theorem, the pointwise form for the first law of thermodynamics for the solid is as follows:

$$(1-\phi)\rho^s \dot{e}^s = \left(P_{Ji} - \phi\tilde{\tau}_{Ji}\right)v_{i,J} + p(\dot{\phi}J) + \tilde{\xi}_I\dot{\mu}_{,I} - \tilde{\pi}\dot{\mu} - \tilde{q}^s_{I,I} + \tilde{r}^s - \tilde{r}^{fs} \tag{3.27}$$

Subtracting (3.27) from (3.24), the first law of thermodynamics for the fluid is then:

$$\phi J\rho^f \overset{\circ}{e}{}^f + \phi J\rho^f \left(\tfrac{1}{2}A\overset{\underline{f}}{v}{}^s_i \overset{\underline{f}}{v}{}^s_i\right) = \phi\tilde{\tau}_{Ji}(v_i + \overset{\underline{f}}{v}{}^s_i)_{,J} + \phi pJ\frac{\overset{\circ}{\rho}{}^f}{\rho^f} +$$

$$\left[p\left(\phi JF^{-1}_{Ji}\right)_{,J} - \tilde{f}^{sf}_i\right]v^{f/s}_i - \tilde{q}^f_{I,I} + \tilde{r}^f + \tilde{r}^{fs} \tag{3.28}$$

3.2.5 ENTROPY INEQUALITIES

In developing the constitutive equations for both the fluid and solid materials, we must ensure that they do not violate the second law of thermodynamics. As a result, we will consider the entropy inequalities for both the solid and the fluid. The second law of thermodynamics for the solid is as follows:

$$\frac{D}{Dt}\int_{V_0}(1-\phi)\rho^s s^s J dV_0 \geq -\int_{S_0}\frac{\tilde{q}_J^s N_J}{\theta^s}\, dS_0 + \int_{V_0}\frac{\tilde{r}^s - \tilde{r}^{fs}}{\theta^s} dV_0 \tag{3.29}$$

The Helmholtz free energy density ψ^s for the solid is:

$$\psi^s = e^s - s^s\theta^s \tag{3.30}$$

where s^s is the specific entropy density of the solid and θ^s is the temperature in the solid. Using equations (3.13), (3.25), and (3.30) in equation (3.29) and applying the divergence theorem leads to the point-wise form of the second law of thermodynamics for the solid as follows:

$$(1-\phi)J\rho^s\dot{\psi}^s \leq \left[(1-\phi)\,P_{Ji}^s - \phi J F_{Ji}^{-1} p\right]v_{i,J} + p(\dot{\phi}J) + \tilde{\xi}_I\dot{\mu}_{,I} - \tilde{\pi}\dot{\mu} - \frac{\tilde{q}_J^s\theta_{,I}^s}{\theta^s} -$$

$$(1-\phi)J\rho^s s^s\dot{\theta}^s \tag{3.31}$$

It is assumed that the Helmholtz free energy of the solid can depend on the true porosity, the temperature of the solid, the temperature gradients, the phase-field parameter, the phase-field parameter gradient, and its time derivative, and the deformation gradient, as follows:

$$\psi^s = \psi^s(F_{i,J}, \theta^s, \theta^s_{,I}, \mu, \mu_{,I}, \dot{\mu}, \phi J) \tag{3.32}$$

Such that,

$$d\psi^s = \frac{\partial \psi^s}{\partial F_{i,J}} dF_{i,J} + \frac{\partial \psi^s}{\partial \theta^s} d\theta^s + \frac{\partial \psi^s}{\partial \theta^s_{,I}} d\theta^s_{,I} + \frac{\partial \psi^s}{\partial \mu} d\mu + \frac{\partial \psi^s}{\partial \mu_{,I}} d\mu_{,I} + \frac{\partial \psi^s}{\partial \dot{\mu}} d\dot{\mu} +$$

$$\frac{\partial \psi^s}{\partial (\phi J)} d(\phi J) \tag{3.33}$$

We make use of the time derivative of the deformation gradient, which is related to the velocity gradient as follows:

$$\dot{F}_{iK} = F_{jK} v_{i,j} \tag{3.34}$$

Applying equations (3.33) and (3.34) to equation (3.31) yields the following:

$$\left[(1-\phi) J\rho^s \frac{\partial \psi^s}{\partial F_{i,J}} - (1-\phi)\, P^s_{Ji} + \phi J F^{-1}_{Ji} p\right] v_{i,J}$$

$$+ \left[(1-\phi) J\rho^s \frac{\partial \psi^s}{\partial (\phi J)} - p\right] (\dot{\phi J}) + \left[(1-\phi) J\rho^s \frac{\partial \psi^s}{\partial \mu_{,I}} - \tilde{\xi}_I\right] \dot{\mu}_{,I}$$

$$+ \left[(1-\phi) J\rho^s \frac{\partial \psi^s}{\partial \mu} + \tilde{\pi}\right] \dot{\mu} + \left[(1-\phi) J\rho^s \frac{\partial \psi^s}{\partial \dot{\mu}}\right] \ddot{\mu}$$

$$+ \frac{\tilde{q}^s_I \theta^s_{,I}}{\theta^s} + (1-\phi) J\rho^s \left[\frac{\partial \psi^s}{\partial \theta^s} + s^s\right] \dot{\theta}^s + \left[(1-\phi) J\rho^s \frac{\partial \psi^s}{\partial \theta^s_{,I}}\right] \dot{\theta}^s_{,I} \leq 0 \tag{3.35}$$

Again, but now for the fluid material, the second law of thermodynamics is formulated as follows:

$$\frac{D}{Dt}\int_{V_0} \phi\rho^f s^f J dV_0 \geq -\int_{S_0} \frac{\tilde{q}_J^f N_J}{\theta^f}\, dS_0 + \int_{V_0} \frac{\tilde{r}^f + \tilde{r}^{fs}}{\theta^f} dV_0 - \int_{S_0} \rho^f \tilde{w}_J N_J s^f \; dS_0 -$$

$$\int_{V_0} \rho^f \tilde{m}\, s^f\, dV_0 \tag{3.36}$$

The Helmholtz free energy density ψ^f for the fluid materials is:

$$\psi^f = e^f - s^f \theta^f \tag{3.37}$$

where s^f is the entropy density of the fluid and θ^s is the temperature in the fluid. Using equations (3.14), (3.28), and (3.37) in equation (3.36) and applying the divergence theorem leads to the point-wise form of the second law of thermodynamics for the fluid as follows:

$$\phi J\rho^f \overset{\circ}{\psi}{}^f \leq \phi p J \frac{\overset{\circ}{\rho^f}}{\rho^f} - \phi\, J\, \rho^f s^f \overset{\circ}{\theta}{}^f + \phi\tilde{\tau}_{Ji}(v_i + \underline{v_i^s})_{,J} - \phi J\rho^f \left[\tfrac{1}{2}\overset{\circ}{A}\, \underline{v_i^s} + A\left(\overset{\circ}{\underline{v_i^s}}\right)\right] \underline{v_i^s}$$

$$+ \left[p\left(\phi J F_{Ji}^{-1}\right)_{,J} - \tilde{f}_i^{sf}\right] v_i^{f/s} - \frac{\tilde{q}_J^f \theta_{,I}^f}{\theta^f} \tag{3.38}$$

Now, it is assumed that the Helmholtz free energy of the fluid, the fluid pressure, and the entropy density of the fluid can depend only on the fluid density, the temperature of the fluid, the temperature gradients, the fluid velocity gradient as follows:

$$\psi^f = \psi^f(\theta^f, \theta_{,I}^f, \rho^f, v_{i,J}^f) \tag{3.39}$$

Such that,

$$d\psi^f = \frac{\partial \psi^f}{\partial \theta^f} d\theta^f + \frac{\partial \psi^f}{\partial \theta^f_{,I}} d\theta^f_{,I} + + \frac{\partial \psi^f}{\partial \rho^f} d\rho^f + \frac{\partial \psi^f}{\partial v^f_{i,J}} dv^f_{i,J} \tag{3.40}$$

Applying equations (3.40) to equation (3.38) gives the following:

$$\phi J \left[\rho^f \frac{\partial \psi^f}{\partial \rho^f} - \frac{p}{\rho^f}\right] \overset{\circ}{\rho}{}^f + \frac{\tilde{q}^f_I \theta^f_{,I}}{\theta^f} + \phi J \rho^f \left[\frac{\partial \psi^f}{\partial \theta^f} + s^f\right] \overset{\circ}{\theta}{}^f + \left[\phi J \rho^f \frac{\partial \psi^f}{\partial \theta^f_{,I}}\right] \overset{\circ}{\theta}{}^f_{,I} +$$

$$\left[\phi J \rho^f \frac{\partial \psi^f}{\partial v^f_{i,J}}\right] \left(\overset{\circ}{v}{}^f_{i,J}\right) + \phi J \rho^f \left[\frac{1}{2} \overset{\circ}{A}\, \overset{f}{v}{}^s_i + A \left(\overset{\circ}{\overset{f}{v}{}^s_i}\right)\right] \overset{f}{v}{}^s_i -$$

$$\left[p\left(\phi J F^{-1}_{Ji}\right)_{,J} - \tilde{f}^{sf}_i\right] \overset{f}{v}{}^s_i - \phi \tilde{\tau}_{Ji} v^f_{i,J} \leq 0 \tag{3.41}$$

In the next section, we will make the use of equations (3.35) and (3.41) to obtain the restrictions on the constitutive relations that are proposed.

3.2.6 Solid and Fluid Free Energies and Constitutive Relations

The solid free energy potential Ω^s will be proposed that will be called the "poro-enthalpy." It can be derived from the Helmholtz free energy using a Legendre transformation as follows:

$$(1 - \phi_0) J_0 \rho^s_0 \Omega^s = (1 - \phi_0) J_0 \rho^s_0 \psi^s - Jp\phi \tag{3.42}$$

Substituting equation (3.42) in equation (3.35) leads to:

$$(1-\phi)J\rho^s\dot{\Omega}^s \leq \left[(1-\phi)\,P^s_{Ji} - \phi J F^{-1}_{Ji} p\right] v_{i,J} - \phi J\,\dot{p}$$

$$+\tilde{\xi}_I \dot{\mu}_{,I} - \tilde{\pi}\dot{\mu} - \frac{\tilde{q}^s_J \theta^s_{,I}}{\theta^s} - (1-\phi)J\rho^s s^s \dot{\theta}^s \tag{3.43}$$

We still have not made the use of equations (3.35), (3.41), and (3.43). These equations must hold for all admissible processes associated with the variables $F_{i,J}, \theta^f, \theta^f_{,I}, \mu, \phi, \rho^f, v^f_{i,J}, \theta^s, \theta^s_{,I}, \mu, \mu_{,I}, \dot{\mu},$ and ϕJ [104]. As a result, the constitutive relations for the solid are as follows:

$$\left.\begin{aligned}
&(1-\phi_0)\,P^s_{Ji} = (1-\phi_0)J_0\rho^s_0 \frac{\partial \Omega^s}{\partial F_{i,J}} + \phi J F^{-1}_{Ji} p \\
&\tilde{\xi}_I = (1-\phi_0)J_0\rho^s_0 \frac{\partial \Omega^s}{\partial \mu_{,I}} \\
&\phi J = -(1-\phi_0)J_0\rho^s_0 \frac{\partial \Omega^s}{\partial p} \\
&s^s = -\frac{\partial \Omega^s}{\partial \theta^s} \\
&\frac{\partial \Omega^s}{\partial \dot{\mu}} = \frac{\partial \Omega^s}{\partial \theta^s_{,I}} = 0 \\
&\tilde{\pi} = -(1-\phi_0)J_0\rho^s_0 \frac{\partial \Omega^s}{\partial \mu} - \beta\dot{\mu} - \eta_I \theta^s_{,I} \\
&\tilde{q}^s_I = -\tilde{\eta}_I \dot{\mu} - \kappa^s_{IJ}\theta^s_{,I}
\end{aligned}\right\} \tag{3.44}$$

We make use of the fact that the mass balance for the solid is as follows:

$$(1-\phi)J\rho^s = (1-\phi_0)J_0\rho_0^s \tag{3.45}$$

Similar to that for the solid, the fluid constitutive equations emerge from its entropy inequality as follows:

$$\left.\begin{aligned}
&p = (\rho^f)^2 \frac{\partial \psi^f}{\partial \rho^f} \\
&s^f = -\frac{\partial \psi^f}{\partial \theta^s} \\
&\frac{\partial \psi^f}{\partial v^f_{i,J}} = \frac{\partial \psi^f}{\partial \theta^f_{,I}} = 0 \\
&\tilde{\tau}_{Ji} = \nu_{iJkL}\left(w_{k,L} + \phi v_{k,L}\right) + \hat{\tau}_{Ji} \\
&\tilde{q}^f_I = -\kappa^f_{IJ}\theta^f_{,J} + \hat{q}_I \\
&\tilde{f}^{sf}_i = p\left(\phi J F^{-1}_{Ji}\right)_{,J} - \phi_{,J}\tilde{\tau}_{Ji} - \chi_{ij}v^{\underline{f}}_i - \phi J\rho^f\left(\tfrac{1}{2}\overset{\circ}{A}\, v^{\underline{f}}_i - A\left(\overset{\circ}{v^{\underline{f}}_i}\right)\right) + \hat{f}^{sf}_i
\end{aligned}\right\} \tag{3.46}$$

Where, ν_{iJkL} is the positive definite material tensors of the fluid viscosity, κ^f_{IJ} the thermal conductivity of the fluid, and χ_{ij} is the fluid impermeability of the porous solid. Next, we propose a poro-enthalpy for reversible, hyper-elastic, isothermal materials as follows:

$$(1-\phi_0)J_0\rho_0^s\Omega^s = \psi\left(F_{i,J},\mu\right) - [\alpha + (1-\alpha)g_m(\mu)](J-1)p -$$
$$[1-g_m(\mu)]\frac{p^2}{2N} - \phi_0 p + \frac{G_c}{4l_0}\left[(1-\mu)^2 + 4l_0^2\mu_{,I}\mu_{,I}\right] \tag{3.47}$$

where $\psi(F_{i,J}, \mu)$ is the strain energy density, which includes a degradation function that will be discussed later in more detail. As for the material constants, α is the Biot coefficient, N is the Biot tangent modulus, and G_c is Griffith's critical energy release rate. The relation between N, α, and ϕ_0 [105] is as follows:

$$\frac{1}{N} = \frac{(\alpha - \phi_0)(1-\alpha)}{K} \tag{3.48}$$

Where K is the bulk modulus of the aggregate. The linear momentum equation for the fluid (3.16) will be modified by the assumption of isothermal creepy Newtonian flow. The following constitutive relations are proposed to reproduce Stokes flow in the crack and Darcy flow in intact regions:

$$\tau_{ij} = g_S(\mu)\nu^f \left[w_{i,j} + w_{j,i} - \tfrac{2}{3}w_{k,k}\delta_{i,j} + \phi\left(v_{i,j} + v_{j,i} - \tfrac{2}{3}v_{k,k}\delta_{i,j}\right)\right] \tag{3.49}$$

$$\tilde{f}_i^{sf} = p\left(\phi J F_{Ji}^{-1}\right)_{,J} - \phi_{,J}\tilde{\tau}_{Ji} - g_D(\mu)\phi J \frac{\nu^f}{\kappa} w_i \tag{3.50}$$

where ν^f is the fluid viscosity and κ is the isotropic intrinsic permeability for the intact material. Two indicator functions have been introduced into the constitutive relations: $g_S(\mu)$ for Stokes flow and $g_D(\mu)$ for Darcy flow. The structure of these functions and what conditions must be satisfied will be discussed in the following section.

The free energy ψ^f for the fluid is proposed in such a way that we allow for the fluid to be compressible, as follows:

$$\psi^f = \frac{1}{c^f}\left(\frac{\rho_0^f}{\rho^f} + ln(\rho^f)\right) \tag{3.51}$$

A linearized relationship between the density and the pressure is derived from (4.46) and (3.51) as follows:

$$\rho^f = \rho_0^f + c^f p \tag{3.52}$$

In the absence of the micro-force balance governing the phase-field parameter, and the Stokes flow for the fluid in the cracks, the formulation presented above recovers non-linear poroelastic theories that agree with the Biot's classical theory [106-108].

3.2.7 SCHEMES FOR TENSION-COMPRESSION SPLITS

As motivated by the fact that only tensile stresses should derive damages, the strain energy is decomposed into two parts: ψ^- and ψ^+. These two parts of the strain energy represent the compressive and the tensile parts of the strain energy, respectively. The idea is that a crack should not develop under purely compressive principal stresses. Therefore, the phase-field degradation function $g_d(\mu)$ will be applied only to the tensile part of the strain energy as follows:

$$\psi(\varepsilon_{ij}, \mu) = g_d(\mu)\, \psi^+(\varepsilon_{ij}) + \psi^-(\varepsilon_{ij}) \tag{3.53}$$

As discussed previously, two approaches to the tension/compression splits will be investigated here. The first is based on the work of Miehe et al. [1] and is expressed in terms of the principal strains $\varepsilon_1, \varepsilon_2$ (for 2D plane strain) as follows:

$$\begin{aligned} \psi^+(\varepsilon_{ij}) &= \frac{Ev}{2(1+v)(1-2v)}\langle \varepsilon_{kk}\rangle^2 + \frac{E}{2(1+v)}(\langle \varepsilon_1\rangle^2 + \langle \varepsilon_2\rangle^2) \\ \psi^-(\varepsilon_{ij}) &= \frac{Ev}{2(1+v)(1-2v)}\langle -\varepsilon_{kk}\rangle^2 + \frac{E}{2(1+v)}(\langle -\varepsilon_1\rangle^2 + \langle -\varepsilon_2\rangle^2) \end{aligned} \tag{3.54}$$

where the bracket 〈 .. 〉 is the Macaulay bracket defined as:

$$\langle x \rangle = \frac{x+|x|}{2} \tag{3.55}$$

Another approach is based on the behavior of masonry-like materials. This type of material exhibits no resistance to tension. For such behavior, constitutive models have been constructed that prohibit tensile stress states. Among these, those of Del Piero and of Angelillo et al. proposed a constitutive model that reflects such phenomena and ensures the existence of the strain energy density [2, 3]. By assuming that $\varepsilon_1 \geq \varepsilon_2$, the tensile and compressive parts of the strain energy are decomposed as follows:

$$\left.\begin{aligned}
&\text{If } (\varepsilon_2 \geq 0), \text{ then} \\
&\quad \psi^+(\varepsilon_{ij}) = \frac{Ev}{2(1+v)(1-2v)}(\varepsilon_{kk})^2 + \frac{E}{2(1+v)}[(\varepsilon_1)^2 + (\varepsilon_2)^2] \\
&\quad \psi^-(\varepsilon_{ij}) = 0 \\
&\text{If } (\varepsilon_1(1-v) + \varepsilon_2 v \geq 0), \text{ then} \\
&\quad \psi^+(\varepsilon_{ij}) = \frac{E\,(\varepsilon_1(1-v)+\varepsilon_2 v)^2}{2(1-v)(1+v)(1-2v)} \\
&\quad \psi^-(\varepsilon_{ij}) = \frac{E\,(\varepsilon_2)^2}{2(1-v)^2} \\
&\text{If } (\varepsilon_1(1-v) + \varepsilon_2 v < 0), \text{ then} \\
&\quad \psi^+(\varepsilon_{ij}) = 0 \\
&\quad \psi^-(\varepsilon_{ij}) = \frac{Ev}{2(1+v)(1-2v)}(\varepsilon_{kk})^2 + \frac{E}{2(1+v)}[(\varepsilon_1)^2 + (\varepsilon_2)^2]
\end{aligned}\right\} \tag{3.56}$$

For both schemes, plane-strain is assumed. The constants *E* and v are the modulus of elasticity and the Poisson ratio, respectively.

3.2.8 DEGRADATION AND INDICATOR FUNCTIONS

The form of a degradation function $g_d(\mu)$ and must, at least, satisfy the following conditions [68, 83]:

$$g_d(0) = 0\,, \quad g_d(1) = 1\,, \text{ and } \quad g_d'(0) = 0 \tag{3.57}$$

The form of the degradation function $g_d(\mu)$ that predominates in the literature is:

$$g_d^q(\mu) = \mu^2 \tag{3.58}$$

This quadratic form [102] has the advantage that it is simple to implement in the "staggered" solution scheme (i.e. solve u_i with fixed μ, then solve μ with fixed u_i, and alternate until certain convergence criteria are achieved) because both sets of equations are linear for the simplest manifestation of the theory. Another form that has some attractive features was proposed by Borden et al. [71]:

$$g_d^c(\mu) = \mu^2[s(\mu - 1) - 2\mu + 3] \tag{3.59}$$

where *s* is the slope at μ = 1. For $0 \leq s \ll 1$, it is called the cubic degradation function. In equation (3.47), we also introduced a phase-field function $g_m(\mu)$. This function aims to cause the porosity to approach unity inside the crack. Its requirements are as follows:

$$g_m(0) = 1, g_m(1) = 0,\ g'_m(0) = 0 \text{ and } g'_m(1) = 0 \tag{3.60}$$

Thus, a simple function that satisfies (3.60) is:

$$g_m(\mu) \equiv \begin{cases} 1 & : \quad \mu < 1 \\ 1 - 3\mu^2 + 2\mu^3 & : \quad 0 \leq \mu \leq 1 \\ 0 & : \quad \mu > 1 \end{cases} \tag{3.61}$$

The indicator functions g_S and g_D are introduced to the constitutive relations in such a way that Stokes flow occurs inside the crack and Darcy flow in the intact material. As a result, two requirements must be satisfied:

$$g_S(0) = 1 \text{ and } g_S(1) = 0 \tag{3.62}$$

$$g_D(0) = 0 \text{ and } g_D(1) = 1 \tag{3.63}$$

A simple Stokes indicator function satisfying (3.62) is proposed:

$$g_S(\mu) = (1 - \mu)^2 \tag{3.64}$$

For Darcy flow in the intact material, a specific power-law form is used:

$$g_D(\mu) = \mu^n \tag{3.65}$$

The exponent *n* is chosen in such a way that the impermeability is degraded rapidly within the crack. In the simulations, *n* = 6 is chosen. This value for *n* is further discussed in [61].

3.3 Summary for Strong and Weak Forms

To implement the finite element methods, a weak form is derived. In this section, we will summarize the governing equations in both strong and weak forms.

3.3.1 STRONG FORM:

The aggregate equilibrium equation:

$$\begin{aligned} P_{Ji,J} + \widetilde{b_i} &= 0 && \text{in } V_0 \\ P_{Ji}N_J &= \tilde{t}_i && \text{on } S_t \\ u_i &= \hat{u}_i && \text{on } S_u \end{aligned} \tag{3.66}$$

Kinematics:

$$F_{iJ} = \delta_{iJ} + u_{i,J} \tag{3.67}$$

Micro-force balance equation:

$$\begin{aligned} \tilde{\xi}_{I,I} + \tilde{\gamma} + \tilde{\pi} &= 0 && \text{in } V_0 \\ \tilde{\xi}_I N_I &= \tilde{\imath} && \text{on } S_i \\ \mu &= \hat{\mu} && \text{on } S_\mu \end{aligned} \tag{3.68}$$

The fluid mass balance:

$$\frac{1}{\rho^f}\frac{D}{Dt}(\phi\rho^f J) + \left(JF_{Ji}^{-1}w_i\right)_{,J} + \frac{\rho^f_{,J}}{\rho^f}JF_{Ji}^{-1}w_i - \tilde{m} = 0 \quad \text{in } V_0 \tag{3.69}$$

Linear momentum equations for the fluid:

$$\begin{aligned}
&\left(\tau_{ji}JF_{Jj}^{-1}\right)_{,J} - JF_{Ji}^{-1}p_{,J} - g_D(\mu)\frac{\nu^f}{\kappa}Jw_i = 0 && \text{in } V_0 \\
&\left(\tau_{ji} - p\delta_{ij}\right)JF_{Jj}^{-1}N_J = \tilde{t}_i^f && \text{on } S_f \\
&w_i = \hat{w}_i && \text{on } S_w \\
&p = \hat{p} && \text{on } S_p
\end{aligned} \tag{3.70}$$

3.3.2 WEAK FORM

The following equation serves as a weak form for the finite element implementation:

$$\begin{aligned}
&\int_{V_0}\left[P_{Ji}\delta F_{iJ} + \tilde{\xi}_I\delta\mu_{,I} - \tilde{\pi}\delta\mu\right]dV_0 + \int_{V_0}\left[\left(\tilde{\tau}_{Ji} - pJF_{Ji}^{-1}\right)\delta w_{i,J} + g_D(\mu)\frac{\nu^f}{\kappa}Jw_i\delta w_i\right]dV_0 \\
&+ \int_{V_0}\left[-\left(\frac{1}{\rho^f}\frac{D}{Dt}(\phi\rho^f J) + JF_{Ji}^{-1}w_{i,J} + \frac{\rho^f_{,J}}{\rho^f}JF_{Ji}^{-1}w_i\right)\delta p\right]dV_0 \\
&= \int_{V_0}\left[\tilde{b}_\iota\delta u_i + \tilde{\gamma}\delta\mu - \tilde{m}\delta p\right]dV_0 + \int_{S_0}\left[\tilde{t}_\iota\delta u_i + \tilde{\iota}\delta\mu + \tilde{t_\iota^f}\delta w_i\right]dS_0
\end{aligned} \tag{3.71}$$

The constitutive relations are:

$$P_{Ji} = g_d(\mu)\frac{\partial \psi^+}{\partial F_{iJ}} + \frac{\partial \psi^-}{\partial F_{iJ}} - [\alpha + g_m(\mu)(1-\alpha)]JF_{Ji}^{-1}p + \phi\tilde{\tau}_{Ji} \tag{3.72}$$

$$\tilde{\pi} = -g_d'(\mu)\psi^+(F_{ij}) + \frac{G_c}{2l_0}(1-\mu) + g_m'(\mu)\left[(1-\alpha)(J-1)p - \frac{1}{2N}p^2\right] \tag{3.73}$$

$$\widetilde{\xi_I} = 2G_c l_0 \mu_{,I} \tag{3.74}$$

$$\phi = \frac{1}{J}\left\{\phi_0 + [\alpha + g_m(\mu)(1-\alpha)](J-1) + [1-g_m(\mu)]\frac{p}{N}\right\} \tag{3.75}$$

3.4 Numerical Implementations

A continuous Galerkin finite element method is used to solve the partial differential equations. We used the so-called Taylor hood (TH) [109] element that satisfies the LBB conditions [110, 111]. For two dimensional analyses, a quadrilateral TH element is used with biquadratic interpolations for the fluid velocity and bilinear interpolations for the pressure, the displacements and the phase-field variable. For three dimensional analyses, the hexahedral TH element is used with triquadratic interpolations for the fluid velocity and trilinear interpolations for the pressure, the displacements, and the phase-field variable. The partial differential equations are coupled and solved using standard Newton–Raphson methods with an implicit backward Euler integration scheme. For matrix inversion, a parallel, sparse, direct solver from the MUMPS/PETSc library is used [112].

3.5 Experimental Method

It is imperative to compare the model simulations with experimental results where possible. This will not only validate the model but also provide insights into the experimental observations. To accomplish this, we will compare the model with experiments carried by AlTammar [4].

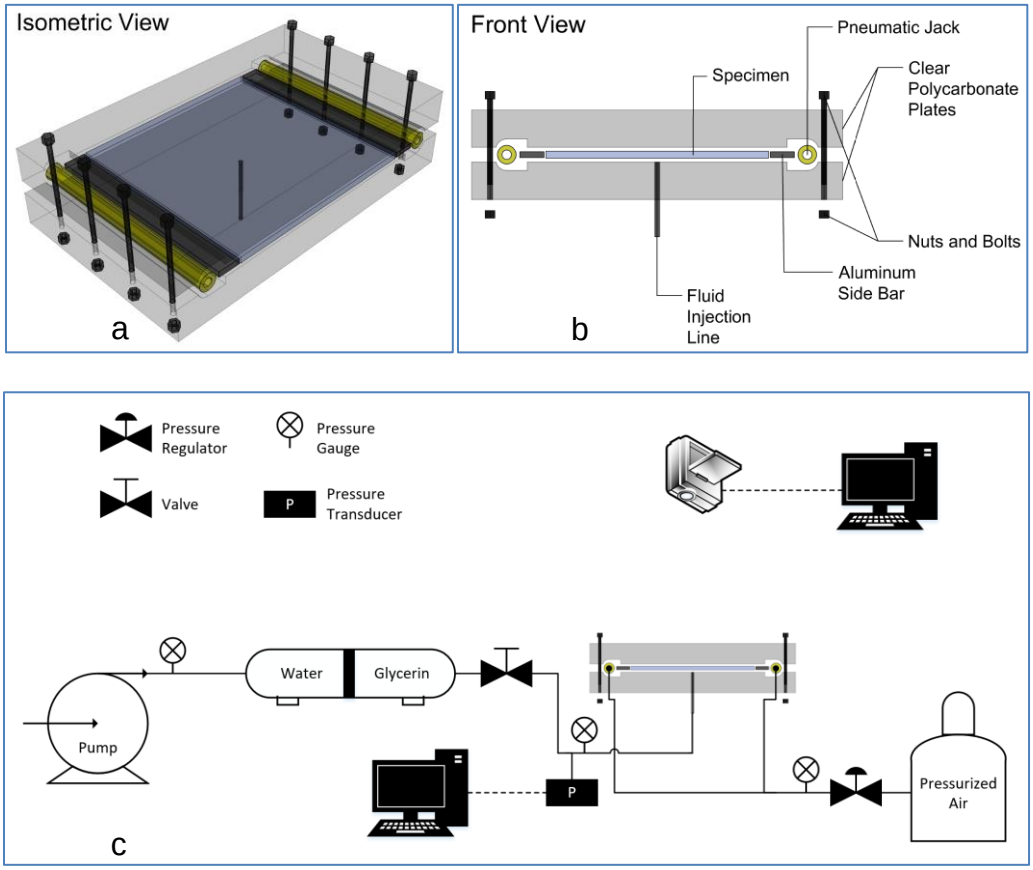

Figure 3.1: Schematic of fracture cell (a & b) and layout of experimental setup (c) (source [43]).

Figure 3.1 shows the experimental layout. A test specimen with the dimensions of 152 mm x 52 mm x 5.1 mm has a hole with 3.2 mm diameter at its center. The far-field stress is applied on the two opposite-parallel sides via pneumatic jacks. Glycerin is injected at the center hole to initiate the crack. On the top and the bottom surfaces of the specimen, two thin flexible adhesive layers are used to prevent fluid leakage. The fracture growth is monitored using a high-resolution digital camera. These experiments aim to study the effect of the inclusions on the crack growth. Therefore, an oblique inclusion with a 25 mm length and a variable thickness is cast and placed at a variable distance away from the injection port (see Figure 3.2).

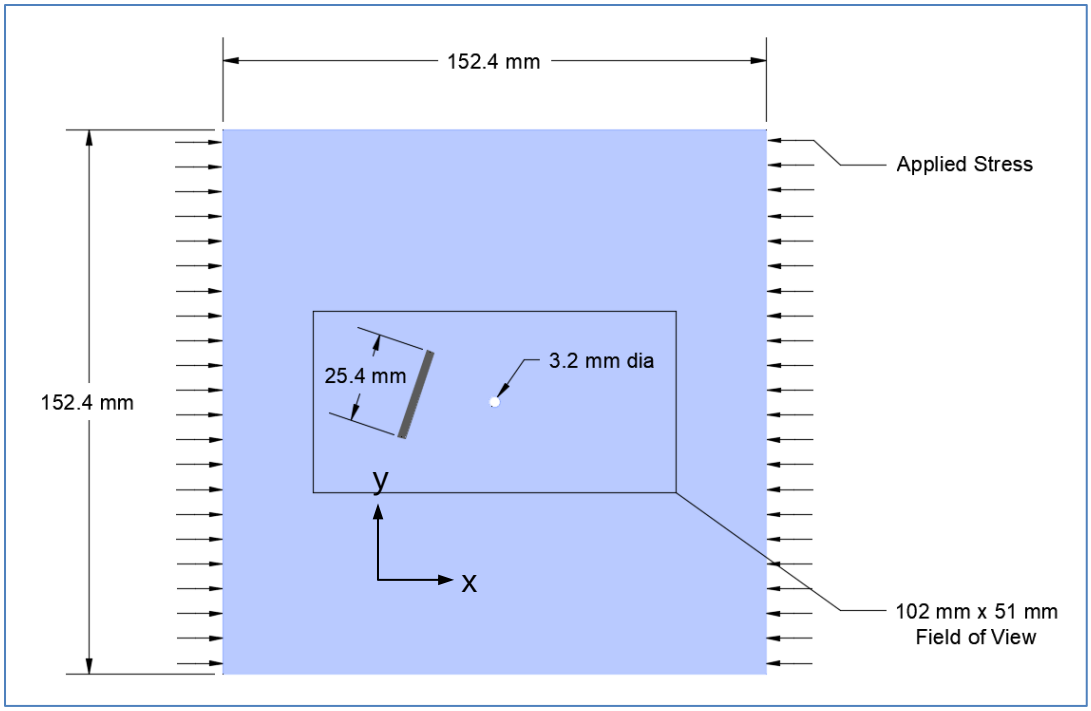

Figure 3.2: Configuration of test specimen as used in the fracturing tests (source [43]).

Four tests were performed to study four factors that can influence the crack growth: 1) the tough-stiffness of the inclusions, 2) the thickness, 3) the distance, and 4) the oblique angle. The matrix of the test specimens is made of plaster. The tough-stiff inclusions are cast using Hydrostone, while weak-soft inclusions are cast using a mixture of 80% plaster and 20% talc by weight. The far-field stress, the material proprieties, the fluid viscosity, and the inclusion dimensions/orientation are listed and discussed in Chapter 4.

Chapter 4. Results and Discussions

In this Chapter, phase-field modeling simulations of hydraulic fractures are presented and compared to experimental observations. However, before detailing these calculations, we first address an outstanding issue regarding the proper representation of the strain energy that does not allow for damage under purely compressive principal stresses. Two approaches are investigated: Miehe's split approach [1], and an approach based on the masonry-like materials constitutive model [2, 3].

Thereafter, the phase-field simulations that are related to applications that are relevant to fracture treatments in the oil and gas industries are presented. The behavior of multiple fluid-driven fractures has attracted interest in optimizing the design of the fracture spacing in hydraulic fracture treatments. Additionally, it is vital to understand the behavior of fluid-driven fracture growth in the presence of natural cracks. Hydraulic fracture treatments can activate natural fractures and increase the connectivity of the overall fracture network. However, the presence of natural fractures can also alter the orientation of the hydraulic fractures toward unfavorable directions and possibly terminate their growth. Furthermore, with regard to optimizing the re-fracturing treatment, it of interest to consider how old fractures filled with proppant can influence the crack path of the induced fractures. In addition, the influence of heterogeneities on fracture growth is studied. The problem of an induced fracture interacting with a layer of different material is studied. As in-situ stresses are considered to have a significant impact on the entire fracture treatment, the problem of a fluid-driven crack under the influence of different far-field stresses is

studied. Finally, some natural fractures can have a finite opening and are filled/cemented with different materials. To understand how the induced fracture interacts with such inclusion-like cemented natural fractures, a list of experiments performed by Altammar [4] is presented, discussed, and simulated using the phase-field approach. The simulation results are in close agreement with the experimental results. Lastly, the phase-field model is extended to three-dimensions, and two benchmark problems are simulated: 1) a compact tension CT test specimen, and 2) a circular crack is driven by pressurized fluid.

4.1 Tension-Compression Split Schemes

From a phenomenological point of view, it is necessary to formulate a constitutive model that is consistent with the fact that fracture should not propagate under compression. For brittle materials, compressive stresses should not cause the evolution of damage, but rather only contribute to the material's deformation. In contrast, tensile stresses are drivers for fracture and crack growth. Therefore, within the phase-field framework, the strain energy must be decomposed in such a way as to take this seemingly obvious behavior into account. To do this, the strain energy is decomposed into tensile and compressive parts, and only the tensile part is degraded as follows:

$$\psi(\varepsilon_{ij}, \mu) = g_d(\mu)\, \psi^{+}(\varepsilon_{ij}) + \psi^{-}(\varepsilon_{ij}) \tag{4.1}$$

Note that the phase-field degradation function $g_d(\mu)$ is applied only to the tensile part of the strain energy ψ^{+}. Two approaches are studied: 1) Miehe's approach [1], and 2) an approach introduced based on a masonry-like material constitutive model [2, 3]. In general, principal strains at a point can be in one of three states: all tensile strains (extension), all compressive strain (contraction), and mixed tensile and compressive strains. In two-dimensional analyses, three states are used throughout this discussion: case ++, case+-, and case --. The first, case ++ is for both principal strains greater than zero, and the degradation function is applied to the total strain energy. The case -- is when both principal strains are negative, and no degradation function is applied at all to the strain energy density. Finally case +- is for one positive and one negative principal strains, and the degradation function is only applied to the tensile part of the strain energy density.

For Miehe's approach, the criterion used to split the strain energy into the tensile and compressive parts is:

$$\psi^{+}(\varepsilon_{ij}) = \frac{Ev}{2(1+v)(1-2v)}\langle\varepsilon_{kk}\rangle^2 + \frac{E}{2(1+v)}(\langle\varepsilon_1\rangle^2 + \langle\varepsilon_2\rangle^2)$$
$$\psi^{-}(\varepsilon_{ij}) = \frac{Ev}{2(1+v)(1-2v)}\langle-\varepsilon_{kk}\rangle^2 + \frac{E}{2(1+v)}(\langle-\varepsilon_1\rangle^2 + \langle-\varepsilon_2\rangle^2) \quad (4.2)$$

Where,

$$\langle x\rangle = \frac{x+|x|}{2} \quad (4.3)$$

Figure 4.1 (a) shows the three cases; case ++, case +-, and case -- for the strain energy based on this split. An illustration is provided in terms of stresses, rather than strain, to give a better sense of the issues that arise in this approach. The size of the circle has no meaning, but the sectors represent the relative ratios of the principal stresses. Note that the regions for cases ++ and +- will be damaged. Now it becomes apparent that splitting the strain energy with this method can result in damage evolution under purely compressive stresses, as shown in the hatched yellow sector in Figure 4.1 (c). This non-physical situation for Miehe's split is due to the effect of Poisson's ratio. The material can reside in purely compressive stress state even if it is subjected to both tensile and compressive principal strains. Thus, Miehe's approach allows damage to develop under purely compressive stresses, which is not consistent with brittle material behavior. This suggests that it is necessary to remove the Poisson's effect found in the mixed tensile-compressive state. This can be achieved by implementing the constitutive model for masonry-like materials

presented in [2, 3]. Using the ordered principal strains $\varepsilon_1 \geq \varepsilon_2$, the strain energy is decomposed as follows:

If $(\varepsilon_2 \geq 0)$, *then*

$$\psi^+(\varepsilon_{ij}) = \frac{Ev}{2(1+v)(1-2v)}(\varepsilon_{kk})^2 + \frac{E}{2(1+v)}[(\varepsilon_1)^2 + (\varepsilon_2)^2]$$

$$\psi^-(\varepsilon_{ij}) = 0$$

If $(\varepsilon_1(1-v) + \varepsilon_2 v \geq 0)$, *then*

$$\psi^+(\varepsilon_{ij}) = \frac{E\,(\varepsilon_1(1-v)+\varepsilon_2 v)^2}{2(1-v)(1+v)(1-2v)} \tag{4.4}$$

$$\psi^-(\varepsilon_{ij}) = \frac{E\,(\varepsilon_2)^2}{2(1-v)^2}$$

If $(\varepsilon_1(1-v) + \varepsilon_2 v < 0)$, *then*

$$\psi^+(\varepsilon_{ij}) = 0$$

$$\psi^-(\varepsilon_{ij}) = \frac{Ev}{2(1+v)(1-2v)}(\varepsilon_{kk})^2 + \frac{E}{2(1+v)}[(\varepsilon_1)^2 + (\varepsilon_2)^2]$$

Figure 4.1 (b) shows how the approach based on masonry-like materials identifies the three cases based on the principal strains. In Figure 4.1 (d), the three possible cases are mapped from the principal strains to the principal stresses for a Poisson's ratio of 0.25. As seen in Figure 4.1 (d), this approach ensures that purely compressive stress states do not cause damage evolution, i.e., the hatched sector is now part of the case -- which is not degraded in any aspect.

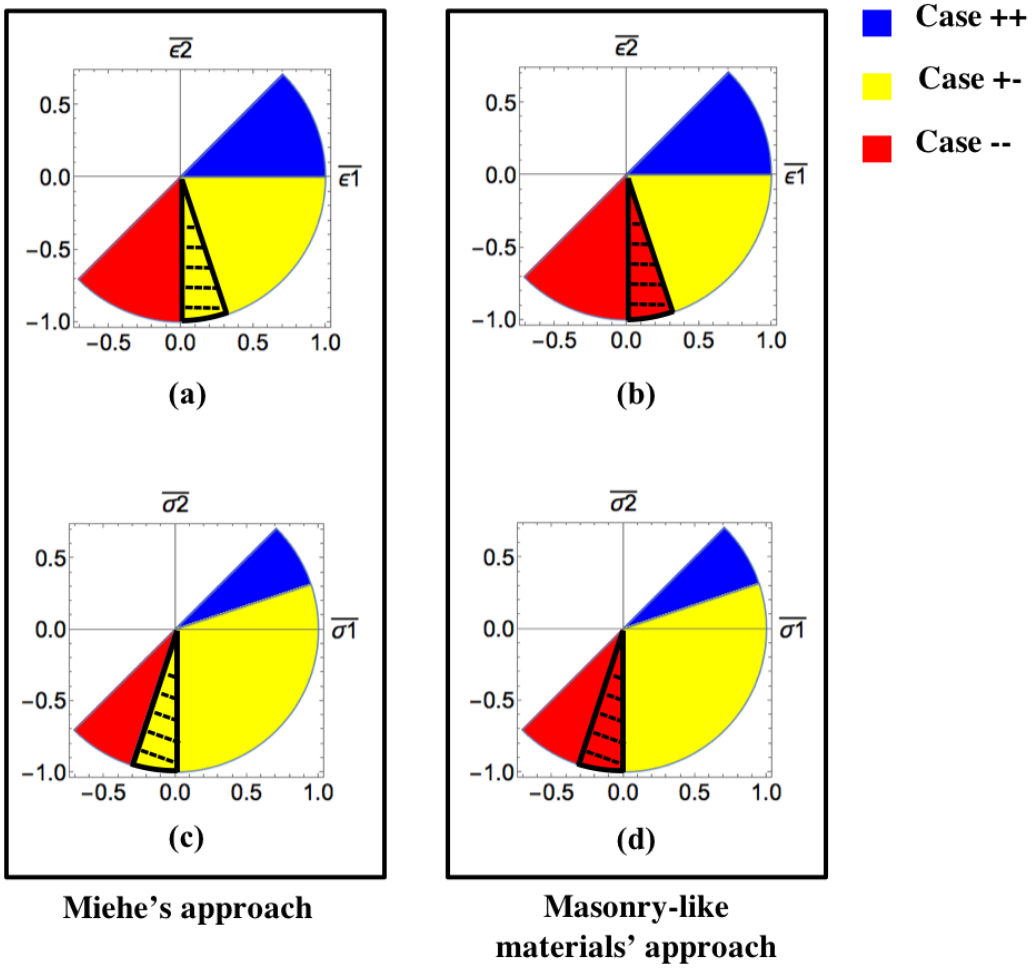

Figure 4.1: Comparison of the Miehe and the masonry-like approaches: Case ++ means the degradation function is applied to the total strain energy. The case -- means the degradation function is not applied at all. Case +- means the degradation function is only applied to the tensile part of the strain energy. (a) and (b) show the criteria for deciding which part of strain energy is degraded using principal strains arguments. (c) and (d) are a mapping of (a) and (b) to the principal stresses.

Another difference between the two approaches arises as a result of removing the Poisson's ratio effect from the part of the strain energy that is degraded. This changes the quantity of the driving force η that drives the damage evolution. Recall that the micro-force driving the crack propagation is calculated as follows:

$$\pi = \frac{\partial \psi^d}{\partial \mu} \tag{4.5}$$

The relative difference in the amount of the driving force between the two approaches can be quantified as follows:

$$\pi_d = \frac{\pi_{Miehe} - \pi_{masonry}}{\pi_{Miehe}} \ \% \tag{4.6}$$

Figure 4.2 shows the relative difference in the driving forces between the Miehe approach and the approach based on masonry-like materials. As seen in the figure, the driving force is the same for both the Miehe approach and the masonry-like material approach in the case of purely tensile strains (case ++), as expected. In the case of purely compressive principal strains (case --), the driving force is zero for both approaches. However, the difference appears in the case of mixed tensile and compressive principal strains (case +-). The differences observed are due to the removal of the Poisson's ratio effect, which is achieved in the masonry-like material approach. In general, the amount of the driving force in Miehe's approach is equal to or larger than the driving force in the masonry-like material approach. The driving force in Miehe's approach becomes higher as the larger principal stress approaches zero ($\varepsilon_1 \rightarrow 0^+$). When the material is subjected to a loading state that is "case +-" for Miehe's approach and "case --" for the masonry-like

materials approach, then the difference is 100% (see the dashed triangle in Figure 4.1 (c) and (d)). This implies that Miehe's approach predicts that damage will evolve, whereas the masonry-like material approach would predict no change in the damage state. Interestingly, loading conditions that reside in this dashed triangle can be encountered underground where the formation is under highly compressive stress states.

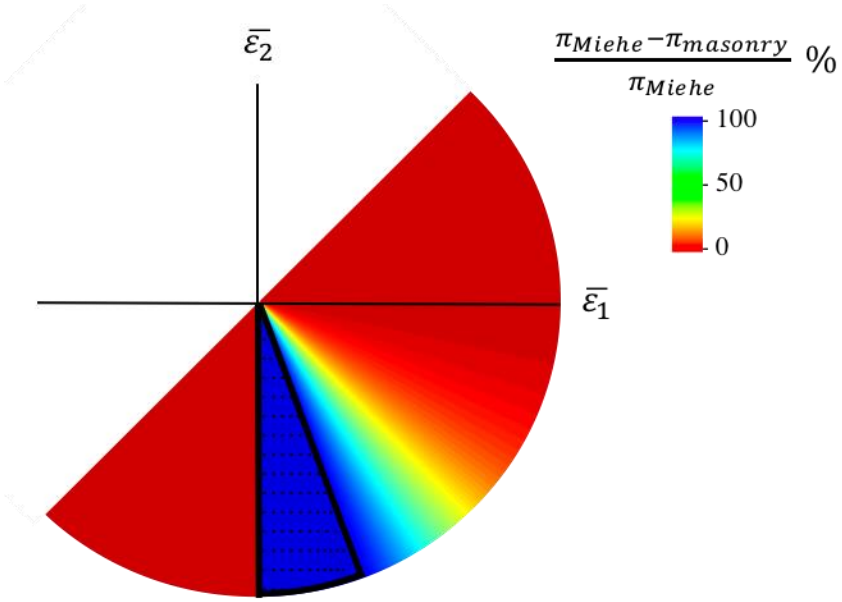

Figure 4.2: Relative difference in the driving force π associated with phase-field μ between Miehe's approach and approach based on masonry-like materials. When $\varepsilon_1 > 0$ *or* $\varepsilon_2 < 0$, the difference in the driving forces between the two approaches is zero. When $\varepsilon_1 < 0$ and $\varepsilon_2 > 0$, the relative difference in the driving force can vary from 0 (close to case ++) to 100% (inside the dashed triangle). In this triangle, the crack can grow according to Miehe's approach, but not according to the masonry-like material approach.

To illustrate the effects of these differences on the crack calculations, three load scenarios are studied: 1) shear-load, 2) purely compressive load, and 3) mixed shear-compression load scenarios. The first load scenario shows the difference in the predicted crack length between the two approaches. The last two load scenarios show the problems that arise with Miehe's approach regarding the damage evolution driven by purely compressive stresses state.

4.1.1 SHEAR-LOAD SCENARIO

Here, the differences in the magnitude of the driving force associated with the phase-field evolution are studied. To illustrate this difference, a square domain of $2000l_0$ X $2000l_0$ is simulated with a crack of length $150l_0$ placed horizontally at the center of the domain. Note that the crack faces are imposed by the mesh and not by setting the phase-field in a row of elements to zero. The phase-field at the crack tip nodes is set to zero (damaged), as seen in Figure 4.3 (a). The domain is subjected to a far-field shear strain applied at the boundaries (displacement control). Displacement control is used in order to produce stable crack growth. The boundaries are displaced incrementally to simulate a shear loading condition with u_1 (x,y = $\pm 1000l_0$) = $\pm u_0$ on the top and bottom boundaries and u_2 (x = $\pm 1000l_0$,y) = $\pm u_0$ on the right and left boundaries, as shown in Figure 4.3 (a). This ensures that the loading condition places the far-field stress state within the case +- where the Miehe and masonry-like approaches differ. Note that the strain states near the

crack tips will take on a wide range of ratios and will be inhomogeneous. Figure 4.3 (b,c) show that the difference in the crack length between the two approaches is about ~ 30% longer using Miehe's split than with the masonry-like material approach.

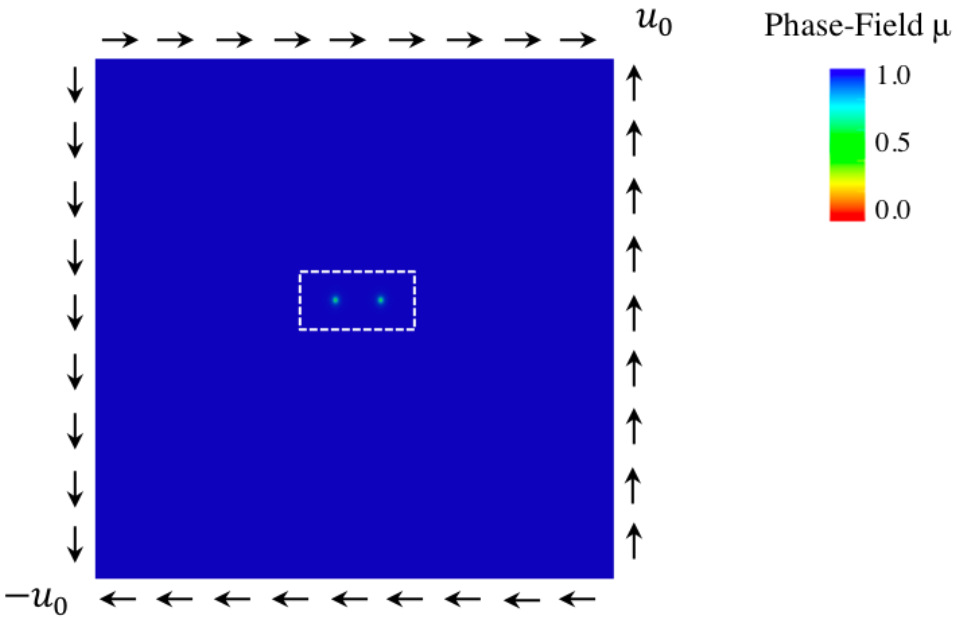

a) Boundary conditions applied

b) Using Miehe's approach

c) Using the masonry-like materials' approach

Figure 4.3: (a) A square domain of $2000l_0$ x $2000l_0$ and a real center crack of $150l_0$ undergoes far-field-shear displacements u_1 ($\pm 1000l_0$, $\pm 1000l_0$) = $\pm u_0$, u_2 ($\pm 1000l_0$, y) = $\pm u_0$. (b) Crack growth at $u_0/\varepsilon_0 l_0$ = 7.51 using the Miehe's approach. (c) Crack growth

at $u_0/\varepsilon_0 l_0$ = 7.51 using the masonry-like materials approach. Poisson's ratio ν = 0.25, ε_0 = 0.001 .

Recall that the main advantage of the approach proposed here over Miehe's approach is that Miehe's approach predicts fracture growth under purely compressive stress states while the masonry-like material approach does not. The following two cases illustrate this issue with a purely compressive and a compression-shear load case.

4.1.2 PURE COMPRESSION LOAD SCENARIO

In this case, the far-field principal stresses are both compressive, as shown in Figure 4.4 (a). Simulations were performed on a square domain of $2000l_0$ X $2000l_0$ with a $100l_0$ phase-field crack placed horizontally at the center. The compression loading condition is chosen to be $\overline{\sigma_1}/\overline{\sigma_2} = 7$. This far-field stresses ratio places the domain in the conflicting triangle (case +- in Miehe's approach and case -- in the masonry-like materials approach). As shown in Figure 4.4 (b), even though the domain is only subjected to compressive stresses, the phase-field continues to grow using Miehe's split approach. In this loading and structural state, the fracture is closed, and the phase-field should not evolve. However, as is seen in Figure 4.4 (b), the phase-field evolves around the crack. This is not physically justifiable and is an artifact of being poorly modeled by this tension-compression split. This behavior is avoided by using the masonry-like materials approach, where all strain energy goes solely to deformation for purely compressive stress states. In that approach,

the crack does not evolve, as shown in Figure 4.4 (c). These types of far-field loading conditions are pervasive during the application of fracture treatments underground. Fractures found underground are usually under compressive in-situ stresses, and thus the issues with Miehe's split will limit the capability of the phase-field model for addressing these types of problems. With the approach based on masonry-like materials, this issue is resolved.

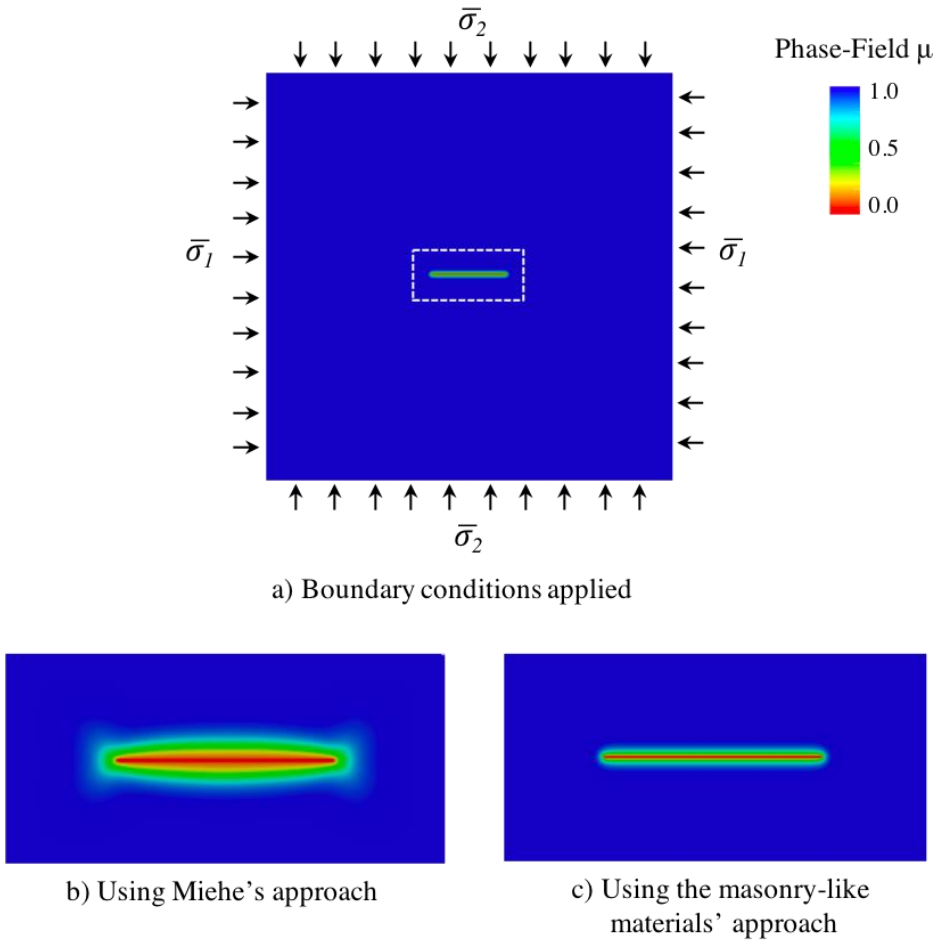

Figure 4.4: (a) A square domain of $2000l_0$ x $2000l_0$ and center crack of $100l_0$ undergoes far-field-compression (displacement-control) at an initial state. (b, c) Crack state at

$\sigma_1/\varepsilon_0 E$ = 2.42, σ_1/σ_2 = 7 , using Miehe's split and the split based on masonry-like materials, respectively. The Poisson's ratio ν = 0.25, ε_0 = 0.001.

4.1.3 SHEAR COMPRESSION LOAD SCENARIO

Finally, another load scenario is considered where the domain is subjected to far-field compression and shear stresses. The results lead to the same conclusion as the previous case. In Miehe's approach, the phase-field spreads in every direction and grows from both ends of the crack. The crack is closed, but part of the strain energy of the system flows into the phase-field evolution. This evolution of the phase-field is avoided with the masonry-like material approach.

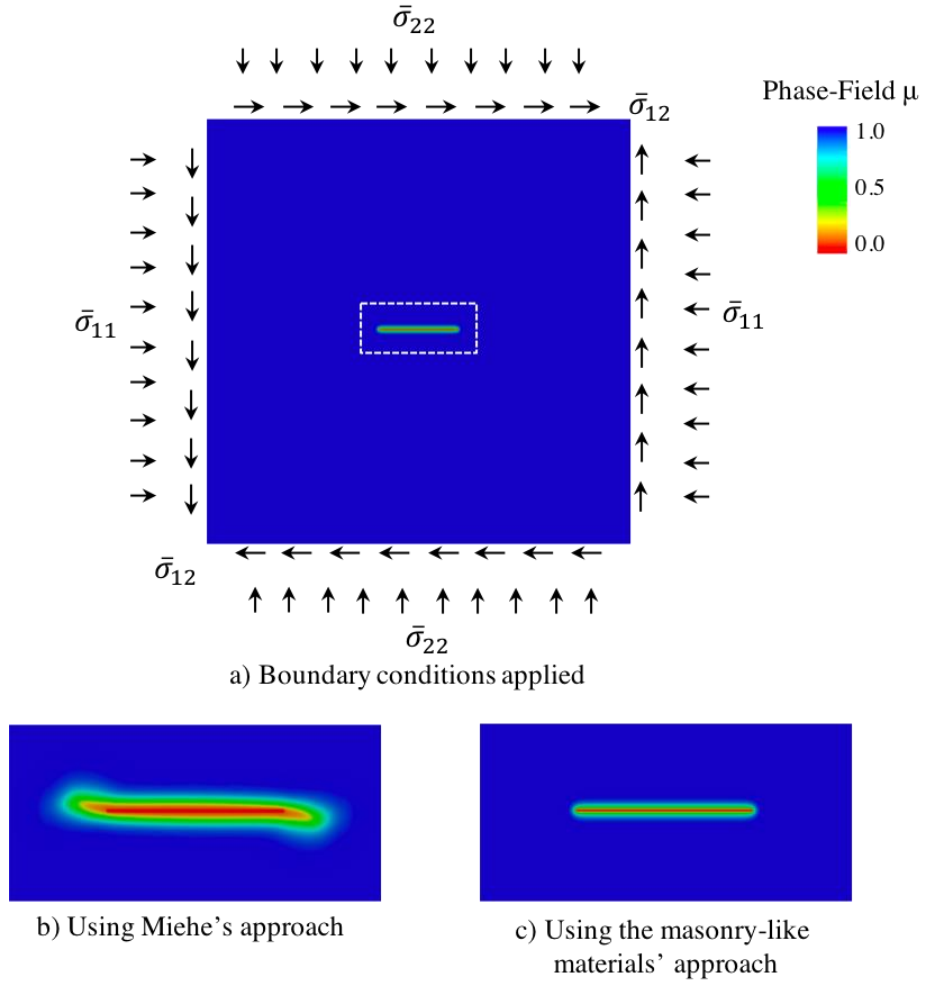

Figure 4.5: (a) A square domain of $2000l_0$ x $2000l_0$ and center crack of $100l_0$ undergoes far-field shear compression (displacement control). (b, c) Crack state at load step, $\sigma_{11}/\varepsilon_0 E$ = 1.492, $\sigma_{22}/\varepsilon_0 E$ = -0.626 , $\sigma_{12}/\varepsilon_0 E$ = 0.75, principal stresses ratio σ_1/σ_2 =10, using Miehe's split and the masonry-like split respectively. The Poisson's ratio ν = 0.25, ε_0 = 0.001.

In conclusion, an outstanding issue regarding the proper representation of the strain energy in the phase-field model has been studied and resolved. The strain energy is split into tensile and compressive parts. Miehe's approach based on a split of the principal strains was compared to a new formulation based on masonry-like materials that are elastic in compression but are unable to support any tensile stress. It has been found that Miehe's approach allows damage to evolve under purely compressive stress states. However, such behavior is avoided by the approach based on masonry-like materials. This new strain energy decomposition extends the effectiveness of phase-field modeling for hydraulic fracture, especially in regard to applying it to fracture growth under the influence of in-situ stresses.

Throughout the remainder of this chapter, the approach proposed based on masonry-like materials will be used. In the following sections, problems relevant to applications in the treatment of fractures in the oil and gas industries are studied. The main goal herein is to show how phase-field modeling can be applied to investigate various interesting problems and contribute to the understanding of fluid-driven crack propagation phenomena.

4.2 Multi-Crack Interactions

The problem of induced fractures interacting with other fractures is considered to be critical in optimizing hydraulic fracture treatments. In this section, three types of problems are studied: 1) fluid-driven parallel cracks and their application to fracturing treatments, 2) fluid-driven cracks interacting with pre-existing natural cracks, and 3) fluid-driven cracks interacting with cracks filled with proppants.

4.2.1 Induced Parallel Cracks

The problem of fluid-driven parallel cracks is relevant to fracture treatment design. In fracture treatments, the fractures are initiated using perforation tools. The fracture spacing is essential, as well as determining how many stages or "groups of fractures" there should be (see Figure 4.6). The ultimate goal in the fracture treatment design is to maximize the drainage area, as this increases the productivity of the well. One aspect of the fracture design is to choose an optimal spacing between the fractures themselves as well as between multiple stages. It seems intuitive that more fractures might result in a greater drainage area being targeted. However, an issue arises when the spacing between the fractures is small enough that initiated fractures that are longer than their neighbors exert excessive stress shadow that inhibits the shorter cracks from propagating, which would then reduce the drainage area. Therefore, studying the appropriate spacing is essential to optimizing fracturing jobs. Here, phase-field modeling can provide some insights into this problem through quantitative analysis of the stresses and fracture opening.

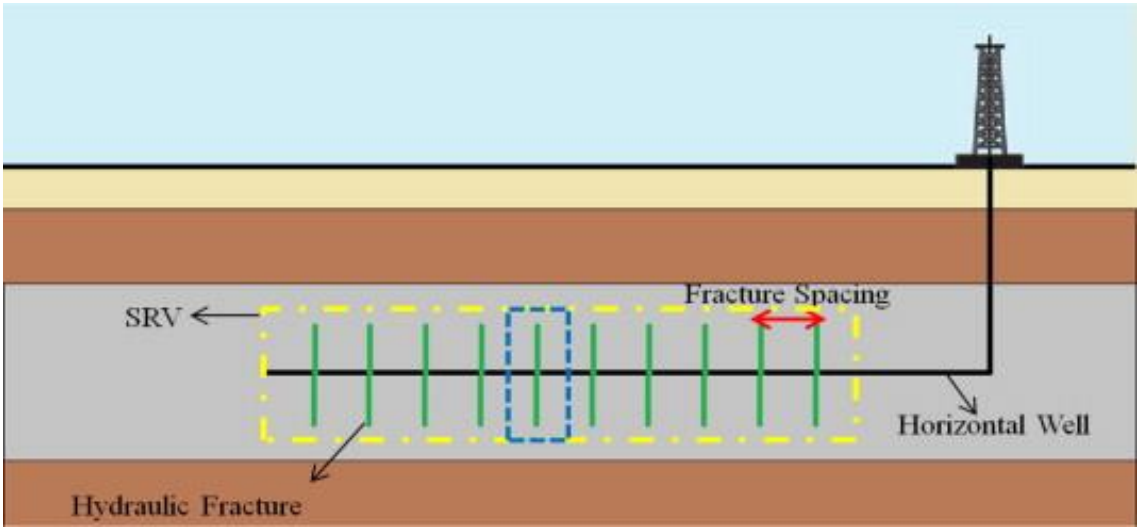

Figure 4.6: Schematic of a multi-stage fracture well. Here there is a horizontal well in a shale reservoir. Fractures are initiated and separated by a regular spacing (source [113]).

First, the most straightforward problem of multi-parallel cracks is studied. A large square domain with the dimensions of $2000l_0$ X $2000l_0$ is assumed. The advantage of any symmetries the problem contains has been taken into account. The normal displacements and normal fluid fluxes on the outer boundaries are imposed to zero (see Figure 4.7). On the centerline faces, symmetry boundary conditions are applied: the normal displacement and the shear traction are zero. Multiple cracks $90l_0$ long are initialized at the center with $20l_0$ spacings. In this problem, the Biot coefficient α is 0.45, the initial porosity is ϕ_0 = 0.1, and the normalized permeability is $\bar{\kappa}$ =10^{-14} (see Figure 4.8). Fluid is injected in the center of the cracks at a constant rate. This problem has been simulated in the literature and is considered to be a benchmark problem. Here, it is first studied to check the proposed

tension-compression split approach discussed in the previous section. It also serves as the baseline for further investigations targeting the optimization of the fracture spacing in the fracture treatment.

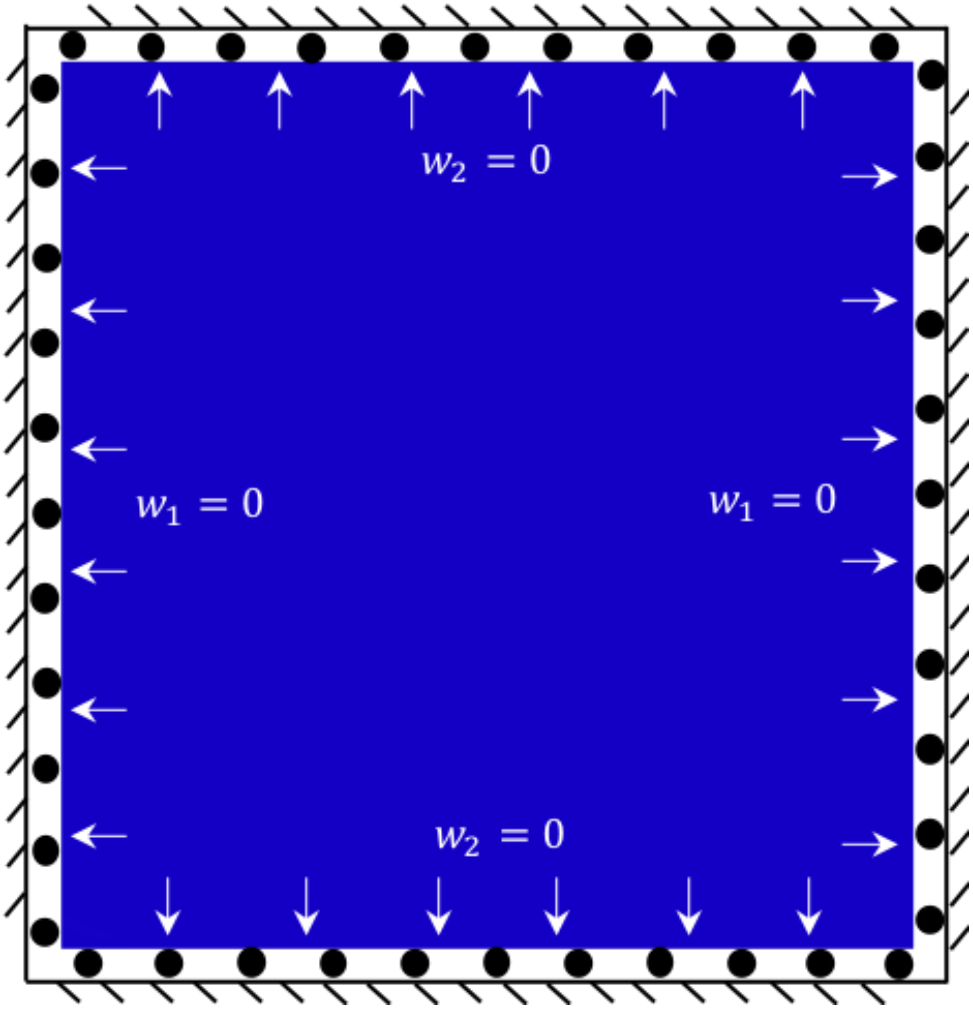

Figure 4.7: A Demonstration of boundary conditions: normal displacements, normal fluid velocities, shear stresses are zero.

Two cases are studied with this geometry: 1) the first case with two cracks and 2) a second case with four cracks. In the first case (as seen in Figure 4.8 (a)), the cracks propagate by deflecting away from each other. The angle of the deflection depends on the spacing distance [24]. For the second case (as seen in Figure 4.8 (b)), the outer cracks propagate by deflecting outward. However, the inner cracks are inhibited in their growth by the outer cracks. This is known to be the effect of the stress shadow mentioned previously. Recall that the stress shadow describes the stress induced in the region surrounding the fluid-driven fractures, and it depends on the net fluid pressure inside the cracks and their geometries [24].The propagation of the outer cracks introduces a larger stress shadow on the inner fractures, confines them, and inhibits their opening.

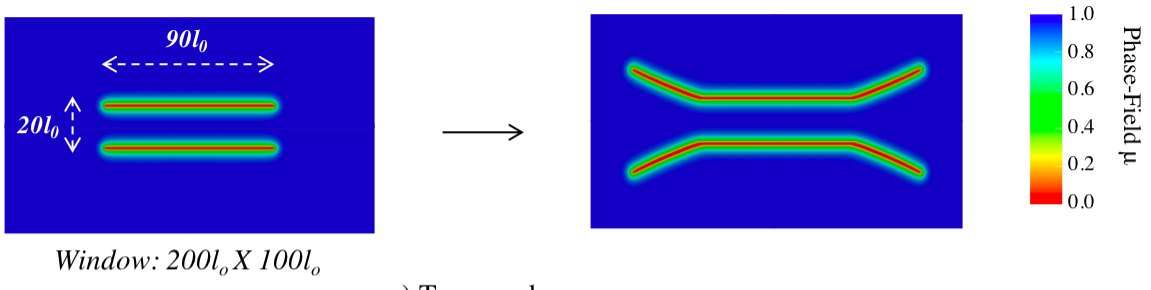

Window: $200l_o$ X $100l_o$

a) Two cracks

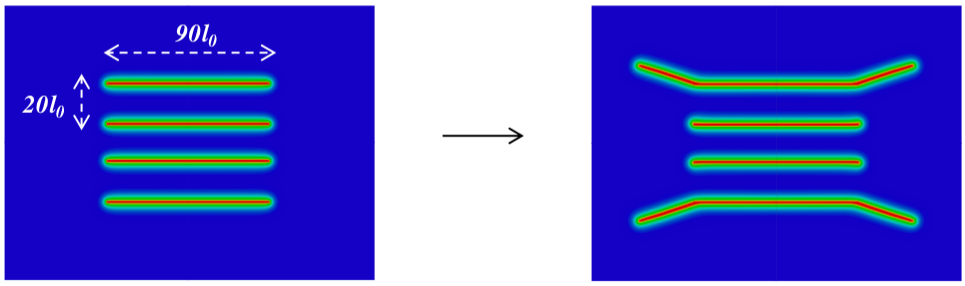

Window: $200l_o$ X $140l_o$

b) Four cracks

Figure 4.8: A square domain of $2000l_0$ x $2000l_0$ and center cracks of $90l_0$ (a) initial state for two parallel cracks → Fracture evolution for load step, $V/l_0^3 = 0.64$. (b) Initial state of four parallel cracks → Fracture evolution for load step $V/l_0^3 = 0.624$. In this problem, the Poisson's ratio $\nu = 0.25$, $\varepsilon_0 = 0.001$, $l_0^2/\kappa = 10^{14}$, $\alpha = 0.45$, $\phi_0 = 0.1$, $c^f / \rho_0^f = 0.01364$, and $\upsilon^f/E\varepsilon_0 t_0 = 5 \times 10^{-12}$.

Next, the problem of how the fracture spacing influences the propagation of the hydraulic fractures will be studied. For a considerable number of fracture stages, the domain can be divided into periodic sections. So, instead of simulating a large problem of multiple stages, only one section "Cell" can be simulated (Figure 4.9), and the computational time of the simulations will be significantly reduced.

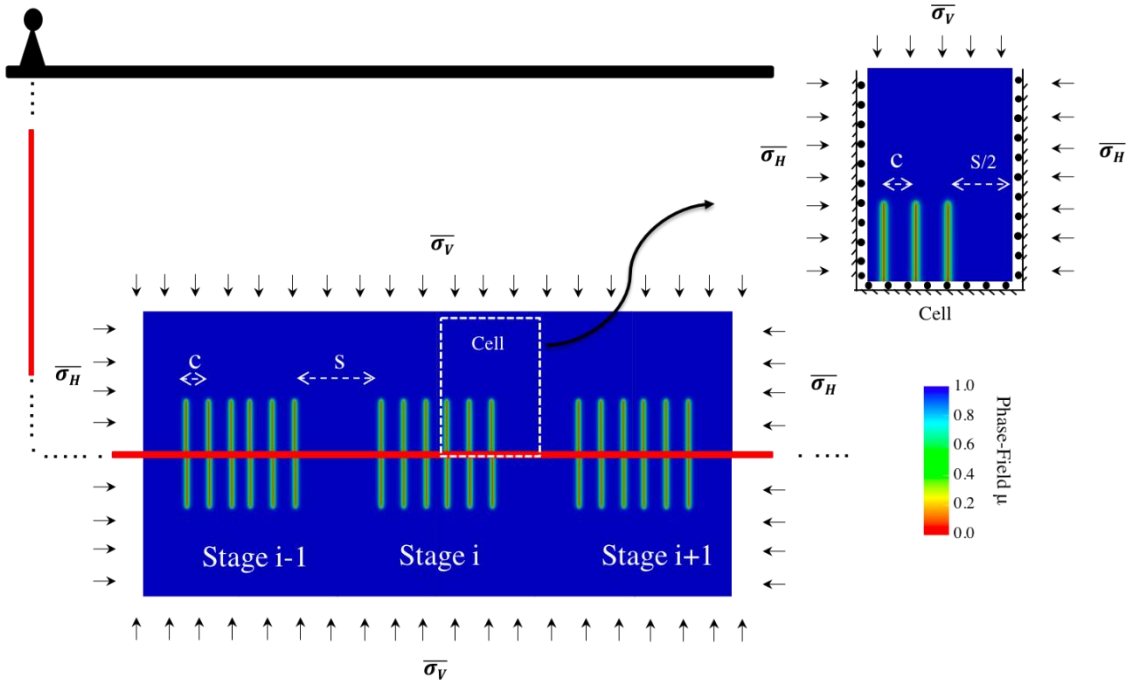

Figure 4.9: (a) Schematic of multi-stage fractures where *s* is the distance separating each stage and *c* is the spacing between cracks within a stage. (b) Schematic of the periodic section that will be simulated with symmetry boundary conditions.

The 'cell' domain with the dimensions of $135l_0$ X $1000l_0$ is assumed. The cell domain is subjected to far-field stresses (displacement control). The surface normal displacements are then fixed. The stresses are: $\bar{\sigma}_V = 0.1$ and $\bar{\sigma}_V/\bar{\sigma}_H = 6$. The surface normal fluid flux on the outer boundaries is zero. On the symmetry faces, the normal displacement is fixed, and the shear traction is zero. Multiple cracks $75l_0$ long are initialized. In this problem, the Biot coefficient α is 0.6, the initial porosity is ϕ_0 = 0.2, and

the normalized permeability is $\bar{\kappa}$ =10^{-12} (see Figure 4.8). The fluid is injected at the lower end of the cracks at a constant rate. Two cases are considered: 1) four cracks per stage and 2) six cracks per stage. For both cases, the stage spacing *S* is fixed at $130l_0$. For the case of four cracks per stage, the fracture spacing *C* is $50l_0$. For the case of six cracks per stage, the fracture spacing is *C* is $30l_0$.

In Figure 4.10, the two problems are subjected to the same far-field stresses and the same fluid injection rate. For Figure 4.10, the calculation of the stresses field for the two cases is reported just before the fractures propagate. With regard to the stress shadow effect, it is observed that $\bar{\sigma}_{11}$ (stress component that is normal to the fracture faces) in the case of six fractures per stage is more significant than $\bar{\sigma}_{11}$ in the case of four fractures per stage.

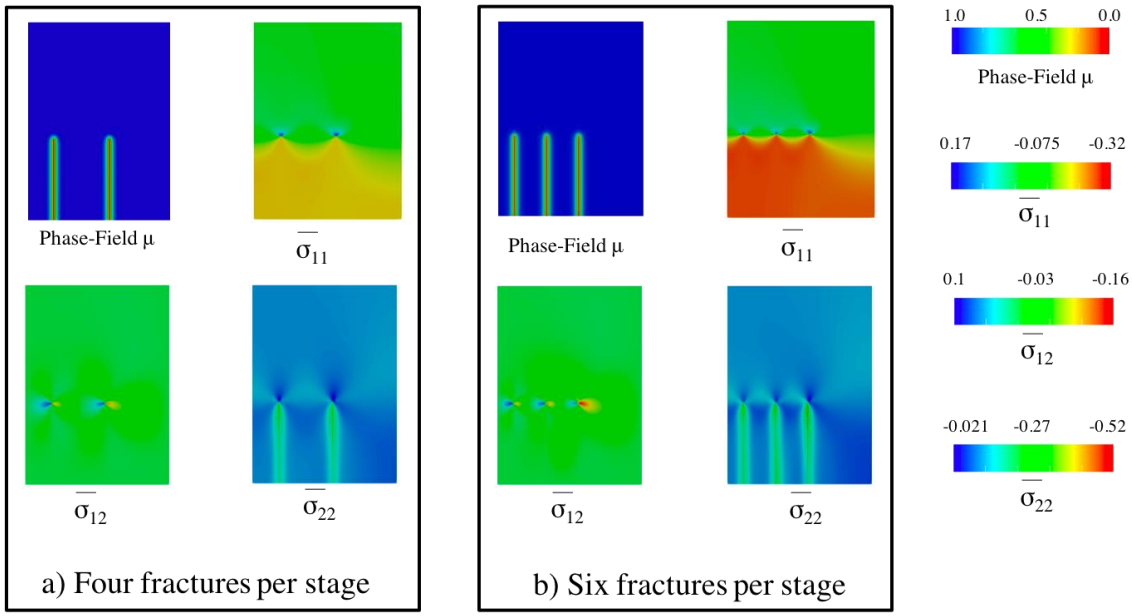

Figure 4.10: The stress field for two cases: (a) four fractures per stage; (b) six fractures per stage. σ_{11} (stress component that is normal to the fracture faces) in the case of six fractures per stage is larger than σ_{11} in the case of four fractures per stage.

Next, the influence of the fracture spacing on the crack aperture is studied. A large domain with the dimensions of $2000l_0$ X $2000l_0$ is assumed and subjected to far-field stresses (displacement control): $\bar{\sigma}_V = 0.1$ and $\bar{\sigma}_V/\bar{\sigma}_H = 6$. On the outer boundaries, the surface normal fluid flux and the shear traction are zero. Multiple cracks $150l_0$ long are initialized. In this problem, the Biot coefficient α is 0.6, the initial porosity is ϕ_0 = 0.2, and the normalized permeability is $\bar{\kappa}$ =10^{-12} (see Figure 4.8). The fluid is injected at the center of cracks, and the pressure at the injection points is controlled. As before, two cases are considered: 1) four cracks, and 2) six cracks. As seen in Figure 4.11, the outer fractures have greater crack openings than the inner fractures. Also, the crack aperture increases as the spacing *c* increases. It is interesting to note that the number of fractures per stage does not significantly influence the crack aperture for outer versus inner cracks.

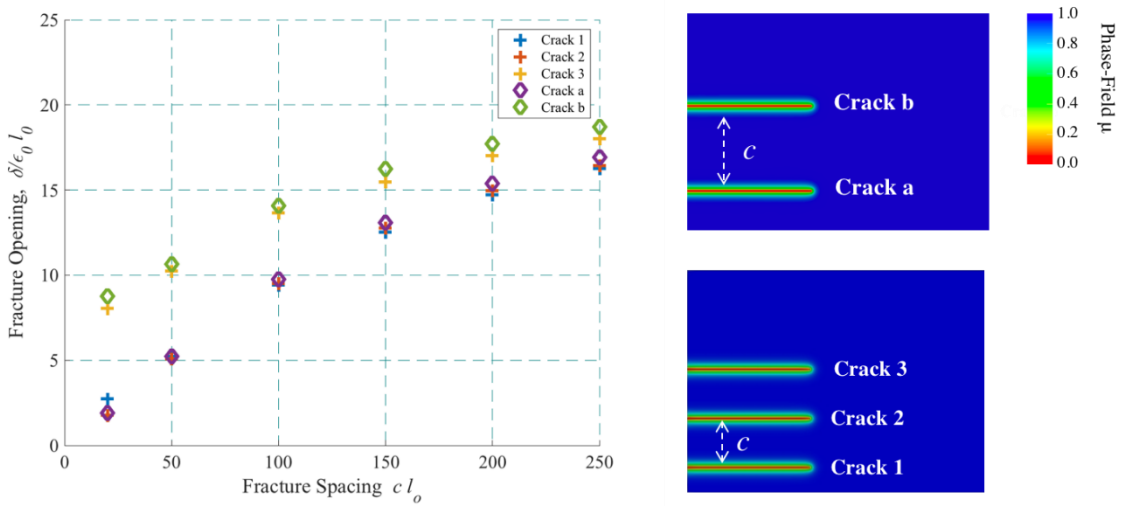

Figure 4.11: Multiple parallel fractures with different spacing c between cracks. In both cases, the outer fractures have a larger opening than the inner fractures. Also, the crack aperture increases as the fracture spacing increases.

Returning to the problem in Figure 4.9, the influence of the fracture spacing on the local stresses is studied. The local ratio $R = \bar{\sigma}_{V,ave}/\bar{\sigma}_{H,ave}$ of the average stress $\bar{\sigma}_{V,ave}$ to the average stress $\bar{\sigma}_{H,ave}$ on the boundary of the subdomain shown in Figure 4.12 (a)) is investigated. Note that this ratio R is only calculated for the square subdomain ($135l_0$ x $135l_0$) that encloses the fractures. Our goal here is to study how the local stresses contrast changes from the far-field stress to the region near the wellbore. As expected, the far-field stress field that is very far from the induced fractures is not affected by the opening of the fracture. However, near the wellbore, the stress normal to the fracture faces increases as the injected pressure increases. This suggests that the stresses near the wellbore change as

the fractures propagate. As shown in Figure 4.12 (b), the local stress ratio *R* near the wellbore drops as the fluid is injected into the fractures. The local maximum and minimum stresses near the injection site switch orientation, causing the fractures to propagate towards undesirable directions, which affect the volume of the drainage area targeted. In Figure 4.12 (c) multiple kinks in the ratio '*R*' curve-line are observed, which appear to be caused by the sequential opening of the fractures, with the outer fracture opening first, then the inner cracks as shown in the dashed lines.

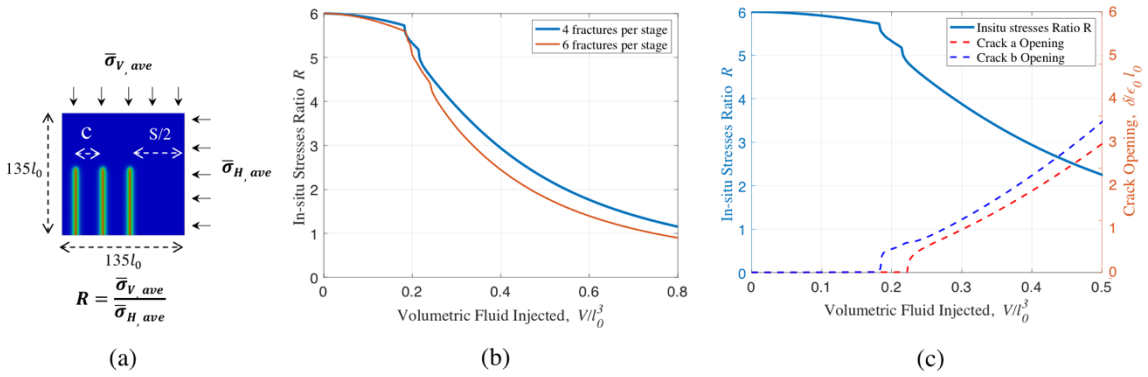

Figure 4.12: a) A schematic of the subdomain ($135l_0 x 135l_0$) that encloses the fractures. The local stresses ratio $R = \sigma_{V.ave}/\sigma_{H.ave}$ is calculated at the boundary of this subdomain only. b) The local stresses ratio *R* near the wellbore drops as the fluid is injected into the fractures. c) Multiple kinks in the ratio '*R*' curve-line are observed which appear to be caused by the sequential opening of the fractures, with the outer fracture opening first, then the inner cracks as shown in the dashed lines.

To investigate the effect of crack spacing on the propagation of hydraulic fractures, the simulations in Figure 4.10 are extended in time to observe the evolution of the cracks. As seen in Figure 4.13 (a), where the spacing c between fractures is $50l_0$, all of the initialized cracks propagate at essentially the same pace, with the outer fractures deflecting outward while the inner fractures grow ahead. For the second case shown in Figure 4.13 (b), where the spacing c between fractures is $50l_0$, the inner fractures are retarded from propagation. This suggests that increasing the number of fractures per stage by reducing the fracture spacing does not necessarily increase the drainage area and the effectiveness of hydraulic fracture treatment. In this simulation, it results in excessive stress shadowing that inhibits the internal fractures from propagating.

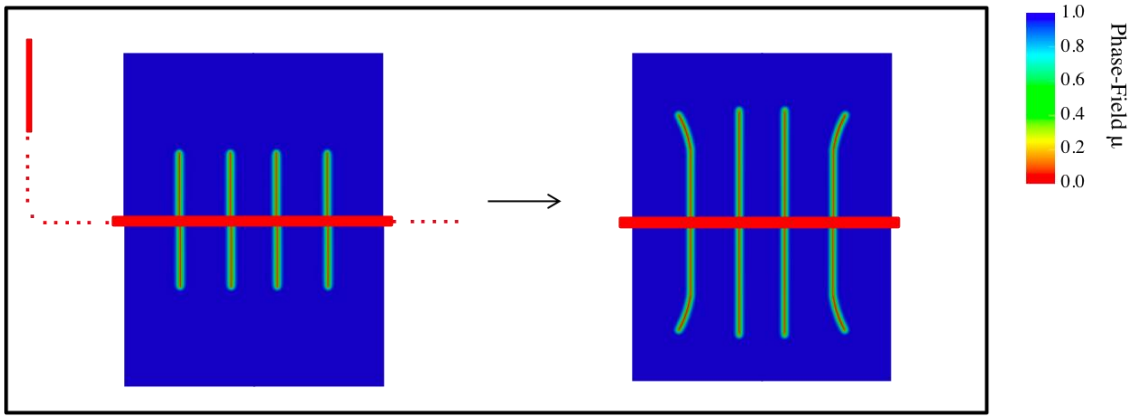

a) Four fractures per stage with spacing $c = 50\ l_0$

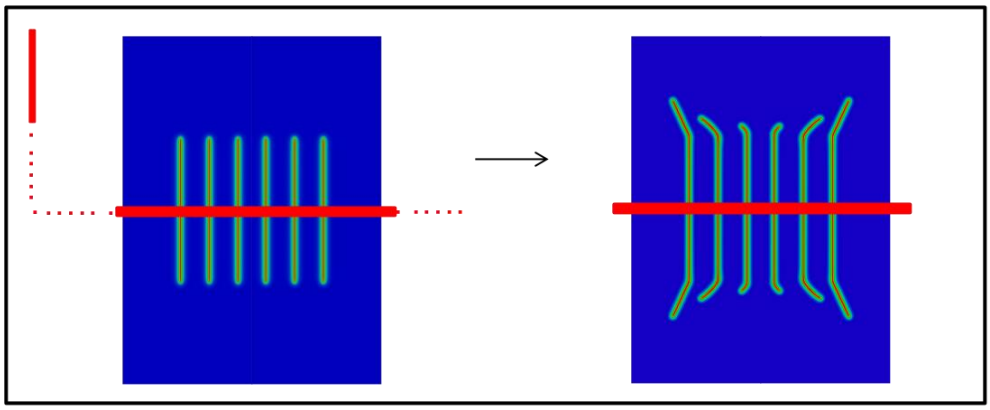

b) Six fractures per stage with spacing $c = 30\ l_0$

Figure 4.13: The propagation of four fractures per stage with an initial length of $150l_0$; a distance of $120l_0$ separates each stage a) fracture spacing of $50l_0$ within the stage. b) fracture spacing of $30l_0$ within the stage. The cell is subjected to in-situ stresses: $\sigma_V/\varepsilon_0 E$ = 0.1, $\sigma_V/\sigma_H = 6$. Poisson's ratio $\nu = 0.25$, $\varepsilon_0 = 0.001$, $l_0^2/\kappa = 10^{12}$, $\alpha = 0.6$, $\phi_0 = 0.2$, c^f / ρ_0^f = 0.001364, and $\upsilon^f/E\varepsilon_0 t_0 = 5\ x\ 10^{-10}$.

In conclusion, a model of multi-stage fracture propagation under the effect of in-situ stresses is simulated to understand the effect of the fracture spacing on the propagation. Decreasing the fracture spacing to maximize the drainage area can result in undesirable growth behavior. Reducing the fracture spacing might increase the drainage area, but only if the fractures can propagate effectively. Decreasing the fracture spacing can increase the stress shadow effect, which can prevent internal fractures from propagating, and decrease the fracture opening in general. This can negatively affect the proppant placement and well productivity.

4.2.2 THE EXISTENCE OF NATURAL CRACKS

Natural cracks are an integral part of underground formations, as has been discussed previously. Induced hydraulic fractures can activate the natural fractures and as a result, enhance the fracture network. However, natural fractures can also disturb the induced fracture growth toward undesirable directions [21]. Here, the problem of an induced hydraulic fracture interacting with natural fractures at different orientations is studied. A natural crack that is initially closed with frictionless faces is assumed. Three positions of a natural fracture placed away from the injection point are presented, as shown in Figure 4.14 (a), (b), and (c).

A large rectangular domain with the dimensions of $1000l_0$ X $2000l_0$ is simulated. The surface normal displacements and surface normal fluid flux on the outer boundaries are set to zero (see Figure 4.7). In this problem, the Biot coefficient α is 0.45, the initial

porosity is ϕ_0 = 0.1, and the normalized permeability is $\bar{\kappa}$ =10^{-14}. A fluid is injected into the left side of the horizontal crack at a constant rate. Note that this could be considered as the center of the horizontal crack for a symmetric problem.

As seen in Figure 4.14 (a), a vertical natural crack $90l_0$ long is placed $130l_0$ away from the injection point. The induced crack propagates and interacts with the natural crack. The natural fracture fills with fluid until it starts to propagate from both ends, deflecting away from vertical. In Figure 4.14 (b), a 45^0-oblique natural crack $90l_0$ long is placed $130l_0$ away from the injection point. As before, the induced crack propagates and interacts with the natural crack and fills it with fluid. After the two cracks intersect, the fracture propagates only from the upper end in this case. The opening of the induced crack exerts a compressive stress on the lower part of the natural crack and inhibits the opening near the bottom crack tip. Finally as in Figure 4.14 (c), a vertical crack $90l_0$ long is placed $130l_0$ away. The difference between this case and the first one in Figure 4.14 (a) is that the center of the crack is shifted to $25l_0$ above the induced crack axis. In this case, the induced crack propagates until it interacts with the natural crack and then the system propagates from the lower end. In this case, the opening of the induced crack exerts a greater driving force on the lower crack tip than on the upper one, and so the fracture propagates from the lower tip.

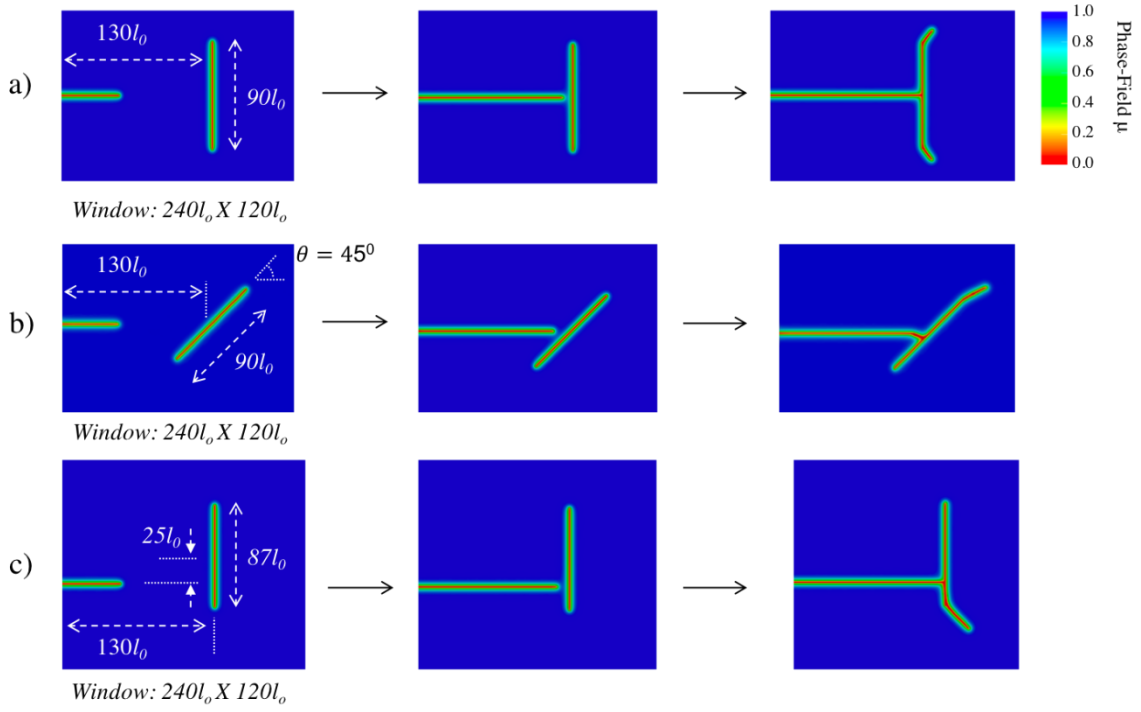

Figure 4.14: A rectangular domain of $1000l_0$ x $2000l_0$ is used with induced crack interacting with a natural closed frictionless crack is simulated. (a) Evolution of a centered vertical natural fracture. (b) Evolution of a 45°-oblique natural fracture. (c) Evolution of an off-center vertical shifted natural fracture. Poisson's ratio $\nu = 0.25$, $\varepsilon_0 = 0.001$, $l_0^2/\kappa = 10^{14}$, $\alpha = 0.45$, $\phi_0 = 0.1$, $c^f / \rho_0^f = 0.01364$, and $\upsilon^f/E\varepsilon_0 t_0 = 5 \times 10^{-12}$.

From all of the cases considered, it appears that the induced crack does not cross through the natural cracks, at least in these conditions. This suggests that natural cracks will produce more complex deflected fracture geometries. This feature may be useful for increasing the volume of the fracture network and the well conductivity, but it can also raise an issue regarding deflecting the induced fractures from their must favorable growth

directions. In any case, these preliminary investigations illustrate how natural fractures interfere with fluid-driven fractures, and that multiple mechanisms dictate the resulting crack path evolution due to these interactions.

4.2.3 ENTANGLED CRACKS

In the last section, the simulations indicate that parallel fluid-driven fractures tend to deflect away from one another where possible. However, it is not clear what may happen when parallel cracks are not centered above one another. In this section, to demonstrate the complexity of different fracture phenomena, parallel cracks are displaced both vertically and interact via their approaching crack tips, as shown in Figure 4.15. The aim is to see what happens when two induced fractures are heading toward each other. This type of problem might be encountered when the stress shadow effect near the wellbore disturbs the local in-situ stresses near the fractures and alters their propagation direction. It can also arise when cracks from different stages interact with each other. Here, two opposing fluid-driven cracks are initialized. A large rectangular domain with the dimensions of $600l_0$ X $2000l_0$ is simulated. Two cracks are separated by a vertical distance of $40l_0$. The surface normal displacements and surface normal fluid flux on the outer boundaries are set to zero. In this problem, the Biot coefficient α is 0.45, the initial porosity is ϕ_0 = 0.1, and the normalized permeability is $\bar{\kappa}$ =10^{-14} (see Figure 4.15). A fluid is injected at both the far

sides of both cracks at a constant rate. As seen in Figure 4.15, the two cracks propagate and deflect toward each other. The stress field near the cracks' tips is in compressive states.

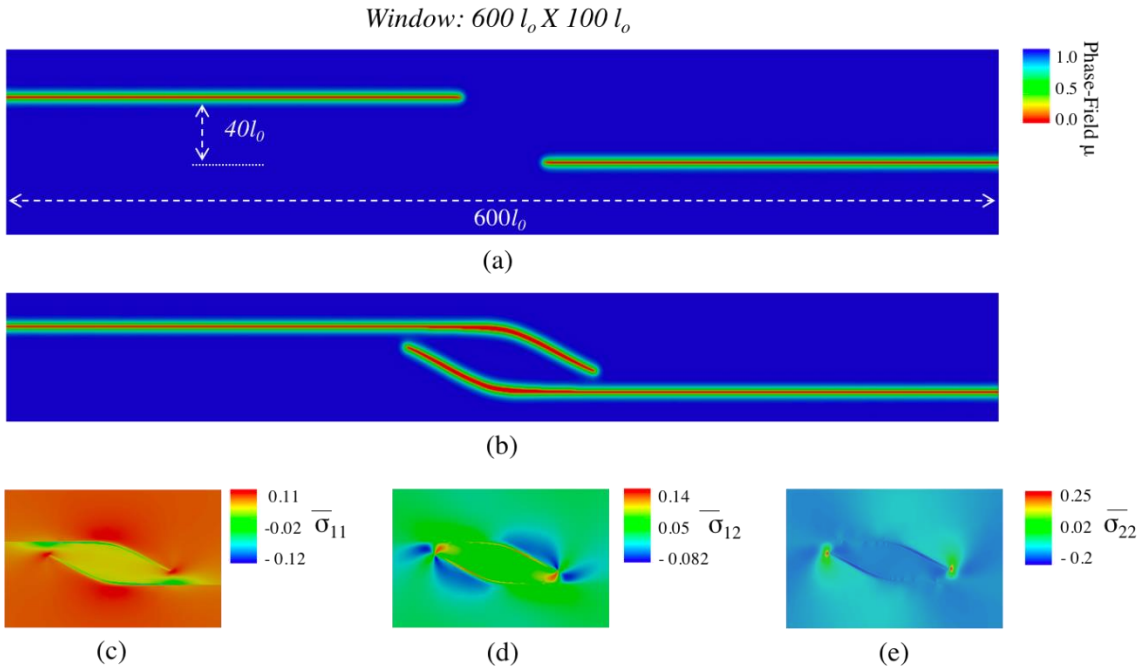

Figure 4.15: a) A rectangular domain of $600l_0$ x $2000l_0$ with two cracks each $275l_0$ long and vertically displaced by $40l_0$. b) The configuration at an injected volume of V/l_0^3 = 2.133. The Poisson's ratio $\nu = 0.25$, $\varepsilon_0 = 0.001$, $l_0^2/\kappa = 10^{14}$, $\alpha = 0.45$, $\phi_0 = 0.1$, c^f / ρ_0^f = 0.01364, and $\upsilon^f/E\varepsilon_0 t_0 = 5 \times 10^{-12}$.

4.3 Cracks Filled with Proppants

Oil production decline over time is reported in most unconventional wells [17]. One successful solution to enhancing production is a re-fracturing treatment [46]. There are two possible ways of refracturing the well: 1) refracturing the well to open the old fractures, or 2) refracturing it with new perforations placed in different orientations [47]. The second approach targets a new drainage area, especially when the in-situ stresses have been re-orientated. The propagation of new fractures can be disturbed by the presence of old fractures filled with proppant. Therefore, how these propped cracks affect the propagation of new fractures is studied here. Two factors are investigated: 1) the separation distance between the new induced fracture and the propped fracture, and 2) the crack aperture of the propped fracture. A large rectangular domain with the dimensions of $1000l_0$ X $2000l_0$ is simulated with the configuration of an induced fracture propagating towards a propped fracture placed $100l_0$ away from the injection point (as in Figure 4.16). The surface normal displacements and surface normal fluid flux on the outer boundaries are set to zero. In this problem, the Biot coefficient α is 0.45, the initial porosity is ϕ_0 = 0.1, and the normalized permeability is $\bar{\kappa}$ =10^{-14} (see Figure 4.16). A fluid is injected at the left center of the induced fracture at a constant rate.

To simulate the cracks filled with proppants, a free strain ε_f is introduced only to the damaged elements that are meant to be filled with proppant. Throughout the formulations in Chapter 3, the strain tensor is modified as follows:

$$\varepsilon_{ij} \Rightarrow \varepsilon_{ij} - \varepsilon_f \mathcal{R}_{ij} \tag{4.7}$$

where $\mathcal{R}_{ij}$ is a tensor that dictates the shape of the opening profile of the fracture. In this problem, the following form is used:

$$\mathcal{R}_{ij} = \begin{bmatrix} \nu & 0 \\ 0 & 1 \end{bmatrix} \tag{4.8}$$

The motivation behind this form is to open the crack in mode I (opening mode) only and to prevent contraction in the lateral direction due to the Poisson's ratio effect (see Figure 4.16 b). As seen in Figure 4.16 (c), opening the crack, to simulate the propped fracture, will produce a stress shadow effect in its vicinity. The free strain ε_f is chosen to have a quadratic form in terms of the crack location ''*c*'' from its center as follows:

$$\varepsilon_f = d\left(1 - \left[\frac{c}{L}\right]^2\right) \tag{4.9}$$

where *d* is the amplitude that controls the maximum opening at the center of the crack, and *L* is the half-length of the crack filled with proppant. As a result, the shape of the opening appears, as shown in Figure 4.16 (b). In this problem, a $40l_0$ long crack filled with proppant (as described above) is placed $100l_0$ away from the injection point at different vertical positions.

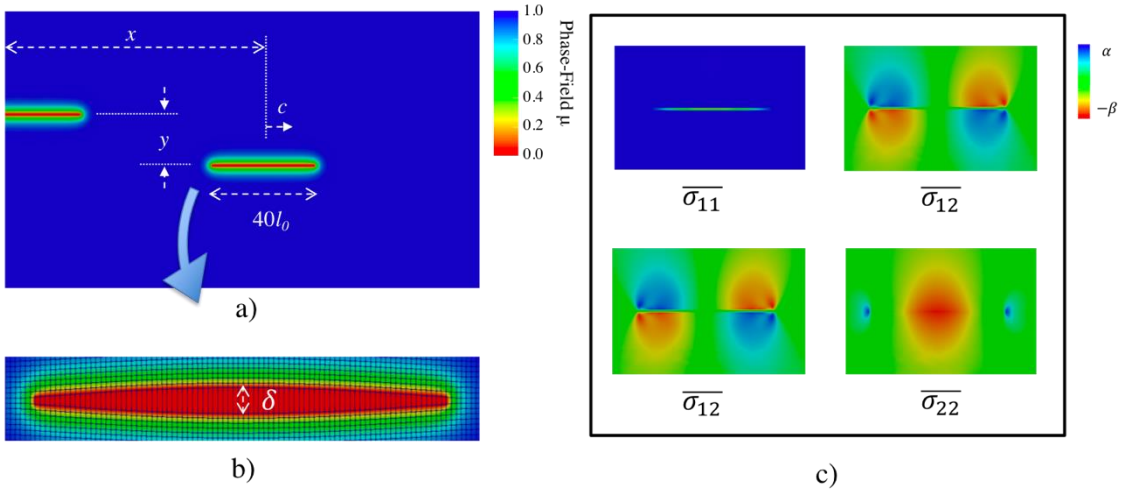

Figure 4.16: (a) A rectangular domain of $1000l_0$ x $2000l_0$ and two fractures. The distance x equals $100l_0$ throughout the simulations of this problem. The y distance varies for different cases. The length of the propped crack is $40l_0$ throughout all cases for this problem. (b) The profile of the crack opening for the free strain has a quadratic form in terms of the crack location ''c'' from its center (See Equation 4.9). (c) The resulting stress field caused by the opening of the propped crack.

The effect of the opening of the propped fracture on the propagation of the fluid-driven fracture is shown in Figure 4.17. Three different values of nominal opening of the crack are considered. As shown in Figure 4.17, when the opening of propped fracture is $\delta/\varepsilon_0 l_0 = 5.4$, the propagation path of the induced fracture is not noticeably affected. However, the length of fracture, in this case, is $10l_0$ shorter than in the case when the opening of the crack filled with proppant is zero (see Figure 4.18). So, the crack filled with proppant, in this case, appears not to affect the induced fracture path, but it does slow it

down. When the opening increases to $\delta/\varepsilon_0 l_0 = 8$, the propped fracture disturbs the induced fracture path, but not enough to fully attract it. Finally, if the opening is further increased to $\delta/\varepsilon_0 l_0 = 11.8$, the propped fracture disturbs the orientation of the in-situ stresses to the extent that the induced fracture is attracted to it until they merge. After the intersection, the fluid fills the propped fracture and it propagates.

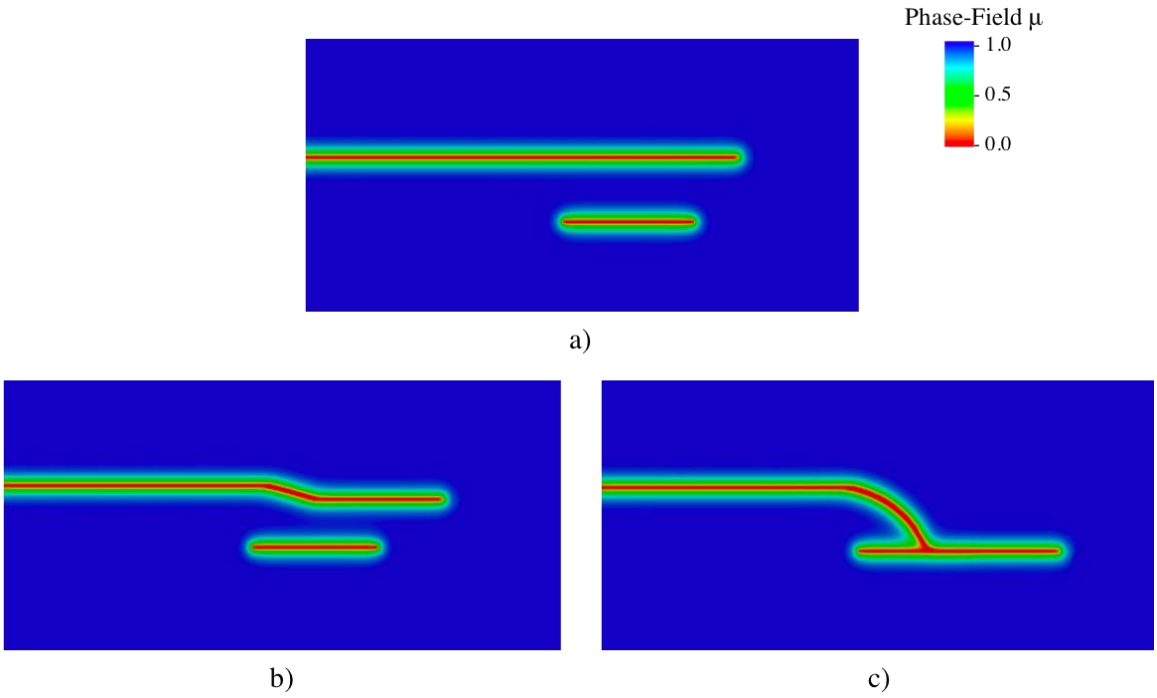

Figure 4.17: Three different proppant openings are tested for the same vertical separation distance equal to $20l_0$: a) d = 10, and $\delta/\varepsilon_0 l_0$ = 5.4 b) d = 15, and $\delta/\varepsilon_0 l_0$ = 8.0 and c) d = 22, and $\delta/\varepsilon_0 l_0$ = 11.8 . The Poisson's ratio ν = 0.25, ε_0 = 0.001, $l_0^2/\kappa = 10^{14}$, α = 0.45, ϕ_0 = 0.1, c^f / ρ_0^f = 0.01364, and $\upsilon^f/E\varepsilon_0 t_0 = 5 \times 10^{-12}$. For variable d, please see equation (4.9).

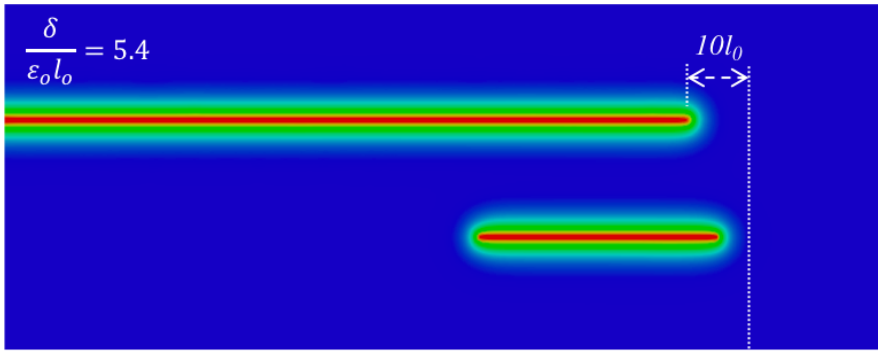

(a)

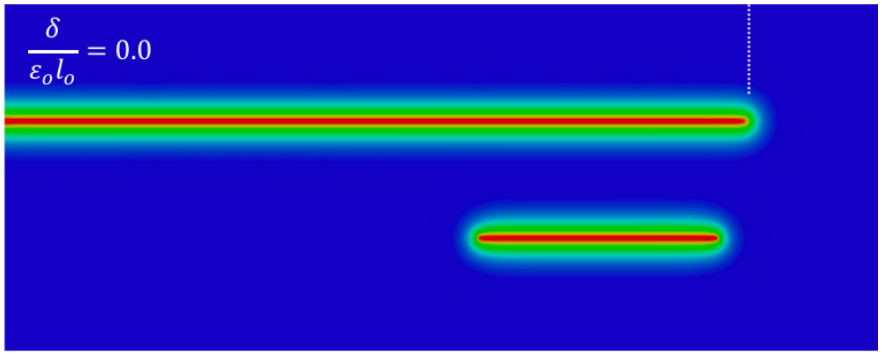

(b)

Figure 4.18: Two different proppant openings are tested for the same vertical separation distance equal to $20l_0$: a) d = 10, and $\delta/\varepsilon_0 l_0$ = 5.4 , and b) d = 0, and $\delta/\varepsilon_0 l_0$ = 0.0 . These two cases are compared at the same load step, V/l_0^3 = 1.1, to shows the effect of the crack filled with proppant on the length of the induced fracture. Poisson's ratio ν = 0.25, ε_0 = 0.001, $l_0^2/\kappa = 10^{14}$, α = 0.45, ϕ_0 = 0.1, c^f / ρ_0^f = 0.01364, and $\upsilon^f/\sigma_0 l_0^3 = 5 \times 10^{-12}$. For variable d, please see equation (4.9).

Next, the effect of different vertical distances of the propped crack on the behavior of the induced crack growth is shown in Figure 4.19. Three different distances are studied with the same opening of the propped crack $\delta/\varepsilon_0 l_0 = 5.4$. As seen in Figure 4.19, the fracture is attracted to the propped fracture when it is closest to the induced fracture plane. As the vertical displacement increases, as the effect of the propped fracture fades. For a vertical separation equal to $40l_0$, the propagation path of the induced fracture is not affected by the propped fracture.

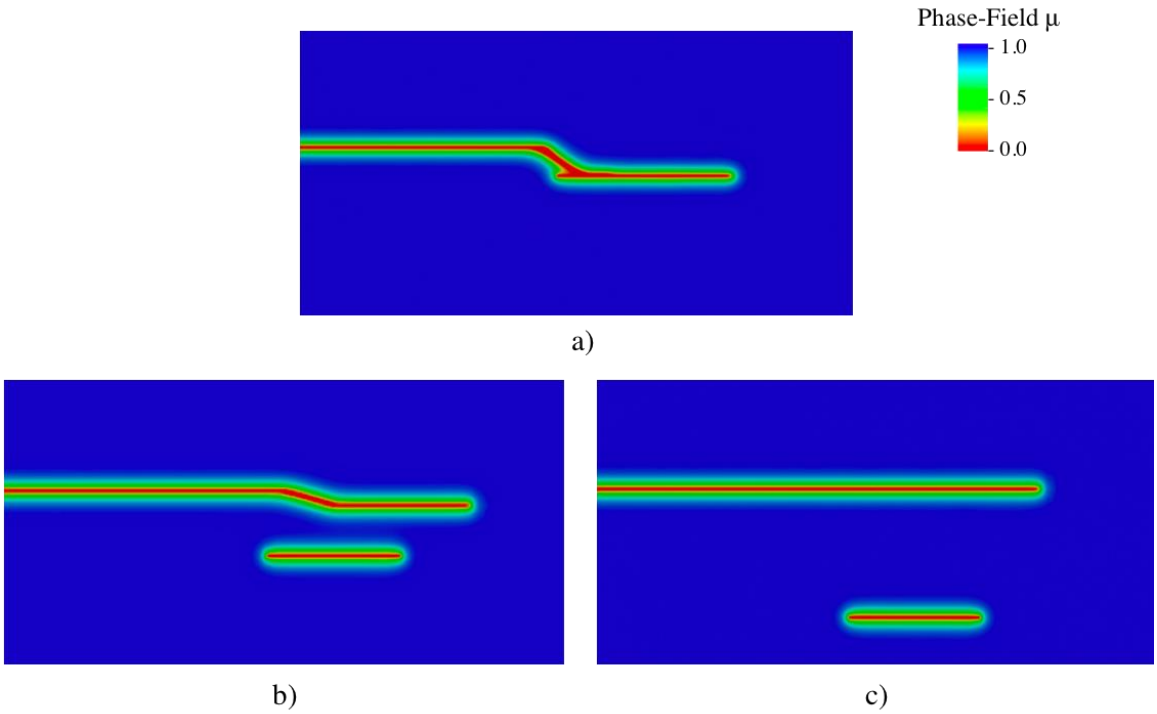

Figure 4.19: Three different vertical spacings are tested for the same opening of the propped fracture to d = 10, and $\delta/\varepsilon_0 l_0$ = 5.4: a) $y = 10l_0$, b) $y = 20l_0$ and c) $y = 40l_0$. The Poisson's ratio ν = 0.25, ε_0 = 0.001, $l_0^2/\kappa = 10^{14}$, α = 0.45, ϕ_0 = 0.1, c^f / ρ_0^f = 0.01364, and $\upsilon^f/E\varepsilon_0 t_0 = 5 \times 10^{-12}$. For variable d, please see equation (4.9).

Lastly, Figure 4.20 shows the pressure as a function of the volumetric fluid injection. Also, the figure shows the configuration of the fracture evolution in terms of the injection pressure and the injection flow. The pressure first increases until it completely fills the induced crack. Then, the pressure drops as the induced fracture propagates. Once the induced fracture encounters the propped crack, the pressure begins to increase until both cracks merge. Finally, the fluid begins to fill the propped crack, pressurize it and propagate it.

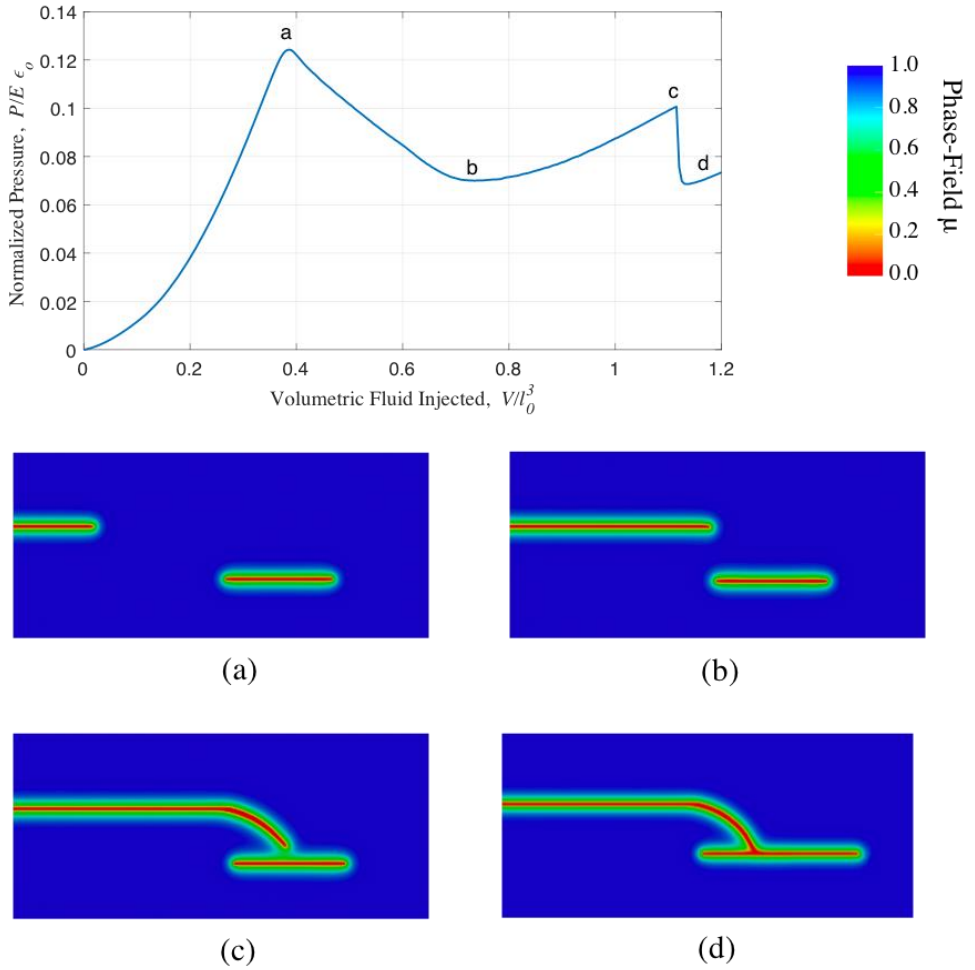

Figure 4.20: The fracture propagation trajectories: (a) the fracture state at load step V/l_0^3 = 0.38, (b) the fracture state at load step V/l_0^3 = 0.73, (c) the fracture state at load step V/l_0^3 = 1.1, and (d) the fracture state at load step V/l_0^3 = 1.2. The Poisson's ratio ν = 0.25, ε_0 = 0.001, $l_0^2/\kappa = 10^{14}$, α = 0.45, ϕ_0 = 0.1, c^f / ρ_0^f = 0.01364, and $\upsilon^f/E\varepsilon_0 t_0 = 5 \times 10^{-12}$.

In conclusion, these model simulations illustrate that propped cracks disturb the local stresses in their vicinity that disturb the path of the induced fractures passing by them. The propped fracture with a greater opening can disturb the propagation path of the induced fracture, slow it down, and attract them until they merge. Moreover, the induced fracture is attracted to the propped fracture when it is closest to the induced fracture plane. This illustrates a problem associated with the influence of old propped cracks on the re-fracturing treatment when a new drainage area is targeted.

4.4 Crack Growth Through Multiple Layers

Unconventional reservoirs are stratified with multiple layers of materials with contrasting properties [34-38], and induced hydraulic fractures are expected to propagate thought multiple layers [39, 40]. Here, the problem of how a fluid-driven crack behaves as it encounters a different layer is investigated and limited to a single layer placed at a particular distance away from the injection point. The following factors are investigated: (a) the thickness of the layer; (b) the orientation of the layer; (c) the contrast of material proprieties between the matrix and the layer; and (d) the viscosity of the injected fluid. Regarding the material contrast, only the contrast in the modulus of elasticity E and the critical energy release rate G_c between the matrix and the layer are allowed to differ. For the modulus of elasticity contrast:

$$R_E = \frac{E_L}{E_M} \tag{4.10}$$

Where R_E is the ratio between the modulus of elasticity of the layer E_L to the modulus of elasticity of the matrix E_M. Similarly, for the material toughness contrast:

$$R_{G_c} = \frac{G_{c,L}}{G_{c,M}} \tag{4.11}$$

Where R_{G_c} is the ratio between the critical energy release rate of the layer $G_{c,L}$ to the critical energy release rate of the matrix $G_{c,M}$. When R appears without subscripts, this means that $R = R_E = R_{G_c}$. Regarding a qualitative description of the layer stiffness and toughness, the layer can be in four states:

- $R_E > 1$ → The layer is '**stiffer**' than the matrix.

- $R_E < 1$ → The layer is '**softer**' than the matrix.
- $R_{G_c} > 1$ → The layer is '**tougher**' than the matrix.
- $R_{G_c} < 1$ → The layer is '**weaker**' than the matrix.

Throughout the simulations of these layer problems, the layer and the matrix are assumed to be fully bonded on their interfaces. A large rectangular domain with the dimensions of $1000l_0$ X $2000l_0$ is simulated. As shown in Figure 4.21, the center of the layer is placed at a distance *x* away from the injection point. The thickness of the layer is w. The surface normal displacements and surface normal fluid flux on the outer boundaries are set to zero. Throughout the layer simulations, the Biot coefficient α is 0.45, the initial porosity is ϕ_0= 0.1, the normalized permeability is $\bar{\kappa}$ =10^{-14}. A fluid is injected into the left edge of the crack at a constant rate.

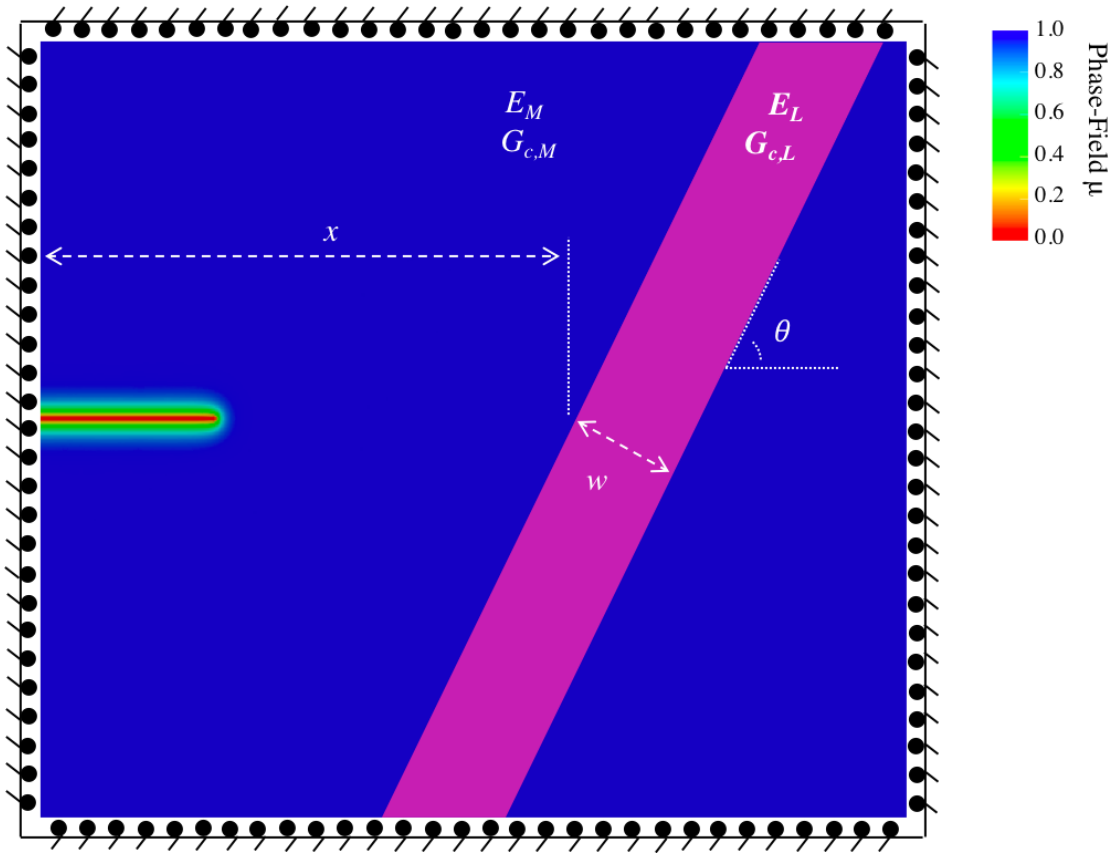

Figure 4.21: Schematic diagram of the layers problem. A rectangular domain of $1000l_0$ x $2000l_0$ with a left-center crack. A layer of thickness w is placed at distance x. θ is the angle of the orientation of the layer relative to the horizontal direction. Throughout the layer problems, the Poisson's ratio $\nu = 0.25$, $\varepsilon_0 = 0.001$, $l_0^2/\kappa = 10^{14}$, $\alpha = 0.45$, $\phi_0 = 0.1$, $c^f / \rho_0^f = 0.01364$.

4.4.1 DEMONSTRATION EXAMPLES OF THE LAYER INFLUENCE

First, examples of different cases are shown to demonstrate the effect of the following: (a) the layer orientation, (b) R_E, and R_{G_c} ratios of the layer stiffness and toughness relative to the matrix, (c) a comparison between the effect of the toughness of the layer R_{G_c} versus the effect of the stiffness of the layer R_E , and (d) a nearly rigid vertical layer. Thereafter, mappings of the layer orientation for different factors are presented. In this mapping, critical material contrast ratios are reported that separate two behaviors: 1) interface crossing and 2) crack deflection. In addition to the orientation mappings, the influence of the distance between the layer and the injecting point on the fracture evolution is studied.

Layer Orientation Effect

Here, the same contrast ratio *R* for both the stiffness and the toughness is used. The layer with a thickness of $15l_0$ is placed $100l_0$ away from the injection point. For the material contrast, *R*=1.5 for the stiff-tough layer and *R*=1/1.5 for the weak-soft layer. Two layer orientations studied, 33^0 and 78^0. This results in four cases to study, as shown in Figure 4.22 (a), (b), (c) and (d):

- Case (a): *R* =1.5, $\theta = 33^0$
- Case (b): *R* =1.5, $\theta = 78^0$
- Case (c): *R* =1/1.5, $\theta = 33^0$
- Case (d): *R* =1/1.5, $\theta = 78^0$

For the stiff-tough layer in Figure 4.22 (a), the induced fracture prefers to deflect in the matrix and propagate along the interface when the angle is low. b) When the layer in (a) is reoriented to 78^0, the layer is not able to deflect the crack. For the weak-soft layer as in (c), the induced fracture prefers to enter the layer zone and propagate through the layer when the angle is low. When the layer in (c) is reoriented to 78^0, the layer is unable to contain the crack, as shown in Figure 4.22 (d). These cases suggest that the layer orientation angle controls the fracture behavior.

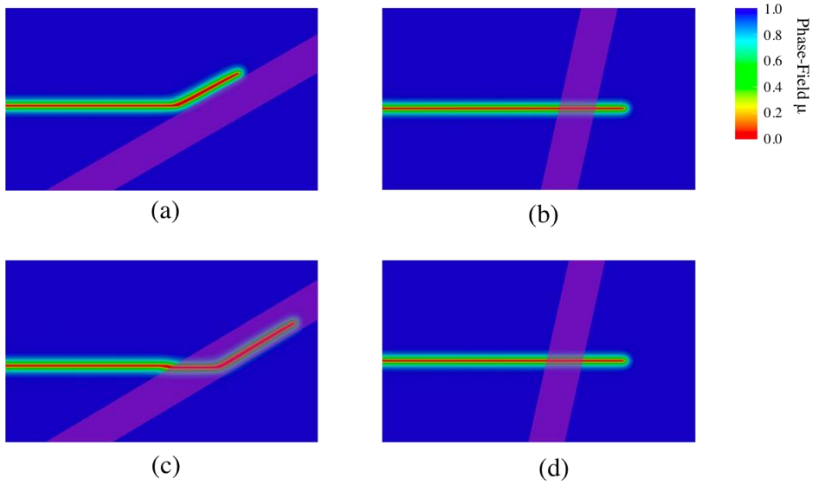

Figure 4.22: A demonstration of the effect of the layer orientation on the behavior of the fracture. The thickness of the layer is $15l_0$: (a) a tough-stiff layer with ratio R = 1.5 for both E and G_c at $\theta = 33^0$ (b) a tough-stiff layer with ratio R = 1.5 for both E and G_c at $\theta = 78^0$; (c) a weak-soft layer with ratio R = 1/1.5 for both E and G_c at $\theta = 33^0$; and (d) a weak-soft layer with ratio R = 1/1.5 for both E and G_c at $\theta = 78^0$. The fluid viscosity, $\upsilon^f/E\varepsilon_0 t_0 = 5 \times 10^{-12}$.

Modulus of Elasticity and Critical Energy Release Rate Contrast Ratios

Here again, four cases are studied, with the orientation of the layer is held to be 78^0. The layer has a thickness of $15l_0$ and placed $100l_0$ away from the injection point. The four cases are:

- Case (a): *R* =3.
- Case (b): *R* =3/2.
- Case (c): *R* =2/3.
- Case (d): *R* =1/3.

For the case shown in Figure 4.23 (a), the layer is tougher and stiffer than the matrix with *R* =3. The fracture is deflected away from the layer preferring to propagate along the layer interface, and a secondary fracture is observed. (b) As the material contrast ratio *R* is decreased to 3/2, the fracture crosses through the layer. (c) Then the ratio *R* is lowered again to 2/3, making the layer weaker and softer than the matrix, and yet the crack crosses the layer. (d) When the layer is weakened and softened again to ratio *R* equal to 1/3, the crack prefers to propagate within the layer, and a secondary crack branch observed as seen in the case (a). These cases show that the ratio *R* has a significant influence on the propagation of the fracture. Layers that are very stiff and tough or very soft and weak are more likely to deflect the crack from its initial orientation.

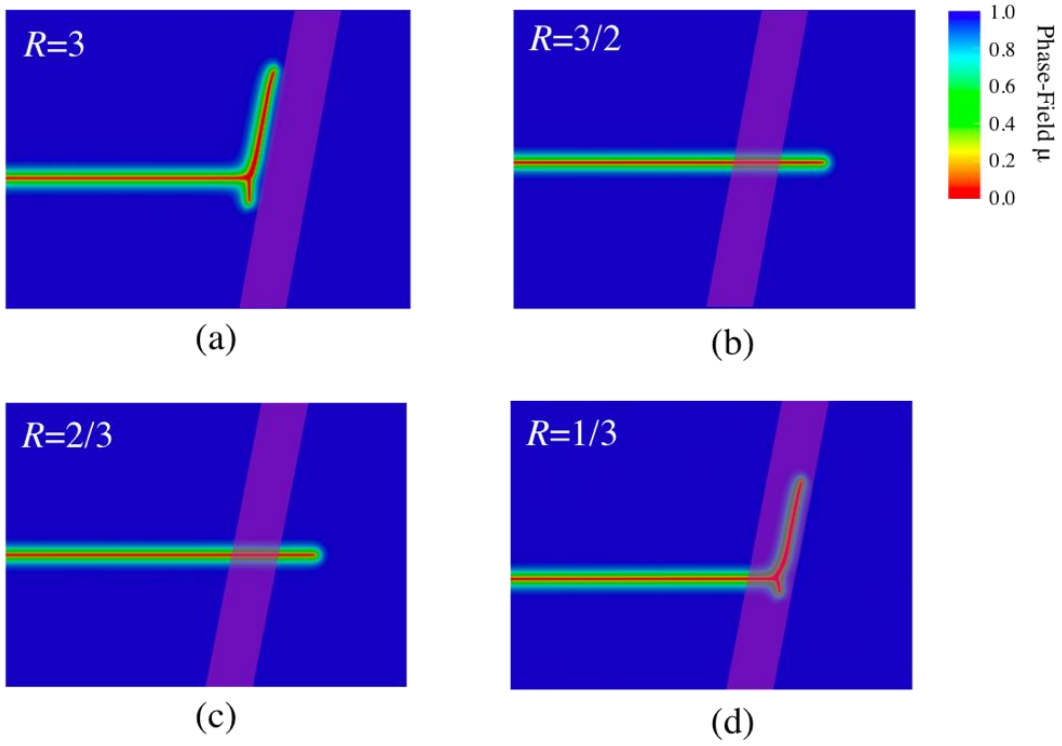

Figure 4.23: A demonstration of the effect of the R ratio of the E and G_c of the layer relative to the matrix on the induced fracture behavior at a fixed $\theta = 78^0$. The thickness of the layer is $15l_0$. (a) A tough-stiff layer with ratio $R = 3$. (b) A tough-stiff layer with ratio $R = 3/2$. (c) A weak-soft layer with ratio $R = 2/3$. (d) A weak-soft layer with ratio $R = 1/3$. The fluid viscosity, $\upsilon^f/E\varepsilon_0 t_0 = 5 \; x \; 10^{-12}$.

The Effect of Stiffness Versus Toughness Contrasts

Two cases are studied to see which has more influence, the modulus of elasticity contrast or the critical energy release rate contrast, on the crack propagation path. For both cases, the angle of the layer orientation is fixed at 45^0. The two cases are:

- Case (a): $R_{G_c} = 2, R_E = 1$, (the layer is only tougher than the matrix).
- Case (b): $R_{G_c} = 1, R_E = 2$, (the layer is only stiffer than the matrix).

As seen in Figure 4.24 (a) when the layer is only tougher than the matrix ($R_{G_c} = 2$), the crack is deflected in the matrix along the layer interface. However as in (b), when the layer is only stiffer than the matrix ($R_E = 2$) , the crack crosses the layer. These simulations show that the toughness contrast has a greater influence than the stiffness contrast on the fracture growth.

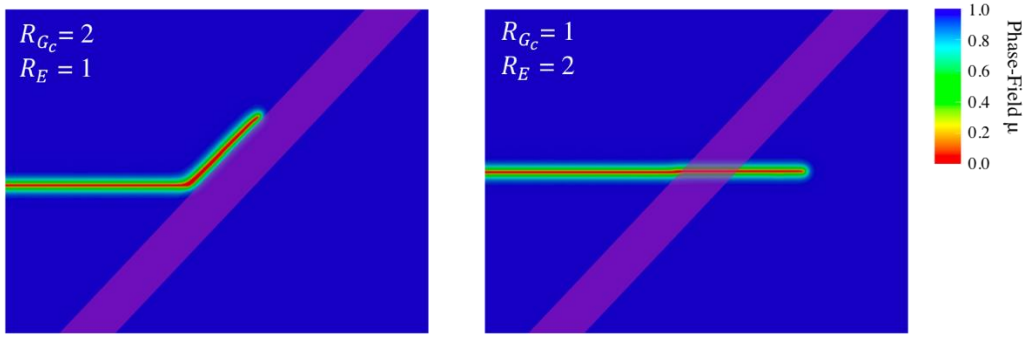

Figure 4.24: A demonstration of the effect of the toughness and stiffness contrast on the induced fracture behavior at a fixed interface angle of $\theta = 45^0$. The thickness of the layer is $15l_0$. a) $R_{Gc} = 2$, $R_E = 1$, b) $R_{Gc} = 1$, $R_E = 2$. The fluid viscosity, $\upsilon^f/E\varepsilon_0 t_0 = 5 \times 10^{-12}$.

Nearly-Rigid Vertical Layer

A layer with very high toughness and stiffness relative to the matrix should act as a rigid barrier against the propagation of the fracture. Figure 4.25 shows a fluid-driven crack encountering an extremely tough and stiff vertical layer with ratio R equal to 100 for both the critical energy release rate contrast and the modulus of elasticity contrast. As is expected, the induced fracture branches into two fractures in a symmetric manner and propagates within the matrix material along the layer interface.

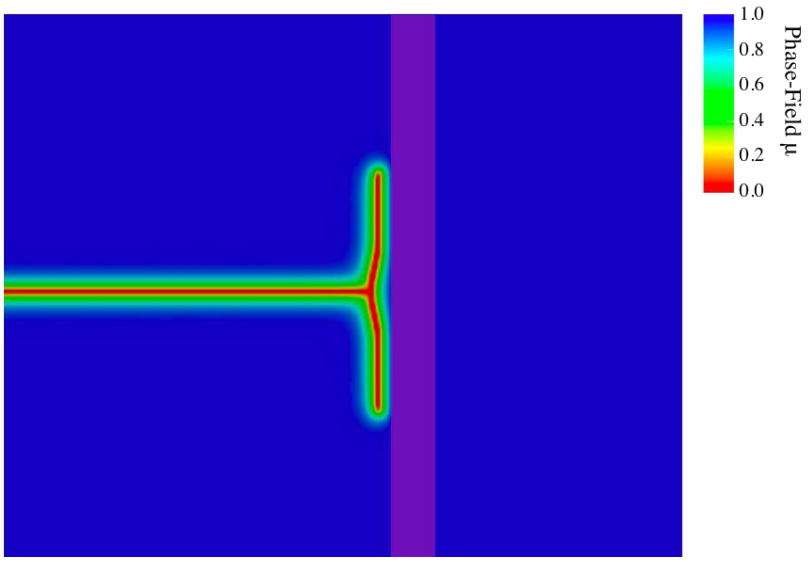

Figure 4.25: A demonstration of the effect of a very tough and stiff vertical layer on the induced fracture behavior. The thickness of the layer is $15l_0$. The fracture branches symmetrically once it encounters the stiff layer. The fluid viscosity, $\upsilon^f/E\varepsilon_0 t_0 = 5 \; x \; 10^{-12}$.

4.4.2 MECHANISM MAPS

In this section, detailed calculations have been carried out to quantify the effect of four factors: 1) layer thickness, 2) stiffness and toughness contrasts, 3) the distance between the layer and the injection point, and 4) the viscosity of the injected fluid. The goal here is to find the critical values of the material property contrast ratios that separate the three crack propagation modes: 1) deflecting in the matrix along the layer, 2) crossing the layer, and 3) deflecting within the layer as demonstrated in Figure 4.26.

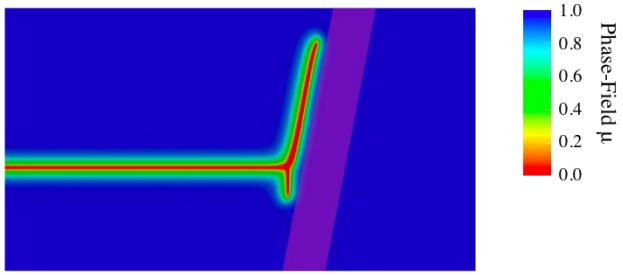

a) Deflecting in the matrix along the layer

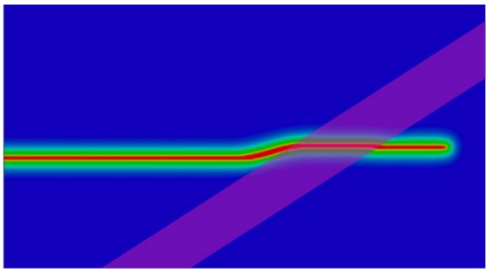

b) Crossing the layer

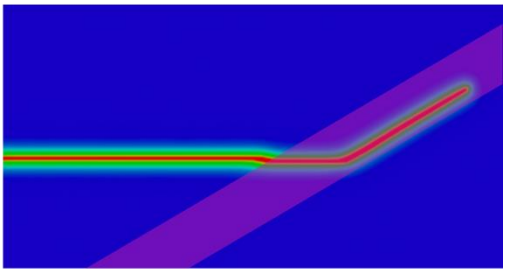

b) Deflecting within the layer

Figure 4.26: Three modes have been observed throughout the layer problems: a) the induced fracture is deflected in the matrix along the layer, b) the induced fracture crosses the layer, and c) the induced fracture deflects within the layer.

Layer Hardness

A layer with a finite thickness of $15l_0$ is held $200l_0$ away from the injection point, and the ratios of R_E and R_{G_c} are equal and vary together. As seen in Figure 4.27, a layer with a shallow angle is more likely to deflect the induced fracture than a layer with a steep angle. The critical contrast ratio that separates the crossing and the deflection modes nearly doubles from an angle of 22^0 to an angle of 78^0. This suggests that the propagation mechanism depends strongly on the layer orientation.

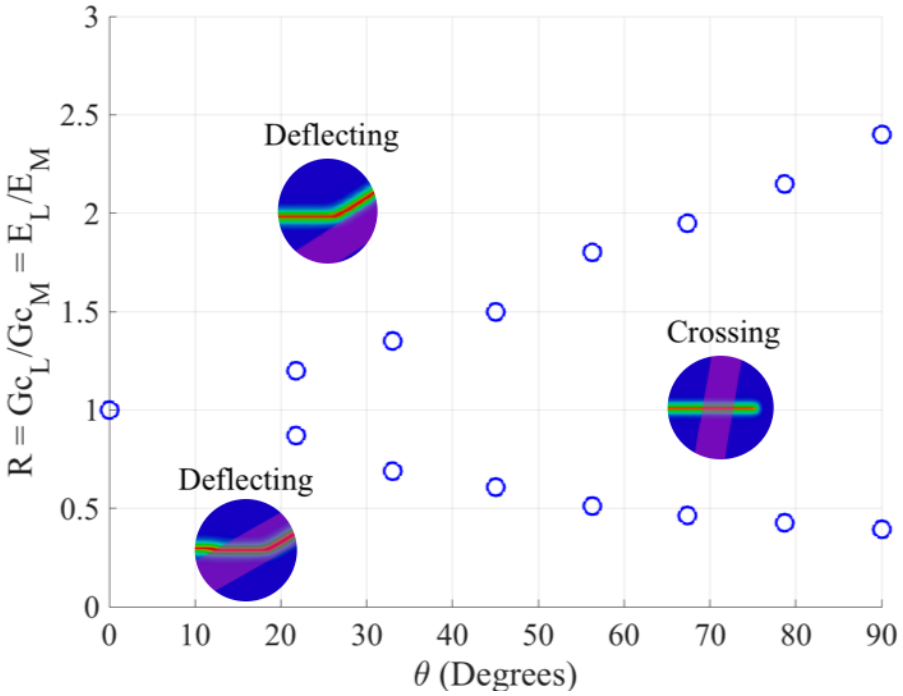

Figure 4.27: The mapping of critical values that separate two fracture behaviors: crossing and deflecting. The layer thickness is held fixed at $15l_0$. The fluid viscosity, $\upsilon^f/E\varepsilon_0 t_0 = 5 \; x \; 10^{-12}$.

Layer Thickness

Two thicknesses are chosen: a finite one of $15l_0$ (Figure 4.28 (a)) and a semi-infinite thickness (Figure 4.28 (b)), where the domain is split into two sub-domains. Figure 4.28 (c) shows the dependence of the propagation mechanism on the materials contrast as a function of the interface angle for these two layer thicknesses. Notice that the fracture is more likely to cross a thinner layer than a thicker layer for all interface angle and contrast ratios. This shows the sensitivity of the propagation behavior to the layer thickness.

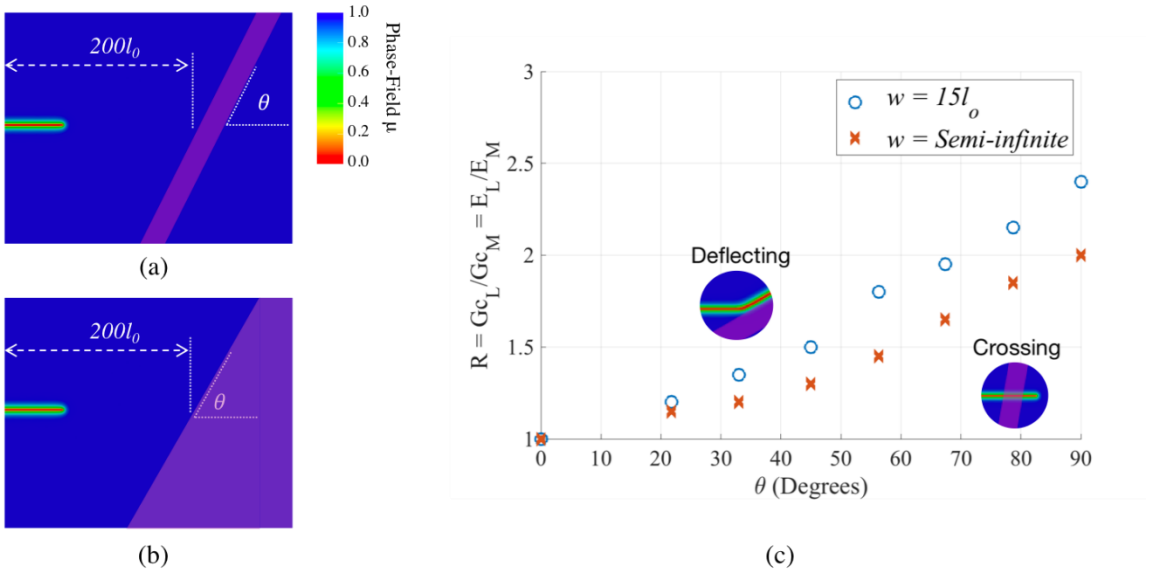

Figure 4.28: The mapping of critical values that separate two fracture behaviors: crossing and deflecting. Two thicknesses are considered: a) a finite thickness of $15l_0$ and b) a semi-infinite thickness. The fluid viscosity, $\upsilon^f/E\varepsilon_0 t_0 = 5 \times 10^{-12}$.

Material Contrast Ratios

In this section, three different material contrasts are studied:

- Case (a): The layer is tougher and stiffer than the matrix ($R > 1$).
- Case (b): The layer is tougher than the matrix, and both the layer and the matrix have the same stiffness ($R_{G_c} > 1$, R_E=1).
- Case (c): The layer is stiffer than the matrix, and both the layer and the matrix have the same toughness ($R_E > 1$, R_{G_c}=1).

As shown in Figure 4.29, the fracture behavior in case (a) and case (b) shows a strong dependence on the layer orientation, as discussed previously. The fracture is more likely to cross a layer with a low orientation angle as well as a layer with low toughness and stiffness contest ratios. Additionally, the difference between case (a) and case (b) regarding contrast ratios R versus R_{G_c} as a function on the orientation angle is observed. The fracture is more likely to cross a layer with only toughness contrast ratio and to be deflected by a layer that is both tougher and stiffer than the matrix. In this situation, the stiffness contrast increases the layer tendency to deflect the fracture. However, as in case (c), when the layer is only stiffer than the matrix, and both the layer and the matrix have the same toughness, the layer cannot act as a barrier, and the fracture crosses through for all orientations. In summary:

- A layer with the modulus of elasticity contrast ratio only cannot act as a barrier. This is consistent with studies by Daneshy [42] who performed experiments showing that the contrast in modulus of elasticity across layers is not sufficient to prevent a fracture from growing into the stiff layer.
- Among the material properties contrasts, the toughness of the layer is the dominant factor in controlling the fracture behavior.
- Cases (a) and (b) show that the modulus of elasticity contrast ratio has a secondary effect compares to the toughness effect. However, when the layer and the matrix have the same toughness, stiffness contrast alone does not appear to affect the fracture behavior.

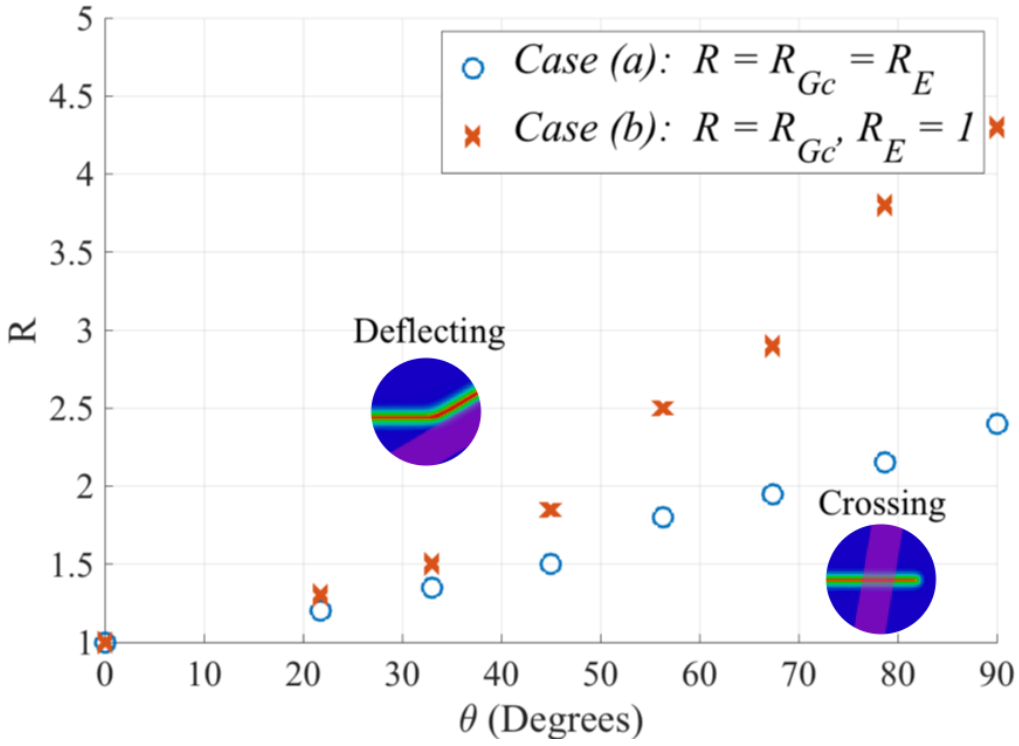

Figure 4.29: The mapping of the regimes for layer: crossing versus crack deflection. Two scenarios are considered: a) varying R_{Gc} ratio with R_E =1 and b) varying both ratios $R = R_{Gc} = R_E$. The fluid viscosity is $\upsilon^f/E\varepsilon_0 t_0 = 5 \times 10^{-12}$.

Injected Fluid Viscosity

In this section, the effect of the injected fluid viscosity is studied. Regarding the effects of the fluid viscosity versus the material toughness on fluid-driven crack behavior, Detournay et al. [54-56] provided insights based on a dimensionless parameter $\mathcal{K}$ that compares the material fracture toughness K_{IC} to the fluid viscosity v^f. Recall that:

$$\mathcal{K} = 4K_{IC}/\sqrt[4]{3\pi^3 E'^3 Q v^f} \quad (4.12)$$

Where Q is the volumetric injection rate. Two regimes are investigated; 1) the toughness-dominated regime, where the energy dissipated at the crack tip to propagate the fracture is large compared to the energy dissipated due to the flow of the viscous fluid, and 2) the viscosity-dominated regime, where the energy dissipated due the viscous fluid is very large compared to the dissipation due to fracture propagation. Here, two fluid viscosities are investigated:

- Case (a): $v^f/E\varepsilon_0 t_0 = 5 \times 10^{-12}, \mathcal{K} = 19.42$.
- Case (b): $v^f/E\varepsilon_0 t_0 = 10^{-9}, \mathcal{K} = 2.9$.

Detournay [54-56] concluded that when $\mathcal{K} < 1$, the solution can be approximated on the assumption that the material has zero toughness (viscous-dominant regime), and when $\mathcal{K} > 4$, the solution can be approximated on the assumption that the injected fluid is inviscid (toughness-dominant regime). Based on $\mathcal{K}$ calculations, case (a) resides in the toughness-dominant regime while case (b) is in a transition regime that is between the toughness-dominant and the viscous-dominant regimes. The relative difference in these fluid viscosities that are chosen is similar to the difference between slickwater and glycerin fluid. For both cases, the distance between the layer and the injection point is fixed at $200l_0$ and the layer thickness is $15l_0$. As seen in Figure 4.30, the crack is more likely to cross the layer when a very viscous injection fluid is used. However, the dependence of the mechanism on the viscosity appears to be weak.

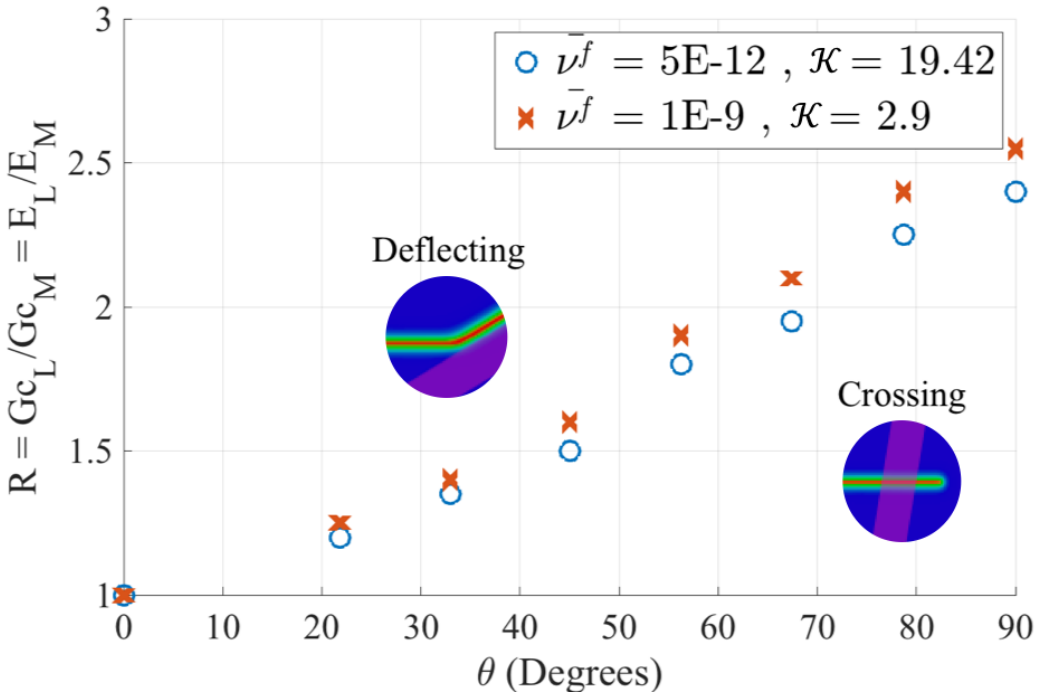

Figure 4.30: The mapping of critical values that separate layer crossing versus crack deflection. Two injected fluid viscosities are considered: a) $\upsilon^f/E\varepsilon_0 t_0$ = 5E10^{-12} , $\mathcal{K}$ = 19.42 , b) $\upsilon^f/E\varepsilon_0 t_0$ =10^{-9}, $\mathcal{K}$ = 2.9.

Distance Between the Injection Point and the Layer

The influence of the distance between the injection point and the layer on the fracture behavior is investigated. The layer orientation is fixed at 67^0 and the distance is varied. As seen in Figure 4.31 and for two values of the injected fluid viscosity, it appears that the distance between the injection point and the layer does not significantly influence the fracture behavior. In addition, it appears that viscous fluids tend to drive the fracture

through layers more readily than low viscous fluid. However, as for the cases studied in Figure 4.31, the dependence of the mechanism on the viscosity is mild.

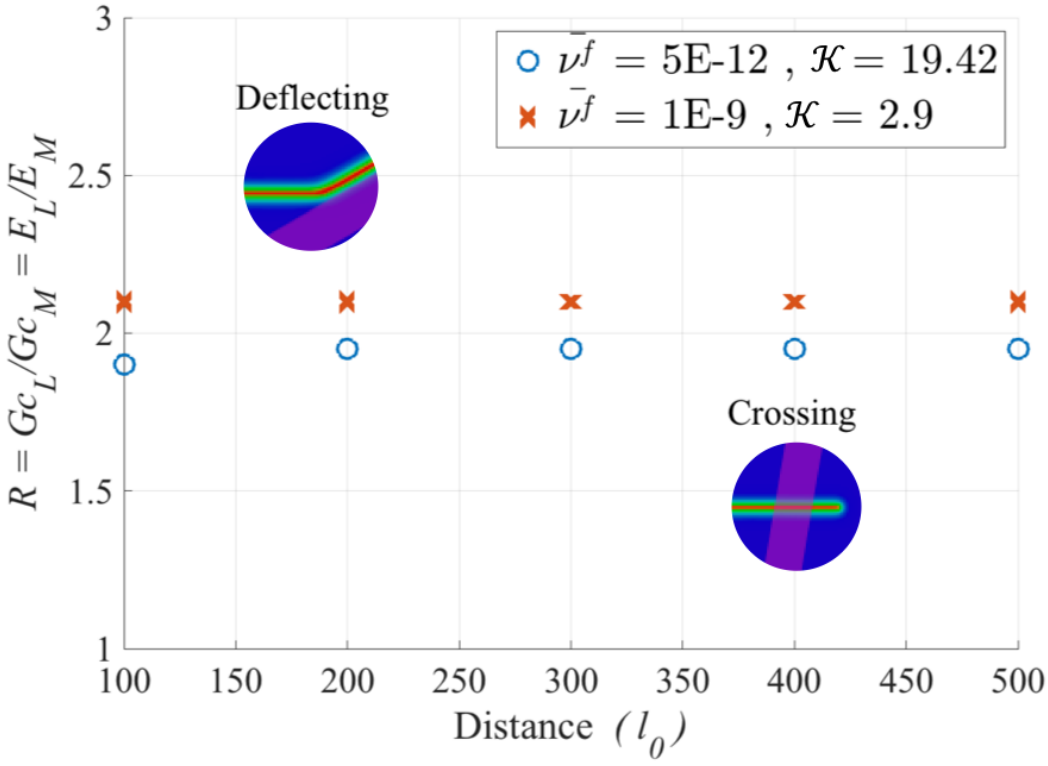

Figure 4.31: Dependence of the fracture mechanism on the injection point distance. Two injected fluid's viscosities are considered: a) $\upsilon^f/E\varepsilon_0 t_0$ = 5E10^{-12} , $\mathcal{K}$ = 19.42 , b) $\upsilon^f/E\varepsilon_0 t_0$ =10^{-9}, $\mathcal{K}$ = 2.9.

In conclusion, several factors influence the fracture behavior when a fluid-driven fracture encounters a layer. A comprehensive study of all the dependencies is beyond the scope of this dissertation. However, some factors have been investigated. A stiff and tough layer tends to deflect the fracture. However, modulus of elasticity contrast alone is not

sufficient to make the layer act as a barrier if the toughness of the layer is low. Furthermore, a layer at a steep inclination relative to the crack direction always has less ability to deflect the fracture than a layer with a shallow inclination. This demonstrates the sensitivity of the propagation behavior to the layer orientation. Additionally, a thicker layer has a greater tendency to deflect the crack than a thinner layer. The distance between the injection point and layer does not appear to have a significant impact on the fracture behavior. Finally, the fracture behavior is weakly dependent on the fluid viscosity.

4.5 Crack Growth Under the Influence of In-Situ Stresses

The in-situ stress magnitudes and orientations are considered to be the dominant factor in fracture treatment design [20, 29]. The contrast ratio of the in-situ stresses has a significant impact on the fracture propagation orientation [30]. Moreover, an induced fracture tends to orient itself to be perpendicular to the minimum principal in-situ stress [31-33]. Here, the problem of an induced fracture subjected to far-field stress is studied (see Figure 4.32 (a)). The goal is to show how the induced fracture at an oblique angle behaves under the influence of the far-field stresses. In addition, the kink angle of the crack defined in Figure 4.32b has been investigated for different induced fracture orientations as well as for different far-field stress magnitudes. Lastly, additional simulations are shown where multiple factors compete together in controlling the crack growth.

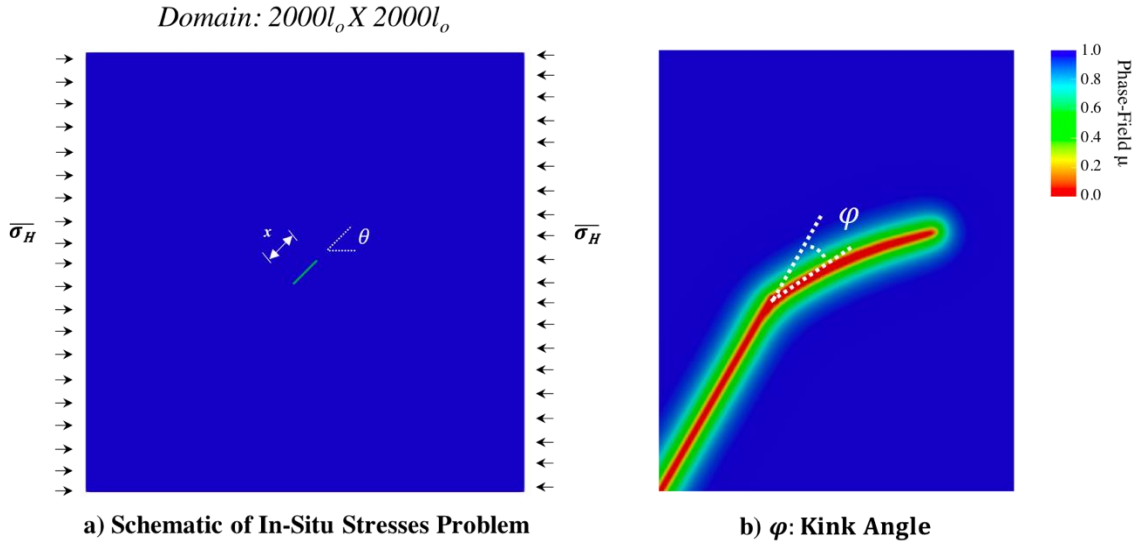

Figure 4.32: a) Schematic of a square domain of $2000l_0$ *x* $2000l_0$ with a central crack with length of $150l_0$ oriented at angle θ. Horizontal far-field stresses σ_H are applied to both left and right sides, and both top and bottom surfaces are traction free. b) The kink angle φ of the induced fracture. Throughout the in-situ stress problems, the Poisson's ratio $\nu = 0.25$, $\varepsilon_0 = 0.001$, $l_0^2/\kappa = 10^{12}$, $\alpha = 0.45$, $\phi_0 = 0.1$, $c^f / \rho_0^f = 0.01364$, and $\upsilon^f/E\varepsilon_0 t_0 = 10^{-11}$.

Here, a large square domain with the dimensions of $2000l_0$ X $2000l_0$ is simulated (see Figure 4.32(a)), where a crack $150l_0$ long is placed at the center of the domain and oriented with angle θ. A horizontal far-field stress $\overline{\sigma_H}$ is applied on right and left boundaries. Top and bottom surfaces are traction free. The surface normal fluid flux on the outer boundaries is set to zero (see Figure 4.7). The Biot coefficient α is 0.45, the initial porosity is $\phi_0 = 0.2$, and the normalized permeability is $\bar{\kappa} = 10^{-12}$. A fluid is injected at the center of the crack at a constant rate $\bar{Q} = 0.005$.

As seen in Figure 4.33, an induced fracture $150l_0$ long is initially oriented at 45^0 relative to the direction of the maximum far-field stress ($\overline{\sigma_H} = 0.1$). As expected, the fracture reorients itself to be perpendicular to the minimum in-situ stress. This shows that the far-field stress forces the fracture to reorient itself during the propagation to be aligned with the maximum principal stress direction. This behavior of the fracture turning towards the maximum principal stress direction is in agreement with what has been discussed in the literature previously.

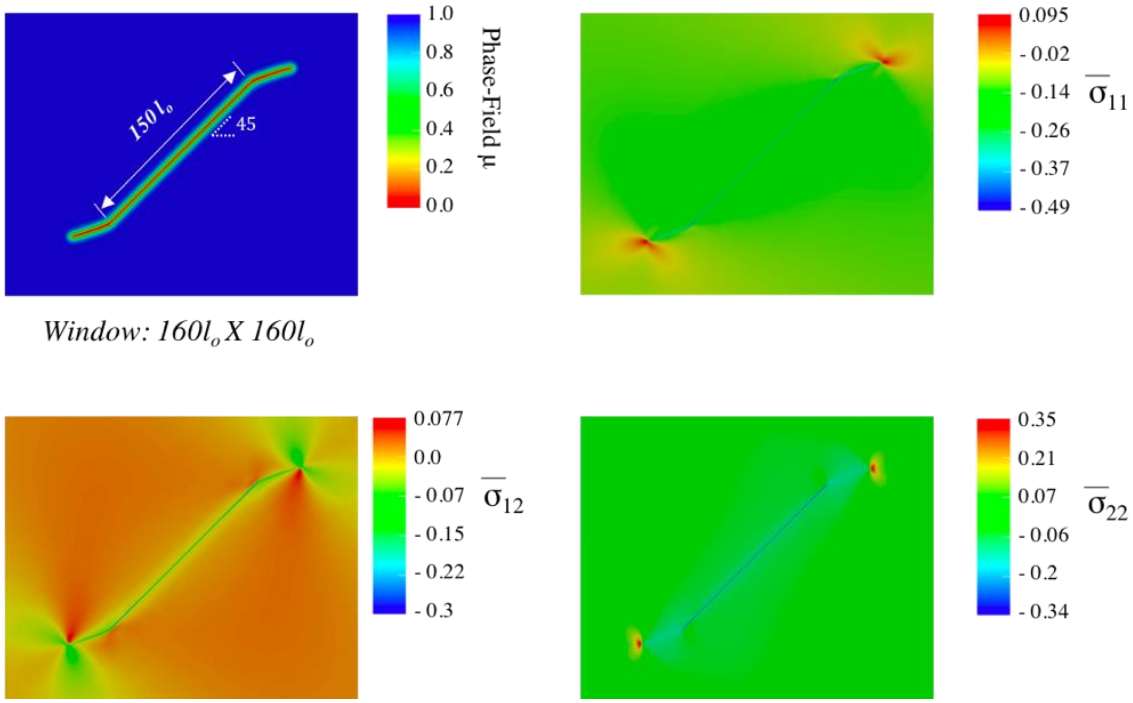

Figure 4.33: The evolution of a crack that is initially $150l_0$ long and oriented at 45^0 relative to the maximum far-field stress direction. The stress field for the trajectory of the crack growth is shown for load step $V/l_0^3 = 0.38$. The horizontal far-field stress is $\sigma_H/E\varepsilon_0 = 0.1$.

Next, the fracture kink angle is studied for different initial crack orientations and different in-situ stress magnitudes. The kink angle φ is the angle between the initial orientation of the fracture and the extension of the propagated fracture, as demonstrated in Figure 4.32 (b). This angle can depend on many factors; the initial fracture length, the in-situ stresses, and initial fracture orientation, etc. Here, the influence of the in-situ stresses and the initial fracture orientation on the kink angle are investigated. Figure 4.34 (a) shows the kink angle φ for different in-situ stress. The kink angle increases as the in-situ maximum stress increases. In Figure 4.34 (b), the kink angle also increases as the initial orientation of the crack deviates from the maximum in-situ stress direction. This emphasizes the strong influence of the in-situ stresses on the fracture growth, as discussed previously.

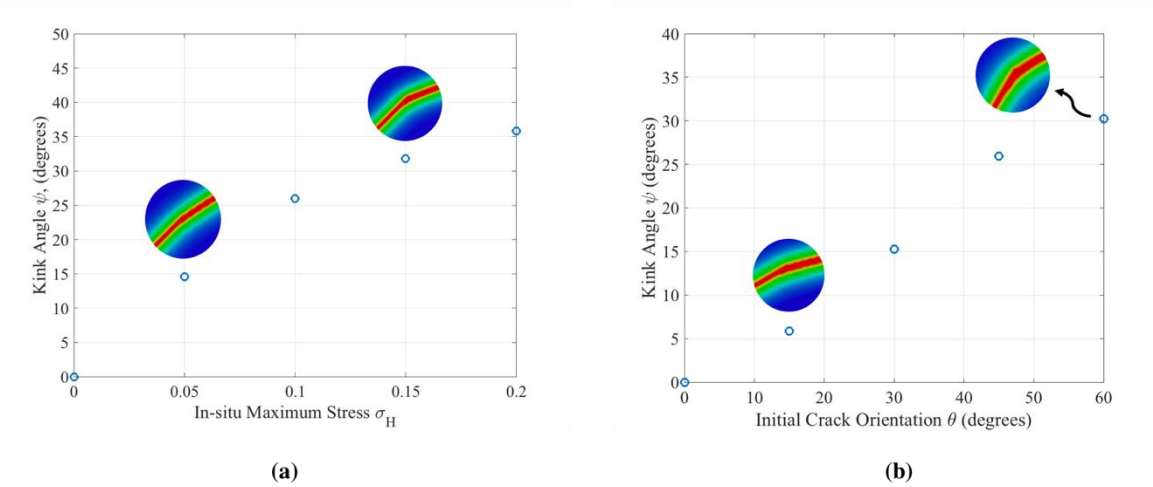

Figure 4.34: a) The kink angle φ of a fluid-driven fracture for different initial orientations. The horizontal in-situ stress is $\sigma_H/\varepsilon_0 l_0 = 0.1$, b) The kink angle φ of a fracture for different initial crack orientation.

In summary, the phase-field approach was applied to show the influence of the in-situ stresses on the fracture evolution. As expected, the fracture should be aligned with the maximum in-situ stress direction as opposed to the minimum in-situ stress direction. If the initial orientation is not the direction perpendicular to the minimum stress direction, the crack reorients itself during the growth to become perpendicular to the minimum in-situ stress direction. The kink angle increases as the fracture orientation angle increases as well as the far-field stress increases. All the simulations in this section suggested that the fracture growth is strongly dependent on the far-field stresses applied.

DEMONSTRATION EXAMPLES OF THE FAR-FIELD STRESS EFFECT

In the following section, three previous problems will be revisited:

- Two parallel fluid-driven cracks as in section 4.2 but will be subjected to far-field stress.
- A domain with crack filled with proppant as in section 4.3 but will be subjected to far-field stress.
- A domain with a single layer as in section 4.4 but will be subjected to far-field stress.

The goals of these simulations are 1) to provide examples that illustrate how far-field stress can change the fracture behavior in more complex topologies, and 2) to demonstrate the capabilities of the phase-field approach to tackling such complicated problems.

In section 4.2, the behavior of two parallel fluid-driven fractures was shown in Figure 4.8 (a). The parallel induced fractures deflect away from each other due to the stress shadow effect. However, the far-field stresses tend to drive the fracture towards the direction perpendicular to the minimum principal stress direction. In this section, the parallel fluid-driven fractures will be investigated again, where the domain will be subjected to far-field stress. The normalized horizontal far-field stress $\overline{\sigma_H}$ = 0.1 is applied to both left and right sides as shown in Figure 4.35 (a). Top and bottom boundaries are traction free. In the absence of far-field stresses, the induced fractures deflect away from each other as shown in Figure 4.35 (b). However, when a far-field stress is applied, the

tendency to grow parallel to the maximum in-situ stress can overwhelm the stress shadow effect and forces the fractures to propagate in a straight direction.

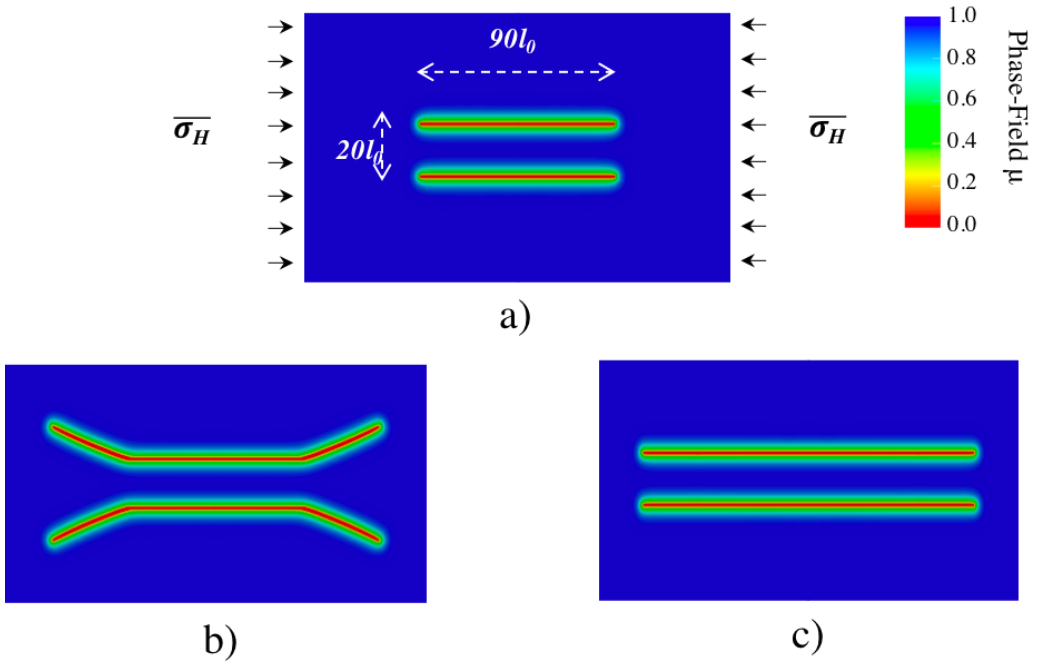

Figure 4.35: (a) Schematic of parallel fractures. (b) The fracture evolution in the absence of in-situ stresses. (c) The fracture evolution under the influence of the in-situ stresses $\sigma_H/\varepsilon_0 l_0 = 0.1$. The Poisson's ratio $\nu = 0.25$, $\varepsilon_0 = 0.001$, $l_0^2/\kappa = 10^{12}$, $\alpha = 0.45$, $\phi_0 = 0.1$, $c^f / \rho_0^f = 0.01364$, and $\upsilon^f/E\varepsilon_0 t_0 = 5 \times 10^{-12}$.

Another demonstration example of the effect of the far-field stress will be shown by revisiting the problem of a fracture filled with proppants studied in section (4.3) where the domain is subjected to far-field stresses. Recall that the crack filled with proppants can disturb the new induced fracture growth path. It has been seen that the new induced fracture would be attracted to fractures filled with proppants depending on the opening

of crack filled with proppants as well as their separation distance. As seen in Figure 4.36 (b), a case where the fracture was slightly disturbed by the opening of the fracture is chosen. However, when the domain of the problem is subjected to a normalized horizontal far-field stress $\overline{\sigma_H}$ = 0.1 as in (c), the far-field stress overcomes the effect of the propped fractures and maintains the fracture path in a straight direction.

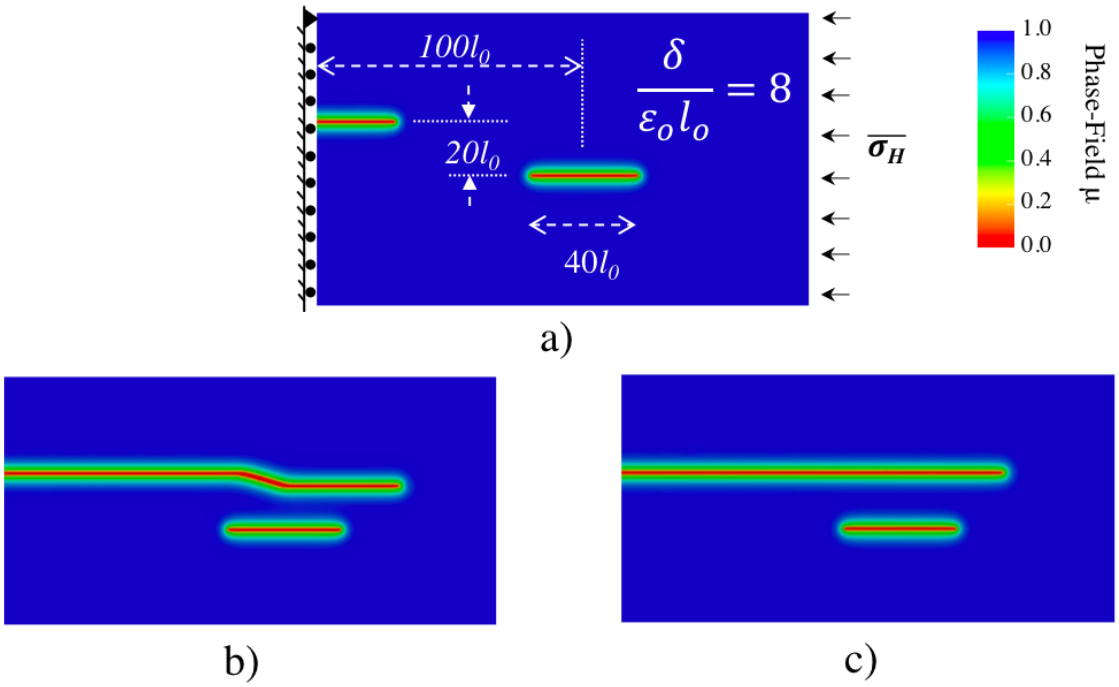

Figure 4.36: (a) Schematic of the propped fracture and induced fracture. (b) The fracture evolution in the absence of in-situ stresses. (c) The fracture evolution under the influence of in-situ stresses $\sigma_H/\varepsilon_0 l_0$ = 0.1. The Poisson's ratio ν = 0.25, ε_0 = 0.001, $l_0^2/\kappa = 10^{12}$, α = 0.45, ϕ_0 = 0.1, c^f / ρ_0^f = 0.01364, and $\upsilon^f/E\varepsilon_0 t_0 = 5 \times 10^{-12}$.

The last example here will show the competition between the effect of the presence of a tough layer and the effect of far-field stress (Figure 4.37 (a)) on the fracture growth. Previously, it has been shown, as in section 4.4, that the tough layer tends to deflect the fracture into the matrix along the layer interface. However, the far-field stress will always drive the fracture during growth to propagate in the direction perpendicular to the minimum in-situ principal stress. As seen in Figure 4.37 (b), in the absence of in-situ stresses, the fracture deflected in the matrix and propagated along the layer interface. However, in the presence of far-field stress subjected horizontally as in Figure 4.37 (c), the fracture deflected by the layer, and then the far-field stress overcomes the layer effect and forces the fracture to cross the layer interface. All these simulations show that the far-field stress can cause crack behavior to change. They emphasized the sensitivity of the fracture growth towards the in-situ stresses. They also demonstrated the capabilities of the phase-field approach to tackle complicated problems.

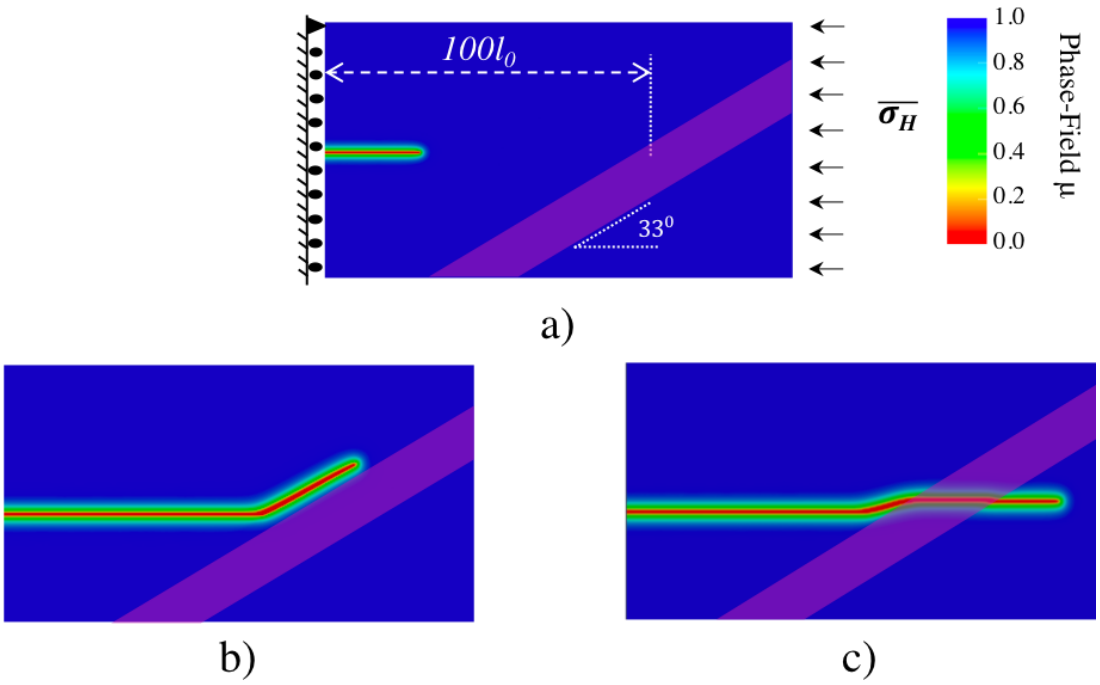

Figure 4.37: (a) Schematic of the layer problem. (b) The fracture evolution in the absence of in-situ stresses. (c) The fracture evolution under the influence of in-situ stresses $\sigma_H/\varepsilon_0 l_0 = 0.15$. The Poisson's ratio $\nu = 0.25$, $\varepsilon_0 = 0.001$, $l_0^2/\kappa = 10^{12}$, $\alpha = 0.45$, $\phi_0 = 0.1$, $c^f / \rho_0^f = 0.01364$, and $\upsilon^f/E\varepsilon_0 t_0 = 5 \times 10^{-12}$.

4.6 Inclusion Problems

In this section, the phase-field approach is used to simulate a set of inclusion problems and compared them to experimental observations. Many studies in the literature consider natural fractures to be closed and have frictional faces [20, 21]. However, natural fractures can also have a finite width and be cemented with different materials [13, 14]. Experiments were recently conducted to investigate how hydraulic fractures interact with cemented natural fractures [44, 45]. Cemented natural fractures can have higher or lower moduli of elasticity and fracture toughness, and the resulting crack growth behavior will depend on these properties. To understand how induced fractures interact with cemented natural fractures or what we are calling "inclusions'', sets of experiments have been conducted by Altammar [4]. Here, those experiments are simulated using the phase-field approach.

In Chapter 3, the setup of the inclusion experiments carried out by Altammar [4] was presented. Three different materials were used in the experiments: plaster was chosen for the matrix, hydrostone was chosen for a tough-stiff inclusion, and a mixture of 80% plaster with 20% talc was constructed to represent a weak-soft inclusion. The tough-stiff inclusion has higher material contrast ratios relative to the matrix: $R_E = 3.4$ for the modulus of elasticity contrast ratio and $R_{G_c} = 1.63$ for the critical energy release rate contrast ratio. For a weak-soft inclusion, the ratio for the modulus of elasticity relative to the matrix is $R_E = 0.51$ and the ratio for the critical energy release rate contrast is $R_{Gc} = 0.82$ (see Table 4-1).

Table 4-1: Normalized material properties for three materials; plaster, hydrostone, and a combination 80% plaster-20% talc for matrix, tough-stiff, and weak-soft inclusions, respectively.

Mixture	**Used as**	$\bar{E}$	$\overline{G_c}$	**Porosity,** ϕ (%)	**Permeability,** $\bar{k}$ **(10^{-6})**
Hydrostone	**Tough-stiff Inclusion**	**3.4**	**1.63**	**28.38**	**1.87**
Plaster	**Matrix**	**1**	**1**	**53.76**	**4.67**
80% Plaster-20% Talc	**Weak-soft Inclusion**	**0.51**	**0.82**	**59.73**	**5.15**

To simulate the experiments, a domain of $1000l_0$ X $1219.2l_0$ is used to simulate only half of the specimen that has the inclusion (see Figure 4.38). The Poisson's ratio is 0.25, the process zone length l_0 is chosen to be 125 μm, and the characteristic strain $\varepsilon_o = \sqrt{G_c/El_0}$ used for normalization is 0.011. A normalized far-field stress $\overline{\sigma_H}$ = 0.03578 is applied on the left boundary using displacement control, while the normal displacement on the right side is set to zero (see Figure 4.38). The top and bottom boundaries are traction-free. The surface normal fluid flux on the entire outer boundary is set to zero. The Biot coefficient α for the matrix and the weak-soft inclusion is 0.8, and for the tough-stiff

inclusion is 0.6. Glycerin, with a normalized viscosity $\overline{\upsilon^f}$ = 7.5E-8, is used as the fracturing fluid. The initial porosity and the normalized permeability are reported in Table 4-1. A fluid is injected at the left-center of the crack at a constant rate.

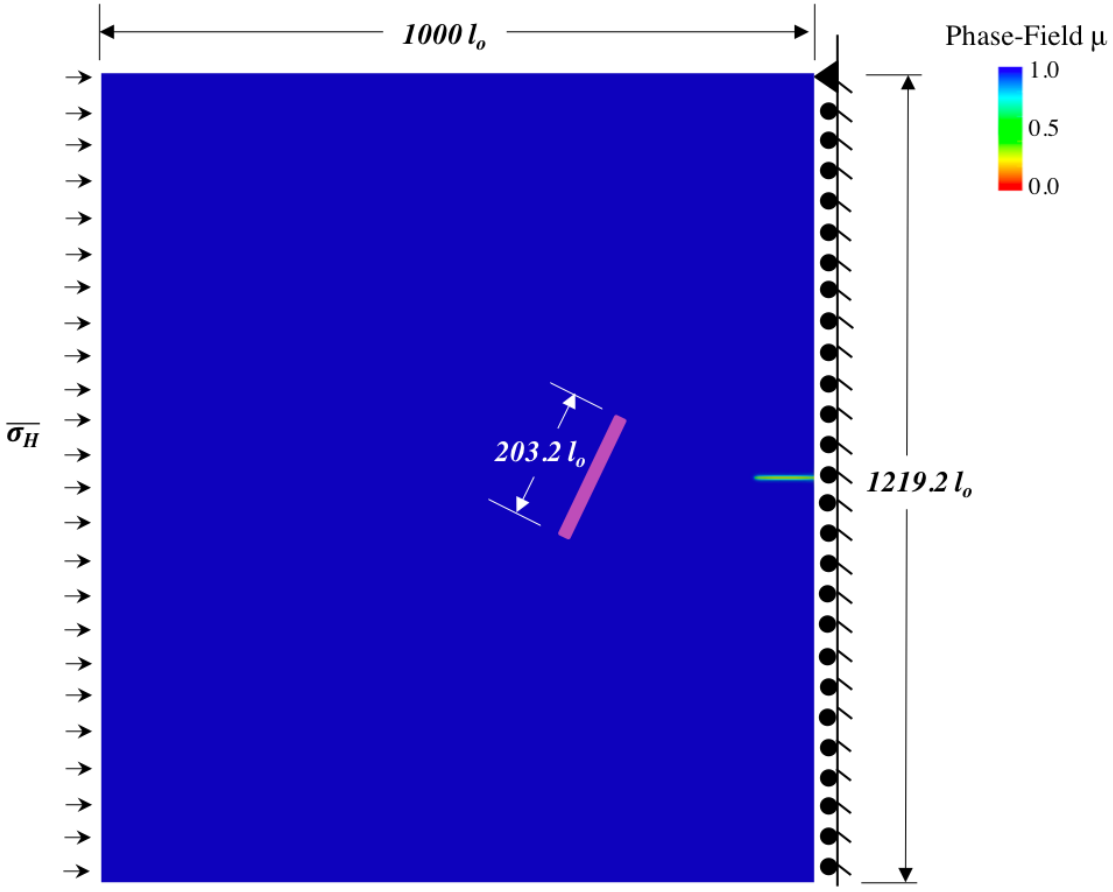

Figure 4.38: Schematic diagram of the domain used for simulating the inclusion Tests 1, 2, 3, and 4.

The first three experimental tests studied the tough-stiff inclusions, and the last test was performed to compare the weak-soft inclusion case. The experimental results for each test will be presented first, followed by the phase-field simulation. Additional simulation is performed to investigate the differences between Test 1 and Test 2.

4.6.1 TEST 1

The aim of Test 1 is to determine how an induced fracture interacts with a thin tough-stiff inclusion placed at a relatively close distance of 19 mm. The orientation of the inclusion has an angle of 61^0 with respect to the horizontal direction. The tough-stiff inclusion has a thickness of 2 mm. As seen in Figure 4.39, the fracture propagates until it reaches the inclusion. After that, it deflects and propagates along the inclusion interface. Once the fracture climbs the inclusion, it reorients itself to be aligned with the direction of the maximum far-field applied stress.

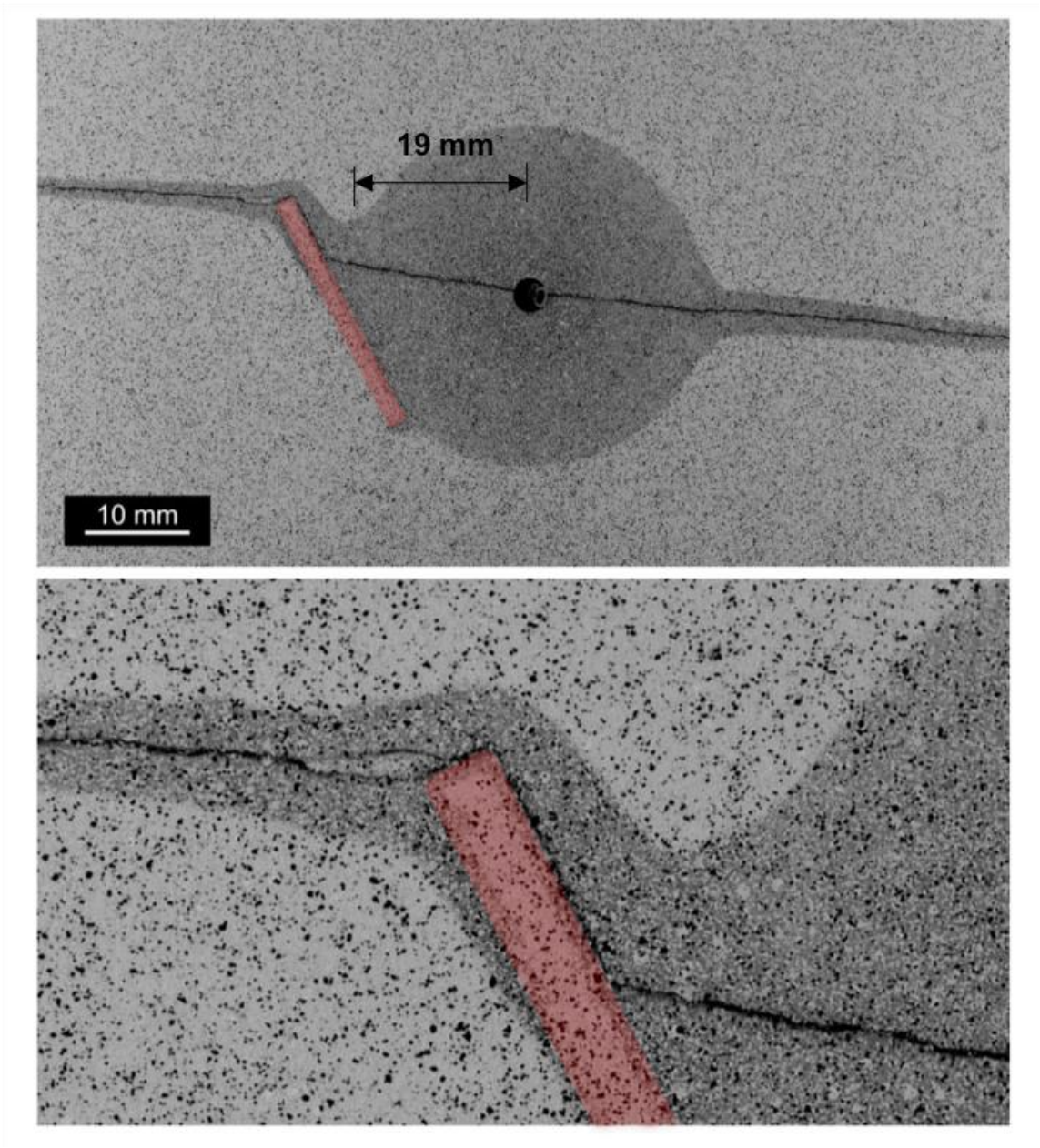

Figure 4.39: Fluid-driven fracture evolution in Test 1 (top) and a magnified view of the deflected section of fracture (bottom) (source [4]).

In the experiment, it was observed that the propagation of the fracture did not align with what presumably should have been the direction of the far-field stress. A probable explanation is that there was an imperfection in the direction of the applied far-field stress during the experiment. Hence, for the purpose of comparison, the axis of the specimen is rotated in the simulation to be aligned with the crack growth direction. Figure 4.40 shows that the crack growth path simulated using the phase-field approach agrees well with the experimental observation. As seen in Figure 4.40, the induced fracture propagates and then is deflected by the tough-stiff inclusion. After it propagates along the inclusion interface and reaches the inclusion edge, it reorients itself to be aligned with the maximum far-field applied stress. Figure 4.40 (b), (c), and (d) show the distribution of the stresses. Stress concentrations can be observed at the fracture tip as well as in the inclusion region near the location of the first turning of the crack.

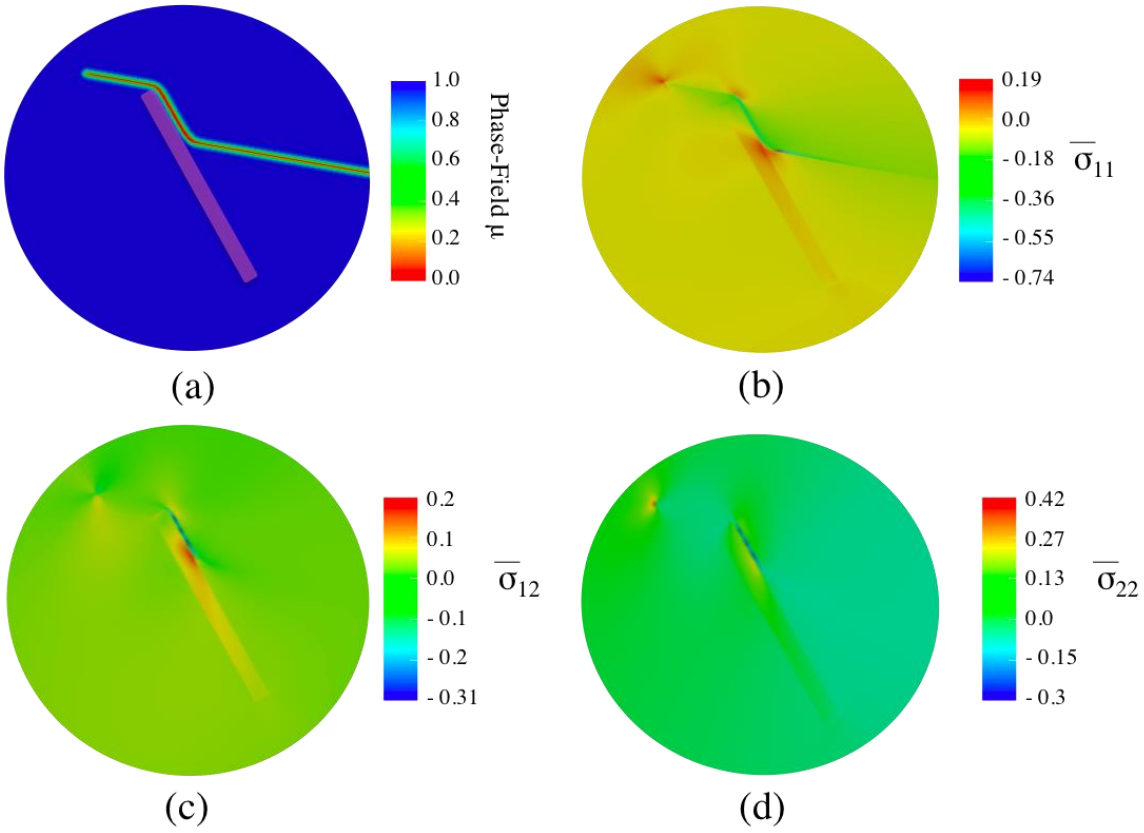

Figure 4.40: A simulation of Test 1 using the phase-field approach. (a) The phase-field solution shows the fracture path. Figures (b), (c), and (d) show the distribution of the stresses. The crack growth path simulated agrees well with the experimental observation shown in Figure 4.39.

4.6.2 TEST 2

The goal of Test 2 is to investigate how an induced fracture interacts with a thin tough-stiff inclusion placed at a relatively large distance of 28 mm from the injection point, as compared to 19 mm in Test 1. The orientation of the inclusion has an angle of 80^0 to the horizontal direction and a thickness of 2 mm. As seen in Figure 4.41, the fracture propagates until it reaches the inclusion, then deflects along the interface and then crosses the inclusion.

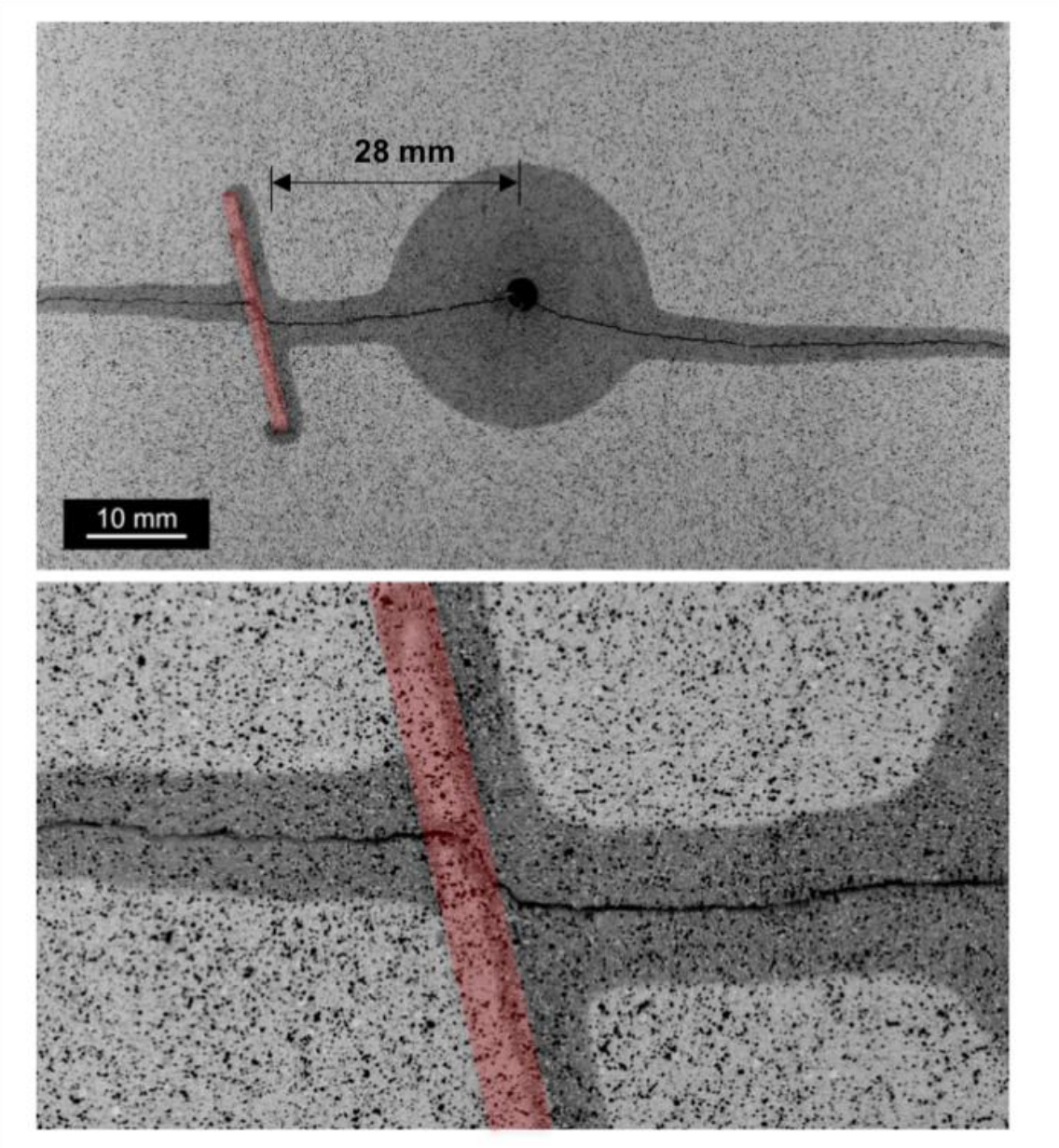

Figure 4.41: Fluid-driven fracture evolution in Test 2 (top) and a magnified view of the deflected section of the fracture (bottom) from (source [4]).

Test 2 has been simulated using the phase-field approach and shows a good agreement with the experimental observation. As seen in Figure 4.42, the induced fracture is deflected by the tough-stiff inclusion, and then finally crosses through the inclusion. Figure 4.42 (b), (c), and (d) show the distribution of the stresses. Stress concentrations can be observed at the fracture tip and on the inclusion interfaces.

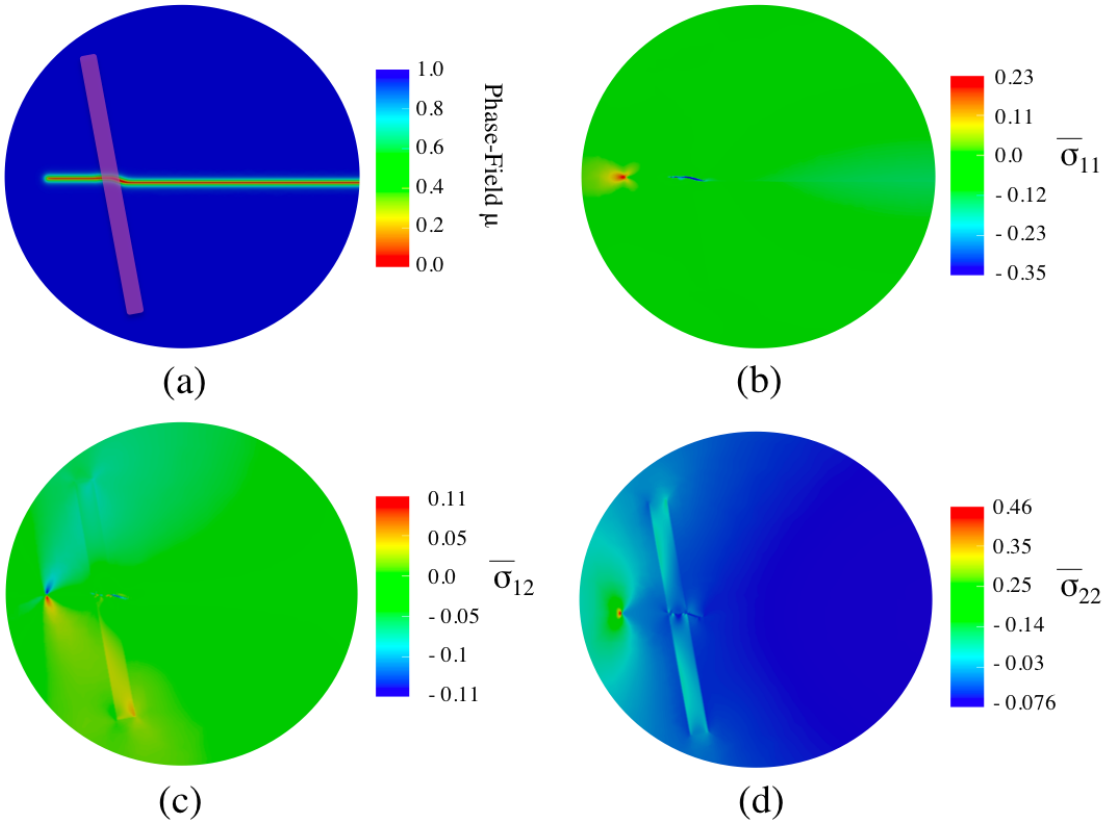

Figure 4.42: A simulation of Test 2 using the phase-field approach. (a) The phase-field solution shows the fracture path. Figures (b), (c), and (d) show the distribution of the stresses. The crack growth path simulated agrees well with the experimental observation shown in Figure 4.41.

There are two main differences between Test 1 and Test 2: the distance between the inclusion and the injection point, and the orientation of the inclusion. To investigate which factor causes this difference in the crack path behavior, an additional simulation has been carried out: the same distance to the injection point as in Test 1, and the same inclusion orientation as in Test 2 are chosen. As seen in Figure 4.43, when the inclusion in Test 1 is reoriented to have a steep angle as in Test 2, the fracture crosses the inclusion. This suggests that the inclusion orientation is the leading cause of the fracture mechanism in these tests. This does not necessarily preclude the role of the distance. However, based on the contrast of the properties of the materials used and the structural conditions in these cases, it is surmised that the orientation of the layer is the main factor in deflecting the fracture.

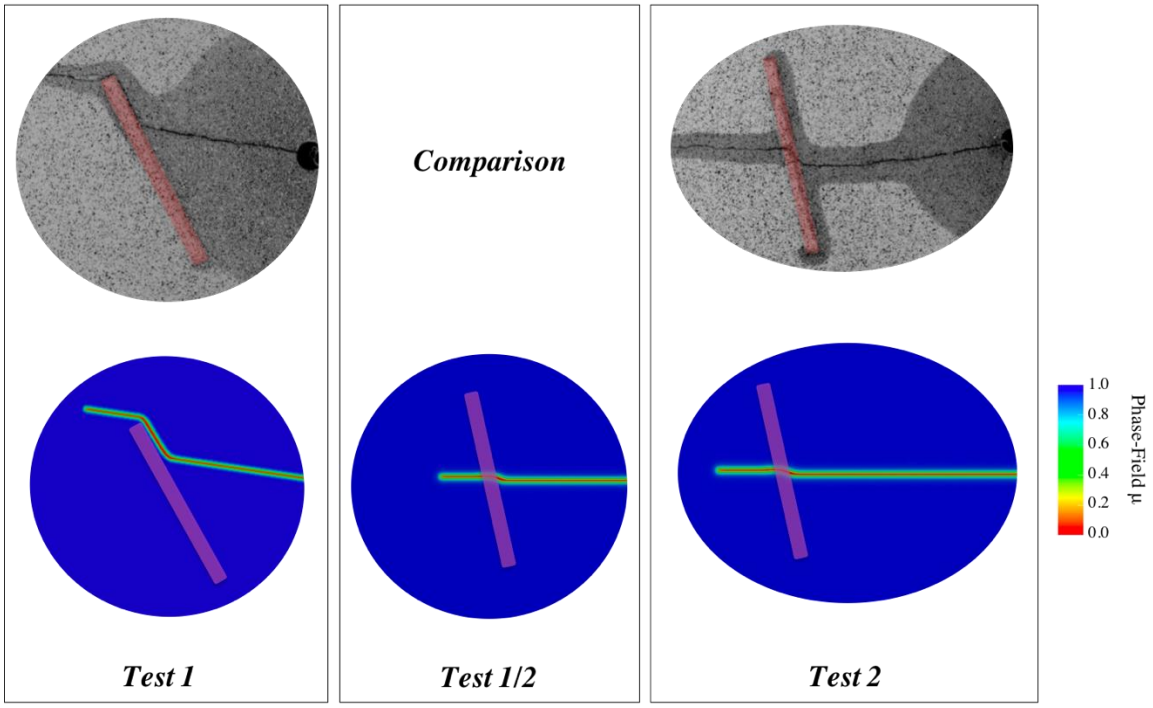

Figure 4.43: An additional simulation is carried out to investigate the difference between Test 1, shown in Figure 4.39, and Test 2, shown in Figure 4.41. In Test 1/2, the same distance to the injection point as in Test 1 and the same inclusion orientation as in Test 2 are chosen. This additional simulation shows that the orientation of the layer is the main factor in deflecting the fracture.

4.6.3 TEST 3

Test 3 studies how an induced fracture interacts with a tough-stiff inclusion but with a larger thickness of 6 mm, as compared with the 2 mm thickness in Test 1. The orientation of the inclusion has an angle of 81^0 relative to the horizontal direction, and is 27 mm from the injection site. As seen in Figure 4.44, the fracture propagates until it reaches the inclusion, then it deflects and propagates along the inclusion interface. Once the fracture runs past the inclusion, it reorients itself to be aligned with the direction of the maximum far-field applied stress. The difference between Test 2 and Test 3 is the thickness of the inclusion. The angle of the inclination of the inclusion is a steep 80^0 as in Test 2, but the thicker inclusion deflects the fracture, while the thinner inclusion allows the crack to pass through.

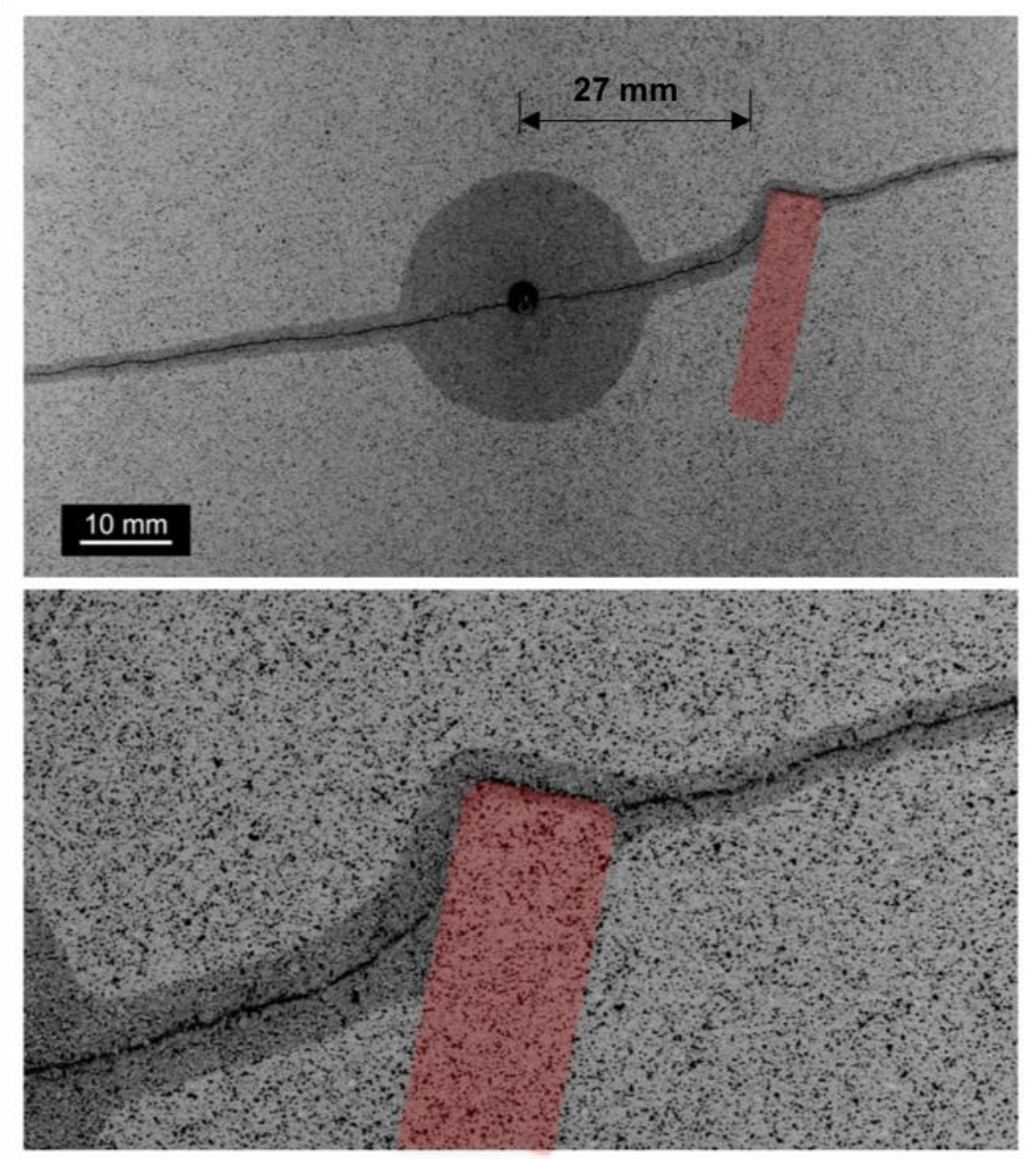

Figure 4.44: Fluid-driven fracture's evolution in Test 3 (top) and a magnified view of the deflected section of the fracture (bottom) (source [4]).

Again as in Test 1, it was observed that the propagation of the initial fluid-driven fracture was not aligned with what presumably should have been the direction parallel to the maximum far-field stress. An imperfection in the direction of the applied far-field stress likely occurred during the experiment. As such, the axis of the specimen is again rotated to be aligned with the crack growth direction for the phase-field calculation. The simulation results for Test 3 again produced a good agreement with the experimental observation. As seen in Figure 4.45, the induced fracture propagates and then is deflected by the tough-stiff inclusion. When fracture reaches the inclusion edge, it reorients itself to be parallel to the maximum far-field stress applied. Figure 4.45 (b), (c), and (d) show the distribution of the stresses. Stress concentrations can be observed at the fracture tip as well as the region near the fracture kinks.

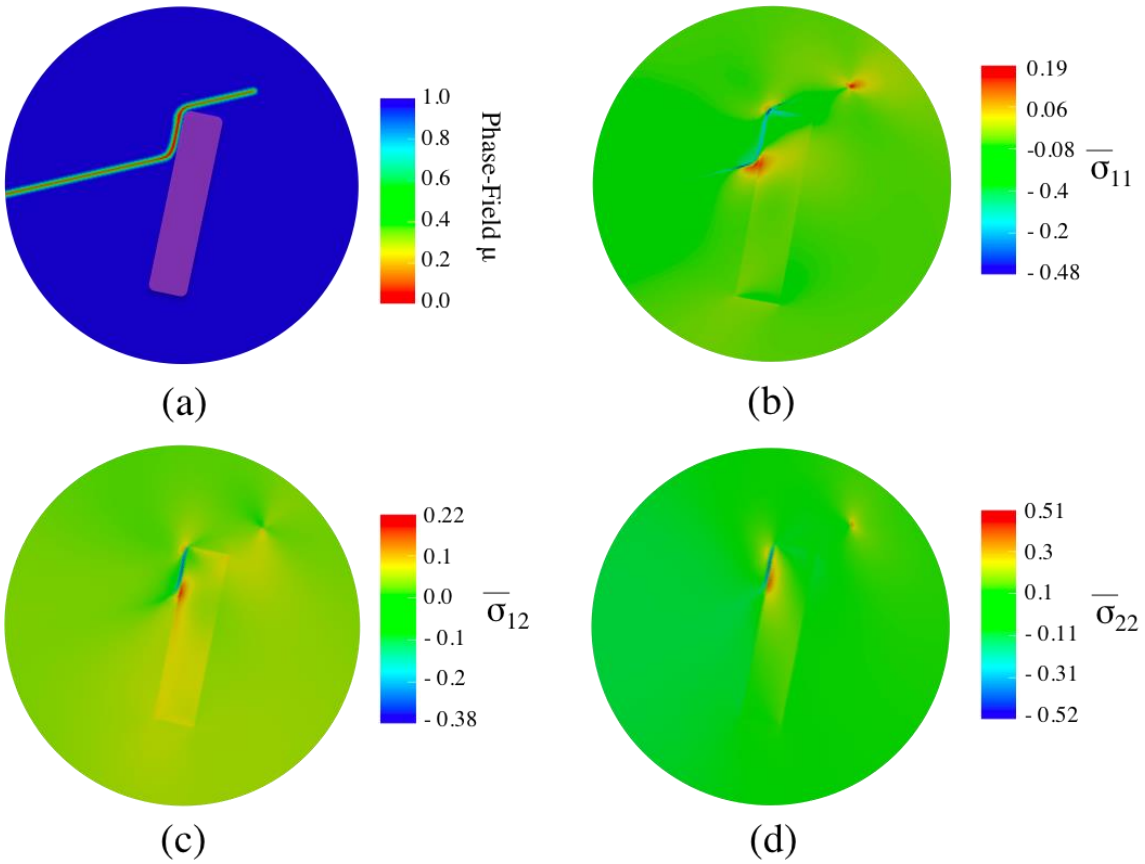

Figure 4.45: A simulation of Test 3 using the phase-field approach. (a) The phase-field solution shows the fracture path. Figures (b), (c), and (d) show the distribution of the stresses. The crack growth path simulated agrees well with the experimental observation shown in Figure 4.44.

4.6.4 TEST 4

The goal of Test 4 is to investigate how an induced fracture interacts with a weak-soft inclusion, as compared to the tough-stiff inclusion in Test 3. The orientation of the inclusion has an angle of 81^0 to the horizontal direction and placed at 27 mm from the injection site. As seen in Figure 4.46, the fracture propagates and crosses the inclusion in a fairly straight direction towards direction parallel to the maximum far-field stress direction. The difference in the behavior between Test 2 and Test 3 illustrates that the tough-stiff inclusion has a greater tendency to deflect the fracture than does the weak-soft inclusion.

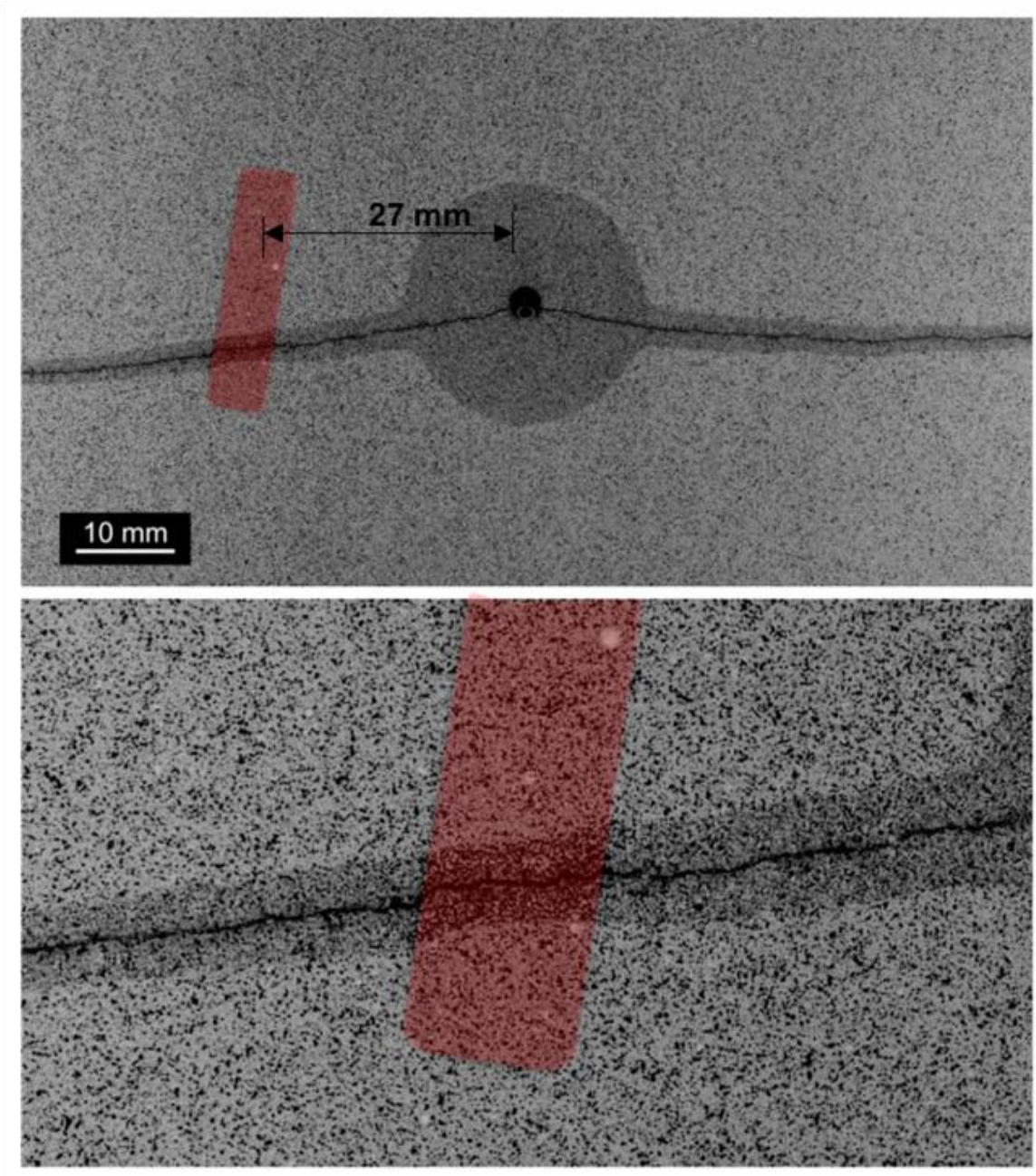

Figure 4.46: Fluid-driven fracture evolution in Test 4 (top) and a magnified view of the deflected section of the fracture (bottom) (source [4]).

Test 4 is simulated using the phase-field approach and again shows good agreement with the experimental observations. As seen in Figure 4.47, the induced fracture propagates and crosses the inclusion. Figure 4.47 (b), (c), and (d) show the distribution of the stresses. Stress concentrations are observed at the fracture tip and on the inclusion interfaces.

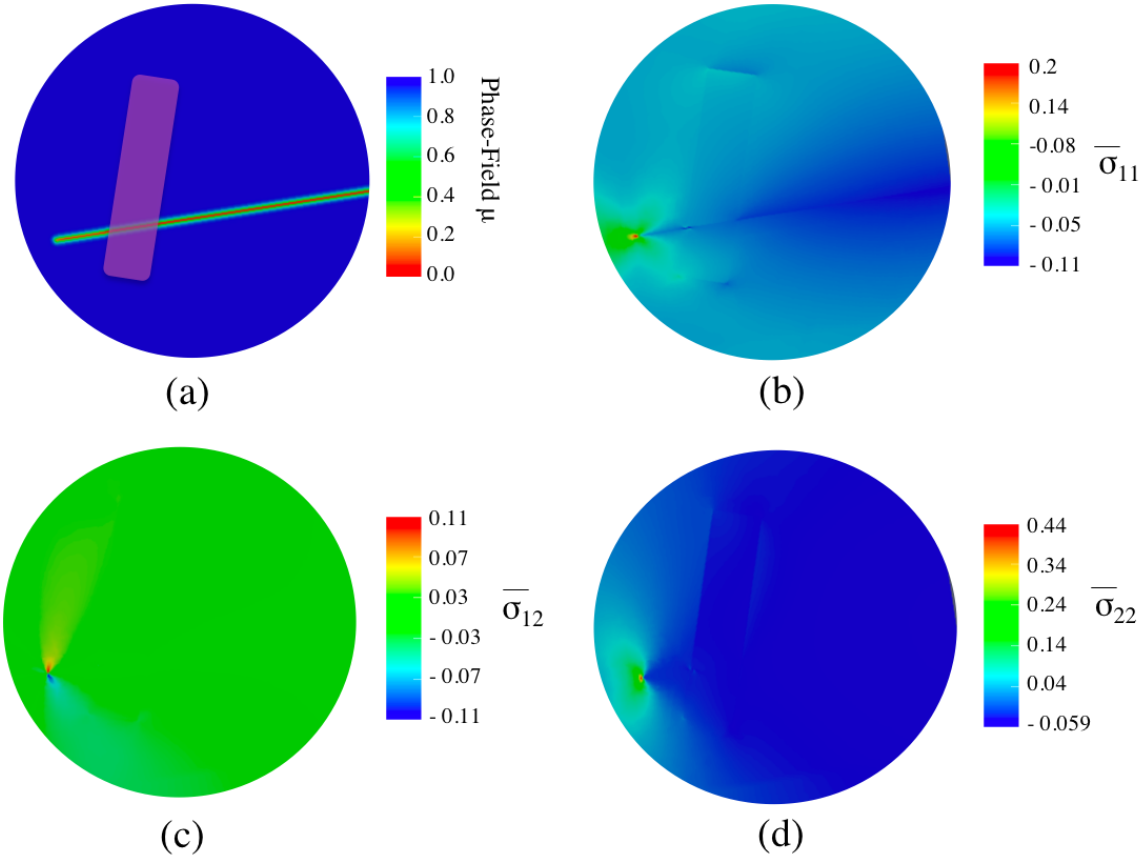

Figure 4.47: A simulation of Test 4 using the phase-field approach. (a) The phase-field solution shows the fracture path. Figures (b), (c), and (d) show the distribution of the stresses. The crack growth path simulated agrees well with the experimental observation shown in Figure 4.46.

In conclusion, the phase-field approach was used to simulate a set of inclusion problems and compared them to experimental observations. Simulations for all four tests using the phase-field approach produced a good agreement with the experimental observations. The goal of these experiments is to understand how induced fractures interact with cemented natural fractures or what we are calling “inclusions’’. Both experiments and simulations show that a tough-stiff inclusion with a shallow orientation with respect to the maximum far-field stress direction has a greater tendency to deflect the fracture than does an inclusion with a steeper orientation. The thicker tough-stiff inclusion acts as a barrier that deflects fracture more so than a thinner inclusion.

4.7 Implementation in Three Dimensions

This section describes the extension of the phase-field model for the hydraulic fracture to three dimensions (3D). First, the extension to 3D has been validated against the analytic solution for the phase-field for a completely separated surface. The simulation domain is a very long rectangular beam with a length of $200l_0$. The nodes on the *z*–*y* plane with $x = 0$ are taken to be damaged with $\mu = 0$. The analytic solution for the phase-field for this problem is as follows:

$$\mu(x) = 1 - e^{-\left|\frac{x}{2l_0}\right|} \tag{4.12}$$

As seen in Figure 4.48, the numerical and the analytic solutions for the phase-field are in agreement. This serves as the first basic validation for the 3D implementation.

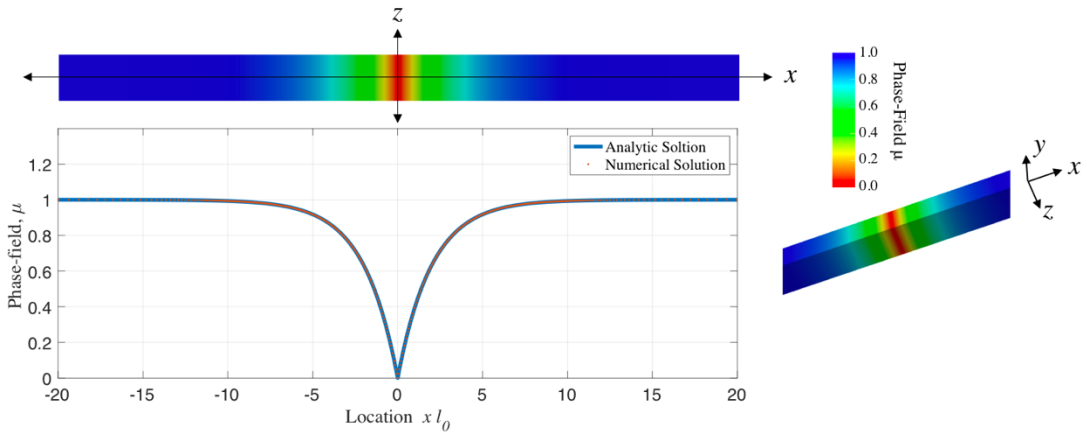

Figure 4.48: A comparison of the analytic solution with the numerical solution for a separated surface.

Next, two benchmark problems will be tested as additional validation cases: 1) a mechanical fracture problem, and 2) a hydraulic fracture problem. For the mechanical problem, a compact tension CT specimen is simulated. For the hydraulic fracture problem, a fluid-driven circular crack is tested.

4.7.1 COMPACT TENSION SPECIMEN TEST

The theory for phase-field modeling of fracture in brittle materials is presented in Chapter 3. In this example, only the mechanical drivers for fracture are considered, and no fluid flow is simulated. The benchmark problem simulated is a compact tension CT specimen, where the dimensions of specimen are shown in Figure 4.49. The boundary of the circular holes is displaced u_0 in an opening mode. All other surfaces are traction free.

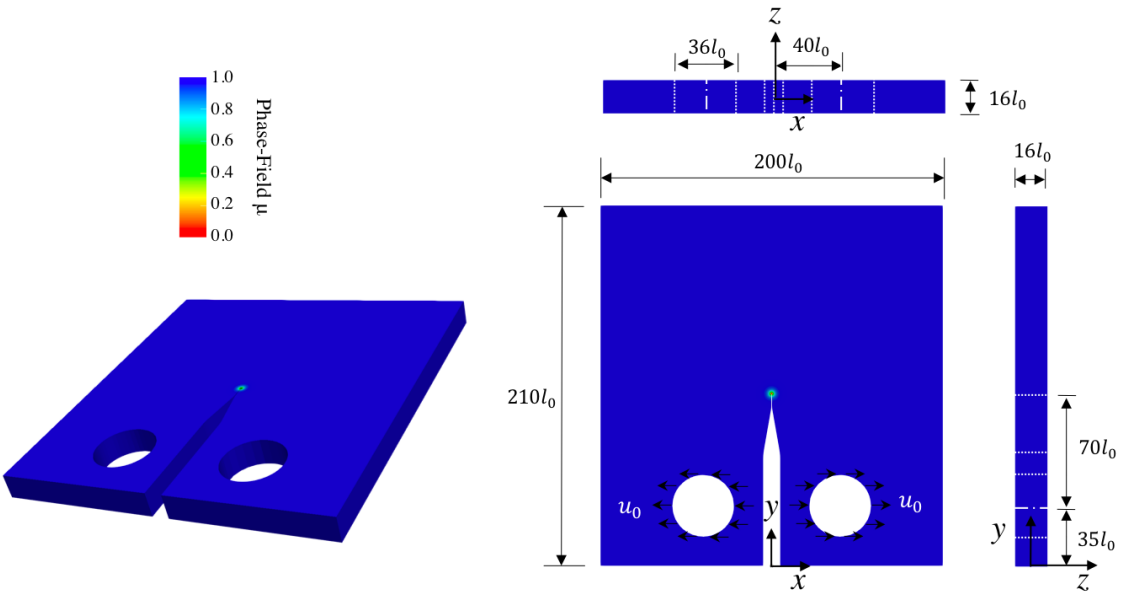

Figure 4.49: (a) Compact tension CT specimen b) The dimensions of the specimen are $200l_0$ *x* $210l_0$ *x* $16l_0$.

As seen in Figure 4.50, as the displacement u_0 increases, the crack grows. Eventually when the $u_0/\varepsilon_0 l_0$ = 15, the fracture grows until the specimen splits into two parts. In the figure, the deformed shape is presented with a magnification scale factor of 150 to make the deformation more obvious.

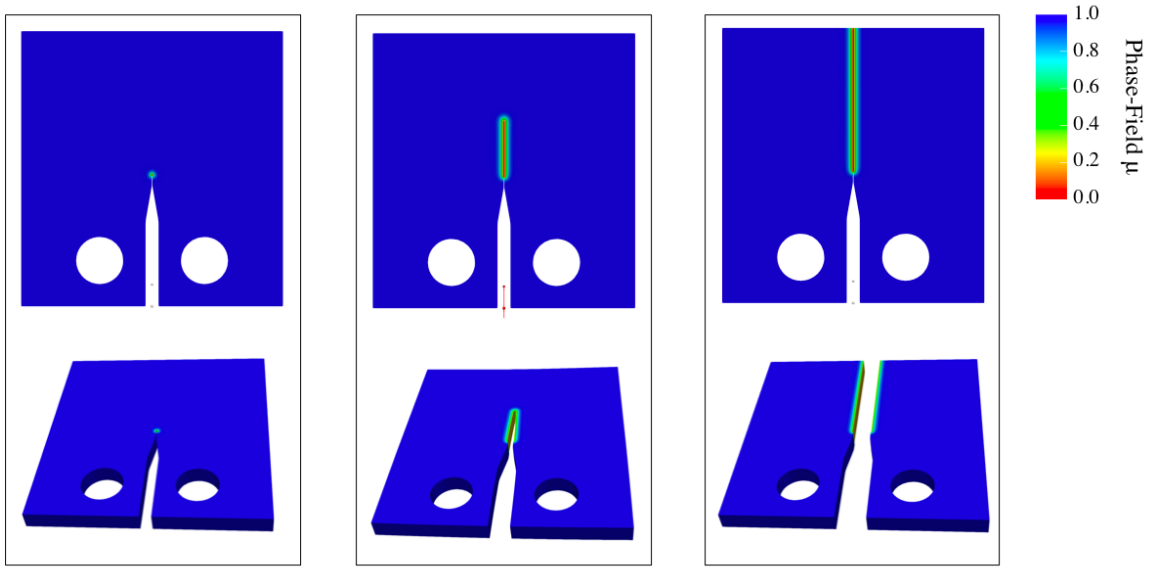

a) Initial State b) Intermediate State a) Final State

Figure 4.50: Fracture growth trajectories in a deformed shape with a scale factor of 150 for compact tension CT specimen: (a) initial state; (b) fracture state at applied displacement $u_1/\varepsilon_0 l_0$ = 25 ; and (c) final state at applied displacement $u_1/\varepsilon_0 l_0$ = 52 for the specimen when it split into two parts.

4.7.1 PRESSURIZED CIRCULAR CRACK

Here, the benchmark problem of a fluid-driven circular fracture is performed (see Figure 4.51). A domain with dimensions $2000l_0$ x $2000l_0$ x $2000l_0$ is assumed, but only one quarter is simulated. A phase-field circular crack with a radius of $25l_0$ is initialized at the center on the domain. On the symmetry planes, normal displacements are set to zero,

and the surfaces are traction-free in the tangential directions. On the outer boundaries, the surface normal displacements and the surface normal fluid flux are set to zero. The Biot coefficient α is 0.45, the initial porosity is ϕ_0= 0.1, and the normalized permeability is $\bar{\kappa}$ =10^{-14}. A fluid is injected at the center of the crack at a constant rate $\bar{Q}$= 0.005.

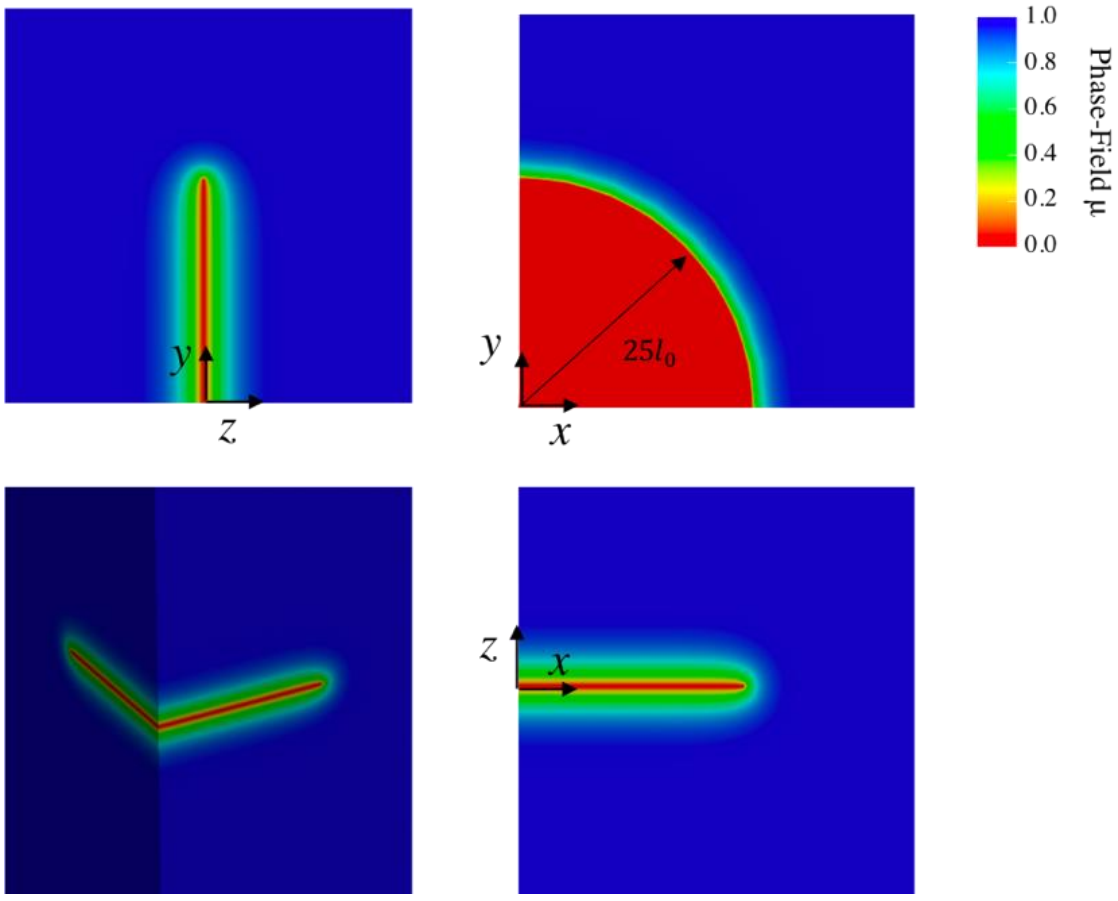

Figure 4.51: A rectangular domain of 2000l_0 x 2000l_0 x 2000l_0 has a central circular crack of radius = 25l_0. Only one-quarter of the domain is simulated, and symmetry boundary conditions are applied on symmetrical faces.

As seen in Figure 4.52, the crack propagates in a symmetrical radial direction, as is expected. When the injected pressure $p/E\varepsilon_0$ reaches 0.15, the fracture starts to propagate until the simulation is terminated when V/l_0^3 reaches 1.12.

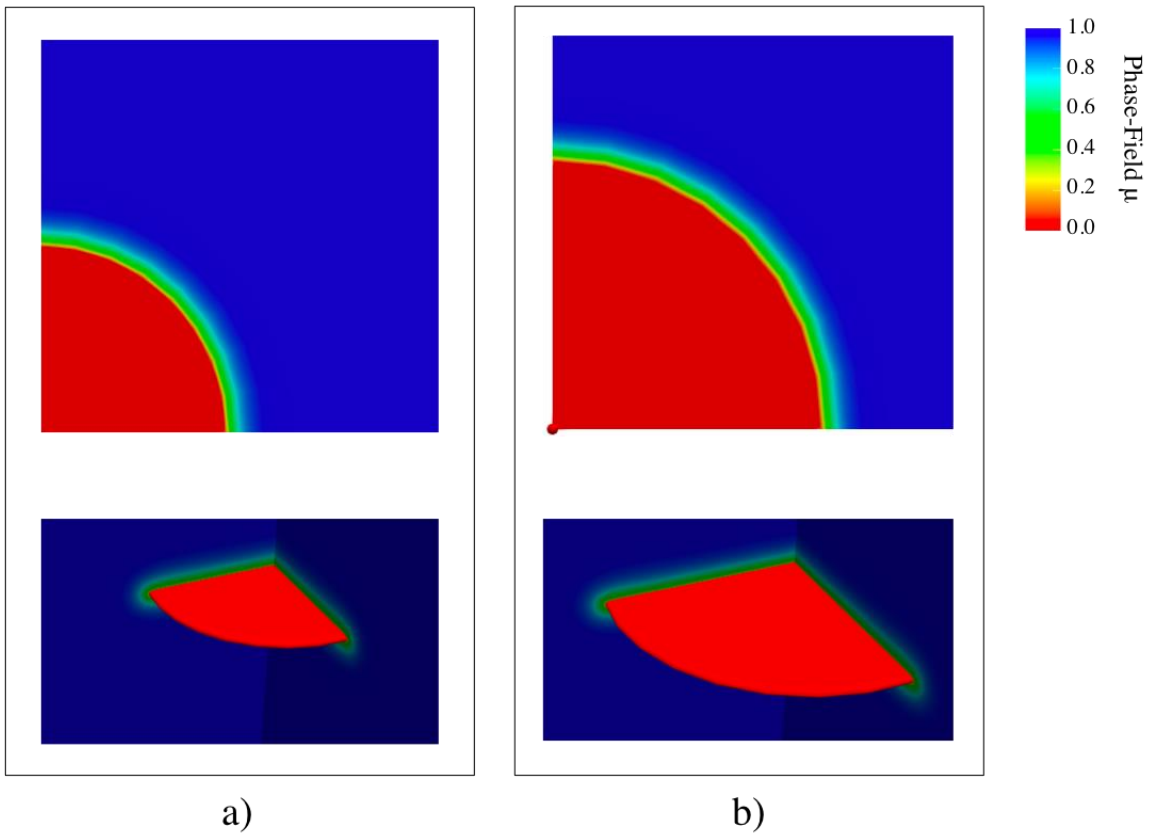

Figure 4.52: Fracture growth: (a) initial state; (b) the fracture propagates radially at load step V/l_0^3 = 1.12 . Top figures are cross-sections at the center of the fracture. The bottom figures are three dimensional views. The Poisson's ratio ν = 0.25, ε_0 = 0.001, $l_0^2/\kappa = 10^{12}$, α = 0.45, ϕ_0 = 0.1, c^f / ρ_0^f = 0.01364, and $\upsilon^f/E\varepsilon_0 t_0 = 5 \times 10^{-12}$.

Chapter 5. Conclusion and Future Work

The phase-field approach for the fracture has been shown to be a powerful tool for simulating very complex fracture topologies, including the turning, branching, and merging of cracks. In contrast to fracture models that explicitly track the crack surfaces, crack propagation and the evolution thereof arise out of the solution to a partial differential equation governing the evolution of a phase-field damage parameter. In the present model, the physics of flow through porous media and cracks is coupled with the mechanics of fracture. Darcy-type flow is modeled in the intact porous medium, which transitions to a Stokes-type flow regime within open cracks. This phase-field model is implemented to gain insights into the propagation behavior of fluid-driven cracks.

One outstanding issue with phase-field fracture models is the decomposition of the strain energy that is required to ensure that compressive stress states do not cause damage evolution. The proper representation of the strain energy function to reflect this fracture phenomenon is studied. The strain energy is constructed in terms of principal strains in such a way that it has two parts: tensile and compressive, where the degradation function only applies to the tensile part. It has been shown that Miehe's decomposition [1] of the strain energy function allows damage to evolve under purely compressive stress states. This issue is resolved using an approach based on the behavior of the masonry-like materials [2, 3]. This approach ensures that cracks do not grow under compressive stresses states, which is actually of critical importance for hydraulic fracture where the far-field stresses are primarily compressive.

To demonstrate the capabilities of phase-field modeling for fluid-driven fractures, four general types of problems have been simulated: 1) interactions of fluid-driven, natural, and proppant-filled cracks; 2) crack growth through different material layers; 3) fluid-driven crack growth under the influence of in-situ far-field stresses; and 4) crack interactions with inclusions. The simulations illustrate the capabilities of the phase-field model to capture interesting and complex crack growth phenomena. They also give some insight into some of the issues related to fracture treatments in the oil and gas industries.

For fracture interactions with other fractures, three main problems were studied. The first problem was on the interactions of parallel induced fractures and the effect of the fracture spacing on the crack propagation behavior. Decreasing the fractures spacing does not necessarily increase the drainage area because of the stresses shadow effect that retards the propagation of internal fractures. Additionally, a shorter fracture spacing reduces the crack aperture of the induced fractures which can cause problems with proppant placement. The interaction between fluid-driven fractures and natural fractures has also been investigated. It was demonstrated that pre-existing natural fractures can deflect the induced fractures toward unfavorable growth directions. Finally, the problem of induced fracture interacting with a fracture filled with proppants was studied. Like natural fractures, proppant filled cracks can disturb the propagation of the induced fracture. Two factors were investigated: the aperture of the propped fracture and the distance separating the induced fracture from a propped fracture. The simulations indicated that a fracture filled with proppants alters the in-situ stresses around its location causing the fluid-driven fracture to slow down and divert from its original path.

To investigate how fluid-driven crack interacts with material interfaces, the problem of an induced fracture interacting with a layer of different fracture and/or elastic properties was studied. Several factors that could influence the fracture behavior when encountering a layer were included in the simulations. A very tough layer has the ability to deflect the induced fracture. The contrast in the modulus of elasticity of the layer relative to the matrix was not sufficient to make the layer act as a barrier in the absence of an increase in the layer toughness. Additionally, a layer with a steep orientation relative to the crack direction has less of a tendency to deflect the fracture. Also, a thicker layer has a greater tendency to deflect the induced crack than a thin layer. Finally, it appears that the distance between the injection point and the layer does not play a significant role in deflecting the fracture.

In section 4.5, the role of in-situ stresses on the crack paths was studied. It was shown that in all of the problems investigated that with a sufficient stress level, the induced fracture will grow to orient itself to be aligned with the direction perpendicular to the minimum in-situ principle stress. The fracture kink angle was also studied for different initial crack orientations and in-situ stresses. The kink angle φ is the angle between the initial orientation of the fracture and the extension of the propagated fracture. The kink angle increases as the in-situ maximum stress increases. The kink angle also increases as the initial orientation of the crack deviates from the maximum in-situ stress direction

Experiments have recently been performed by Altammar [4] to understand how fluid-driven cracks interact with inclusions. Three tests with high toughness and high stiffness inclusions have been carried out to understand the effects of the orientation angle,

the thickness, and the material properties. Additionally, one test with high toughness and high stiffness inclusion has been conducted to compare this case to the tough inclusion cases. To replicate these experiments numerically and to gain a mechanistic understanding of the behaviors, simulations of these configurations were performed using phase-field modeling. All of the simulations had good agreement with the experimental observations and were able to capture the trends of crack deflection versus interface or inclusions crossing in all four test cases. Both the experiments and simulations showed a clear tendency for the induced hydraulic fracture to cross thick natural fractures filled with materials weaker and softer than the host rock and to be diverted by thick natural fractures with tougher and stiffer filling materials. Lastly, in addition to these two-dimensional analyses, the phase-field model was extended to three-dimensions. Two benchmark problems were simulated: a compact tension CT specimen test and a fluid-driven circular crack.

In regard to future work, recall that in the layer problems, only two fluid viscosities were investigated. The two viscosities were chosen to reside in different regimes of toughness versus viscosity dominance. The results suggested a weak dependence of the crack growth modes (deflection/crossing the layer) on the injected fluid viscosity. However, it would be of interest in the applications of hydraulic fracture treatment processes to more thoroughly study the fracture behaviors over a wider range of viscosities that might demonstrate the sensitivity of the behavior on the viscosity. Additionally, in the inclusion problem simulations, the inclusion and the matrix have been assumed to be perfectly bonded. However, it was observed two of the experiments: Test 1 and Test 3, that

the fracture had been directed along an interface near the top side of the inclusion. In contrast to the perfectly bonded interface condition assumed in the phase-field simulations, the inclusion and the matrix may be, for example, partially or weakly bonded. In this situation, the crack will prefer to grow along the weak interface, and the behavior of the fracture observed in the experiments may then be even more accurately captured by the phase-field simulations. This observed difference between the phase-field simulations and the experimental observations suggests that the interface condition, ranging from strongly bonded to weakly bonded, can also play role in the fracture growth behavior.

Appendix: Dimensionless Form of the Model Equations

The normalizations for the model parameters are as follows:

Normalized quantity	Form	Comments
Energy release rate, $\overline{G_c}$ =	$\frac{G_c}{G_{c,m}}$	The G_c is normalized by the G_c of the matrix. In homogenous materials $\overline{G_c}$ = 1.
Stiffness tensor, $\bar{c}_{ijkl}$ =	$\frac{c_{ijkl}}{E}$	E is Young's Modulus.
Characteristic strain, ε_0 =	$\sqrt{\frac{G_c}{E l_0}}$	l_0 is the process zone length.
Dimensionless coordinate, $\bar{x}_i$ =	$\frac{x_i}{l_0}$	
Dimensionless displacements, $\bar{u}_i$ =	$\frac{u_i}{\varepsilon_0 l_0}$	
Normalized strain, $\bar{\varepsilon}_{ij}$ =	$\frac{\varepsilon_{ij}}{\varepsilon_0}$	
Dimensionless stresses, $\bar{\sigma}_{ij}$ =	$\frac{\sigma_{ij}}{E\varepsilon_0}$	
Normalized body forces, $\bar{b}_i$ =	$\frac{b_i l_0}{E\varepsilon_0}$	
Normalized traction, $\bar{t}_i$ =	$\frac{t_i l_0}{E\varepsilon_0}$	

Normalized pressure, $\bar{p}$ =	$\frac{p}{E\varepsilon_0}$	
Normalized intrinsic permeability, $\bar{\kappa}$ =	$\frac{\kappa}{l_0^2}$	
Normalized fluid velocity, $\bar{w}_i$ =	$\frac{w_i t_0}{l_0}$	t_0 is a characteristic time scale.
Normalized fluid viscosity, $\bar{v}^f$ =	$\frac{v^f}{t_0 E\varepsilon_0}$	
Normalized deviatoric fluid stress, $\bar{\tau}_{ij}$ =	$\frac{\tau_{ij}}{E\varepsilon_0}$	
Normalized internal micro-force, $\bar{\pi}$ =	$\frac{\pi}{E\varepsilon_0^2}$	
Normalized external body micro-force, $\bar{\gamma}$ =	$\frac{\gamma}{E\varepsilon_0^2}$	
Normalized micro-force vector, $\bar{\xi}_i$ =	$\frac{\xi_i}{l_0 E\varepsilon_0^2}$	
Normalized injection rate $\bar{Q}$ =	$\frac{Q t_0}{l_0^3}$	

Reference

1. Miehe, C., M. Hofacker, and F. Welschinger, *A phase field model for rate-independent crack propagation: Robust algorithmic implementation based on operator splits.* Computer Methods in Applied Mechanics and Engineering, 2010. **199**(45): p. 2765-2778.
2. Del Piero, G., *Constitutive equation and compatibility of the external loads for linear elastic masonry-like materials.* Meccanica, 1989. **24**(3): p. 150-162.
3. Maurizio Angelillo, L.C.a.A.F., *A numerical model for masonry-like structures.* Journal of Mechanics of Materials and Structures, 2010. **5**(4): p. 583-615.
4. AlTammar, M.J., *Experimental Studies in Hydraulic Fracture Growth: Fundamental Insights and Validation Experiments for Geomechanical Models*, in *Department of Petroleum and Geosystems Engineering*. 2018, The University of Texas at Austin: UT System.
5. Bell, F.G., *Engineering Geology and Construction*. 2004, New York: CRC Press.
6. Moschovidis, Z.A., et al., *Disposal of Oily Cuttings by Downhole Periodic Fracturing Injections, Valhall, North Sea: Case Study and Modeling Concepts.* SPE Drilling & Completion, 1994. **9**(04): p. 256-262.
7. Banks, D., et al., *Permeability and stress in crystalline rocks.* Terra Nova, 1996. **8**(3): p. 223-235.
8. Less, C. and N. Andersen, *Hydrofracture: State Of The Art In South Africa.* Applied Hydrogeology, 1994. **2**(2): p. 59-63.

9. Ghassemi, A., *A Review of Some Rock Mechanics Issues in Geothermal Reservoir Development.* Geotechnical and Geological Engineering, 2012. **30**(3): p. 647-664.

10. Pine, R.J. and A.S. Batchelor, *Downward migration of shearing in jointed rock during hydraulic injections.* International Journal of Rock Mechanics and Mining Sciences & Geomechanics Abstracts, 1984. **21**(5): p. 249-263.

11. Administration, U.S.E.I. *Hydraulically fractured horizontal wells account for most new oil and natural gas wells*. 2018; Available from: https://www.eia.gov/todayinenergy/detail.php?id=34732.

12. Administration, U.S.E.I., *Trends in U.S. Oil and Natural Gas Upstream Costs*. 2016, U.S. Department of Energy: Washington.

13. Gale, J., R. Reed, and J. Holder, *Natural fractures in the Barnett Shale and their importance for hydraulic fracture treatments*. Vol. 91. 2007. 603-622.

14. Gale, J.F.W., et al., *Natural fractures in shale: A review and new observations.* AAPG Bulletin, 2014. **98**(11): p. 2165-2216.

15. Geology.com. *World Shale Gas Resources*. Available from: https://geology.com/energy/world-shale-gas/.

16. Gidley, J.L., *Recent advances in hydraulic fracturing*. 1989, United States: Richardson, TX (USA); Society of Petroleum Engineers.

17. Baihly, J.D., et al., *Shale Gas Production Decline Trend Comparison over Time and Basins*, in *SPE Annual Technical Conference and Exhibition*. 2010, Society of Petroleum Engineers: Florence, Italy. p. 26.

18. Wright, C.A., et al., *Reorientation of propped refracture treatments*, in *Rock Mechanics in Petroleum Engineering*. 1994, Society of Petroleum Engineers: Delft, Netherlands. p. 8.

19. Invester, U.G. *The Sand Demand: Finding Opportunities Beyond Direct Shale Plays*. 2014; Available from: http://www.usfunds.com/investor-library/frank-talk/the-sand-demand-finding-opportunities-beyond-direct-shale-plays/#.XOoB4y2ZPy8.

20. Warpinski, N.R. and L.W. Teufel, *Influence of Geologic Discontinuities on Hydraulic Fracture Propagation (includes associated papers 17011 and 17074).* Journal of Petroleum Technology, 1987. **39**(02): p. 209-220.

21. Dahi Taleghani, A. and J.E. Olson, *How Natural Fractures Could Affect Hydraulic-Fracture Geometry.* SPE Journal, 2013. **19**(01): p. 161-171.

22. Soliman, M.Y., L.E. East, and D.L. Adams, *Geomechanics Aspects of Multiple Fracturing of Horizontal and Vertical Wells.* SPE Drilling & Completion, 2008. **23**(03): p. 217-228.

23. Warpinski, N.R. and P.T. Branagan, *Altered-Stress Fracturing.* Journal of Petroleum Technology, 1989. **41**(09): p. 990-997.

24. Ghassemi, A., *1 - Application of rock failure simulation in design optimization of the hydraulic fracturing*, in *Porous Rock Fracture Mechanics*, A.K. Shojaei and J. Shao, Editors. 2017, Woodhead Publishing. p. 3-23.

25. Fisher, M.K., et al., *Optimizing Horizontal Completion Techniques in the Barnett Shale Using Microseismic Fracture Mapping*, in *SPE Annual Technical*

Conference and Exhibition. 2004, Society of Petroleum Engineers: Houston, Texas. p. 11.

26. Schelumberger. *Oilfield Review*. 2014; Available from: https://www.slb.com/~/media/Files/resources/oilfield_review/ors14/aut14/composite.pdf.

27. Cheng, Y., *Impacts of the Number of Perforation Clusters and Cluster Spacing on Production Performance of Horizontal Shale-Gas Wells.* SPE Reservoir Evaluation & Engineering, 2012. **15**(01): p. 31-40.

28. Supping Peng, J.Z., *In-situ stress and pore pressure*, in *Engineering Geology for Underground Rocks*. 2007, Springer Berlin Heidelberg: Berlin, Heidelberg. p. 45-74.

29. King, G.E., *Thirty Years of Gas Shale Fracturing: What Have We Learned?*, in *SPE Annual Technical Conference and Exhibition*. 2010, Society of Petroleum Engineers: Florence, Italy. p. 50.

30. Abass, H.H., S. Hedayati, and D.L. Meadows, *Nonplanar Fracture Propagation From a Horizontal Wellbore: Experimental Study.* SPE Production & Facilities, 1996. **11**(03): p. 133-137.

31. Cipolla, C.L., et al., *The Relationship Between Fracture Complexity, Reservoir Properties, and Fracture-Treatment Design.* SPE Production & Operations, 2010. **25**(04): p. 438-452.

32. Waters, G.A., et al., *Simultaneous Hydraulic Fracturing of Adjacent Horizontal Wells in the Woodford Shale*, in *SPE Hydraulic Fracturing Technology Conference*. 2009, Society of Petroleum Engineers: The Woodlands, Texas. p. 22.

33. Zhou, J., Y. Jin, and M. Chen, *Experimental investigation of hydraulic fracturing in random naturally fractured blocks.* International Journal of Rock Mechanics and Mining Sciences, 2010. **47**(7): p. 1193-1199.

34. Breyer, J.A., et al., *Facies, Fractures, Pressure and Production in the Eagle Ford Shale (Cretaceous) between the Maverick Basin and the San Marcos Arch, Texas, USA*, in *Unconventional Resources Technology Conference, Denver, Colorado, 12-14 August 2013*. p. 1556-1576.

35. Comer, J.B., *Stratigraphic Analysis of the Upper Devonian Woodford Formation, Permian Basin, West Texas and Southeastern New Mexico*. 1991, The University of Texas at Austin: Bureau of Economic Geology.

36. Donovan, A.D. and S. Staerker, *Sequence Stratigraphy of the Eagle Ford (Boquillas) Formation in the Subsurface of South Texas and Outcrops of West Texas.* TRANSACTIONS- GULF COAST ASSOCIATION OF GEOLOGICAL SOCIETIES, 2010. **60**.

37. Mullen, J., *Petrophysical Characterization of the Eagle Ford Shale in South Texas*, in *Canadian Unconventional Resources and International Petroleum Conference*. 2010, Society of Petroleum Engineers: Calgary, Alberta, Canada. p. 19.

38. Kirk-Burnnand, E., et al., *Hydraulic Fracture Design Optimization in Low Permeability Coals, Surat Basin, Australia*, in *SPE Asia Pacific Unconventional*

Resources Conference and Exhibition. 2015, Society of Petroleum Engineers: Brisbane, Australia. p. 16.

39. Fisher, M.K. and N.R. Warpinski, *Hydraulic Fracture-Height Growth: Real Data*, in *SPE Annual Technical Conference and Exhibition*. 2011, Society of Petroleum Engineers: Denver, Colorado, USA. p. 18.

40. Daneshy, A.A., *Factors Controlling the Vertical Growth of Hydraulic Fractures*, in *SPE Hydraulic Fracturing Technology Conference*. 2009, Society of Petroleum Engineers: The Woodlands, Texas. p. 11.

41. Simonson, E.R., A.S. Abou-Sayed, and R.J. Clifton, *Containment of Massive Hydraulic Fractures.* Society of Petroleum Engineers Journal, 1978. **18**(01): p. 27-32.

42. Daneshy, A.A., *Hydraulic Fracture Propagation in Layered Formations.* Society of Petroleum Engineers Journal, 1978. **18**(01): p. 33-41.

43. AlTammar, M.J. and M.M. Sharma, *Effect of Geological Layer Properties on Hydraulic Fracture Initiation and Propagation: An Experimental Study*, in *SPE Hydraulic Fracturing Technology Conference and Exhibition*. 2017, Society of Petroleum Engineers: The Woodlands, Texas, USA. p. 27.

44. Bahorich, B.L., *Examining the effect of cemented natural fractures on hydraulic fracture propagation in hydrostone block experiments*, in *Petroleum and Geosystems Engineering*. 2012, The University of Texas at Austin: UT Electronic Theses and Dissertations.

45. Fu, W., et al., *Impact of Partially Cemented and Non-persistent Natural Fractures on Hydraulic Fracture Propagation.* Rock Mechanics and Rock Engineering, 2016. **49**(11): p. 4519-4526.

46. Moore, L.P. and H. Ramakrishnan, *Restimulation: Candidate Selection Methodologies and Treatment Optimization*, in *SPE Annual Technical Conference and Exhibition*. 2006, Society of Petroleum Engineers: San Antonio, Texas, USA. p. 9.

47. Zhang, G.Q. and M. Chen, *Dynamic fracture propagation in hydraulic re-fracturing.* Journal of Petroleum Science and Engineering, 2010. **70**(3): p. 266-272.

48. Griffith, A.A., *The phenomena of rupture and flow in solids.* Phil Trans Roy Sot Lon (Series A), 1921. **221**: p. 163-198.

49. Irwin, G., *Analysis of stresses and strains near the end of a crack travers- ing a plate.* Journal of Applied Mechanics, 1957. **24**: p. 361–364.

50. Sneddon, I. *The distribution of stress in the neighbourhood of a crack in an elastic solid*. in *Proceedings of the Royal Society of London A: Mathematical, Physical and Engineering Sciences*. 1946. The Royal Society.

51. Sneddon, I. and H. Elliot, *The opening of a Griffith crack under internal pressure.* Quart. Appl. Math, 1946. **4**(3): p. 262-267.

52. Perkins, T.K. and L.R. Kern, *Widths of Hydraulic Fractures.* Journal of Petroleum Technology, 1961. **13**(09): p. 937-949.

53. Khristianovic, S. and Y. Zheltov. *Formation of vertical fractures by means of highly viscous fluids*. in *Proc. 4th world petroleum congress, Rome*. 1955.

54. Detournay, E., *Propagation Regimes of Fluid-Driven Fractures in Impermeable Rocks.* International Journal of Geomechanics, 2004. **4**(1): p. 35-45.

55. Detournay, E. and A. Peirce, *On the moving boundary conditions for a hydraulic fracture.* International Journal of Engineering Science, 2014. **84**: p. 147-155.

56. Desroches, J., et al., *The crack tip region in hydraulic fracturing.* Proceedings of the Royal Society of London. Series A: Mathematical and Physical Sciences, 1994. **447**(1929): p. 39-48.

57. Adachi, J., et al., *Computer simulation of hydraulic fractures.* International Journal of Rock Mechanics and Mining Sciences, 2007. **44**(5): p. 739-757.

58. Blanton, T.L., *An Experimental Study of Interaction Between Hydraulically Induced and Pre-Existing Fractures*, in *SPE Unconventional Gas Recovery Symposium*. 1982, Society of Petroleum Engineers: Pittsburgh, Pennsylvania. p. 13.

59. Gale, J.F.W., S.J. Elliott, and S.E. Laubach, *Hydraulic Fractures in Core From Stimulated Reservoirs: Core Fracture Description of HFTS Slant Core, Midland Basin, West Texas*, in *Unconventional Resources Technology Conference, Houston, Texas, 23-25 July 2018*. p. 1340-1357.

60. Gale, J.F.W., R.M. Reed, and J. Holder, *Natural fractures in the Barnett Shale and their importance for hydraulic fracture treatments.* AAPG Bulletin, 2007. **91**(4): p. 603-622.

61. Wilson, Z.A. and C.M. Landis, *Phase-field modeling of hydraulic fracture.* Journal of the Mechanics and Physics of Solids, 2016. **96**: p. 264-290.

62. Rungamornrat, J., M.F. Wheeler, and M.E. Mear, *Coupling of Fracture/Non-Newtonian Flow for Simulating Nonplanar Evolution of Hydraulic Fractures*, in *SPE Annual Technical Conference and Exhibition*. 2005, Society of Petroleum Engineers: Dallas, Texas. p. 9.

63. Dahi-Taleghani, A. and J.E. Olson, *Numerical Modeling of Multistranded-Hydraulic-Fracture Propagation: Accounting for the Interaction Between Induced and Natural Fractures.* SPE Journal, 2011. **16**(03): p. 575-581.

64. Bryant, E.C., J. Hwang, and M.M. Sharma. *Arbitrary Fracture Propagation in Heterogeneous Poroelastic Formations Using a Finite Volume-Based Cohesive Zone Model*. in *SPE Hydraulic Fracturing Technology Conference*. 2015. Society of Petroleum Engineers.

65. Shakoor, M., et al., *Computational Methods for Ductile Fracture Modeling at the Microscale.* Archives of Computational Methods in Engineering, 2018.

66. Ha, Y.D. and F. Bobaru, *Studies of dynamic crack propagation and crack branching with peridynamics.* International Journal of Fracture, 2010. **162**(1): p. 229-244.

67. Ouchi, H., et al., *A fully coupled porous flow and geomechanics model for fluid driven cracks: a peridynamics approach.* Computational Mechanics, 2015. **55**(3): p. 561-576.

68. Borden, M.J., *Isogeometric analysis of phase-field models for dynamic brittle and ductile fracture*, in *Computational Science, Engineering, and Mathematics*. 2012, University of Texas at Austin: UT Electronic Theses and Dissertations.

69. Borden, M.J., et al., *A higher-order phase-field model for brittle fracture: Formulation and analysis within the isogeometric analysis framework.* Computer Methods in Applied Mechanics and Engineering, 2014. **273**: p. 100-118.

70. Borden, M.J., et al., *A phase-field description of dynamic brittle fracture.* Computer Methods in Applied Mechanics and Engineering, 2012. **217-220**: p. 77-95.

71. Bourdin, B., C.P. Chukwudozie, and K. Yoshioka, *A Variational Approach to the Numerical Simulation of Hydraulic Fracturing*, in *SPE Annual Technical Conference and Exhibition*. 2012, Society of Petroleum Engineers: San Antonio, Texas, USA. p. 9.

72. Bourdin, B., C.J. Larsen, and C.L. Richardson, *A time-discrete model for dynamic fracture based on crack regularization.* International Journal of Fracture, 2011. **168**(2): p. 133-143.

73. Chen, L.-Q., *Phase-Field Models for Microstructure Evolution.* Annual Review of Materials Research, 2002. **32**(1): p. 113-140.

74. Fried, E. and M.E. Gurtin, *Continuum theory of thermally induced phase transitions based on an order parameter.* Physica D: Nonlinear Phenomena, 1993. **68**(3): p. 326-343.

75. Furrer, D.U., *Application of phase-field modeling to industrial materials and manufacturing processes.* Current Opinion in Solid State and Materials Science, 2011. **15**(3): p. 134-140.

76. Heister, T., M.F. Wheeler, and T. Wick, *A primal-dual active set method and predictor-corrector mesh adaptivity for computing fracture propagation using a*

phase-field approach. Computer Methods in Applied Mechanics and Engineering, 2015. **290**: p. 466-495.

77. Henry, H. and H. Levine, *Dynamic Instabilities of Fracture under Biaxial Strain Using a Phase Field Model.* Physical Review Letters, 2004. **93**(10): p. 105504.

78. Hofacker, M. and C. Miehe, *A phase field model of dynamic fracture: Robust field updates for the analysis of complex crack patterns.* International Journal for Numerical Methods in Engineering, 2013. **93**(3): p. 276-301.

79. Karma, A., D.A. Kessler, and H. Levine, *Phase-Field Model of Mode III Dynamic Fracture.* Physical Review Letters, 2001. **87**(4): p. 045501.

80. Khoei, A.R., et al., *A mesh-independent finite element formulation for modeling crack growth in saturated porous media based on an enriched-FEM technique.* International Journal of Fracture, 2014. **188**(1): p. 79-108.

81. Koslowski, M., A.M. Cuitiño, and M. Ortiz, *A phase-field theory of dislocation dynamics, strain hardening and hysteresis in ductile single crystals.* Journal of the Mechanics and Physics of Solids, 2002. **50**(12): p. 2597-2635.

82. Miehe, C. and S. Mauthe, *Phase field modeling of fracture in multi-physics problems. Part III. Crack driving forces in hydro-poro-elasticity and hydraulic fracturing of fluid-saturated porous media.* Computer Methods in Applied Mechanics and Engineering, 2015.

83. Miehe, C., S. Mauthe, and S. Teichtmeister, *Minimization principles for the coupled problem of Darcy–Biot-type fluid transport in porous media linked to*

phase field modeling of fracture. Journal of the Mechanics and Physics of Solids, 2015. **82**: p. 186-217.

84. Miehe, C., F. Welschinger, and M. Hofacker, *Thermodynamically consistent phase-field models of fracture: Variational principles and multi-field FE implementations.* International Journal for Numerical Methods in Engineering, 2010. **83**(10): p. 1273-1311.

85. Mikelic, A., M.F. Wheeler, and T. Wick, *A phase field approach to the fluid filled fracture surrounded by a poroelastic medium.* ICES report, 2013: p. 13-15.

86. Mikelic, A., M.F. Wheeler, and T. Wick, *A quasi-static phase-field approach to the fluid filled fracture.* ICES report, 2013: p. 13-22.

87. Mikelic, A., M.F. Wheeler, and T. Wick, *Phase-field modeling of pressurized fractures in a poroelastic medium.* ICES report, 2014: p. 14-18.

88. Mikelic, A., M.F. Wheeler, and T. Wick, *A phase-field method for propagating fluid-filled fractures coupled to a surrounding porous medium.* Multiscale Modeling & Simulation, 2015. **13**(1): p. 367-398.

89. Mikelić, A., M.F. Wheeler, and T. Wick, *A quasi-static phase-field approach to pressurized fractures.* Nonlinearity, 2015. **28**(5): p. 1371-1399.

90. Mikelić, A., M.F. Wheeler, and T. Wick, *Phase-field modeling of a fluid-driven fracture in a poroelastic medium.* Computational Geosciences, 2015. **19**(6): p. 1171-1195.

91. Verhoosel, C.V. and R. de Borst, *A phase-field model for cohesive fracture.* International Journal for Numerical Methods in Engineering, 2013. **96**(1): p. 43-62.

92. Fasano, A.a.M.P., *Free boundary problems: theory and applications.* Pitman Advanced Pub, 1983. **2**: p. 644–657.

93. Langer, J.S., *MODELS OF PATTERN FORMATION IN FIRST-ORDER PHASE TRANSITIONS*, in *Directions in Condensed Matter Physics*. p. 165-186.

94. Militzer, M., *Phase field modeling of microstructure evolution in steels.* Current Opinion in Solid State and Materials Science, 2011. **15**(3): p. 106-115.

95. Wang, Y. and J. Li, *Phase field modeling of defects and deformation.* Acta Materialia, 2010. **58**(4): p. 1212-1235.

96. Steinbach, I., et al., *A phase field concept for multiphase systems.* Physica D: Nonlinear Phenomena, 1996. **94**(3): p. 135-147.

97. Steinbach, I., *Phase-field models in materials science.* Modelling and Simulation in Materials Science and Engineering, 2009. **17**(7): p. 073001.

98. Bourdin, B., G.A. Francfort, and J.-J. Marigo, *The Variational Approach to Fracture.* Journal of Elasticity, 2008. **91**(1): p. 5-148.

99. Ambrosio, L. and V.M. Tortorelli, *Approximation of functional depending on jumps by elliptic functional via t-convergence.* Communications on Pure and Applied Mathematics, 1990. **43**(8): p. 999-1036.

100. Mikelić, A., M.F. Wheeler, and T. Wick, *A Phase-Field Method for Propagating Fluid-Filled Fractures Coupled to a Surrounding Porous Medium.* Multiscale Modeling & Simulation, 2015. **13**(1): p. 367-398.

101. Miehe, C., S. Mauthe, and S. Teichtmeister, *Minimization principles for the coupled problem of darcy-biot-type fluid transport in porous media linked to phase field modeling of fracture.* Journal of the Mechanics and Physics of Solids, 2015.

102. Francfort, G.A. and J.J. Marigo, *Revisiting brittle fracture as an energy minimization problem.* Journal of the Mechanics and Physics of Solids, 1998. **46**(8): p. 1319-1342.

103. Gurtin, M.E., *Generalized Ginzburg-Landau and Cahn-Hilliard equations based on a microforce balance.* Physica D: Nonlinear Phenomena, 1996. **92**(3): p. 178-192.

104. Coleman, B.D. and W. Noll, *The Thermodynamics of Elastic Materials with Heat Conduction and Viscosity*, in *The Foundations of Mechanics and Thermodynamics: Selected Papers*. 1974, Springer Berlin Heidelberg: Berlin, Heidelberg. p. 145-156.

105. Coussy, O., *Poromechanics*. 2004, Chichester: John Wiley & Sons.

106. Biot, M.A., *Theory of Propagation of Elastic Waves in a Fluid-Saturated Porous Solid. II. Higher Frequency Range.* The Journal of the Acoustical Society of America, 1956. **28**(2): p. 179-191.

107. Coussy, O., L. Dormieux, and E.M. Detournay, *From mixture theory to biot's approach for porous media.* International Journal of Solids and Structures, 1998. **35**: p. 16.

108. Detournay, E. and A.H.D. Cheng, *Fundamentals of Poroelasticity*, in *Analysis and Design Methods*, C. Fairhurst, Editor. 1993, Pergamon: Oxford. p. 113-171.

109. Taylor, C. and P. Hood, *A numerical solution of the Navier-Stokes equations using the finite element technique.* Computers & Fluids, 1973. **1**(1): p. 73-100.

110. Babuška, I., *The finite element method with Lagrangian multipliers.* Numerische Mathematik, 1973. **20**(3): p. 179-192.

111. Brezzi, F., *On the existence, uniqueness and approximation of saddle-point problems arising from lagrangian multipliers.* Mathematical Modelling and Numerical Analysis, 1974. **8**(2): p. 22.

112. Gropp and Dmitry Karpeyev and Dinesh Kaushik and Matthew G. Knepley and Dave A. May and Lois Curfman McInnes and Richard Tran Mills and Todd Munson and Karl Rupp and Patrick Sanan and Barry~F. Smith and Stefano Zampini and Hong Zhang and Hong Zhang, S.B.a.S.A.a.M.F.A.a.J.B.a.P.B.a.K.B.a.L.D.a.A.D.a.V.E.a.W.D. *PETSc Web page*. 2019; Available from: http://www.mcs.anl.gov/petsc.

113. Zanganeh, B., et al., *The role of hydraulic fracture geometry and conductivity profile, unpropped zone conductivity and fracturing fluid flowback on production performance of shale oil wells.* Journal of Unconventional Oil and Gas Resources, 2015. **9**: p. 103-113.